Consultation on IESC Information Guidelines Explanatory Note: Subsidence Associated with Coal Seam Gas Mining

The Independent Expert Scientific Committee on Coal Seam Gas and Large Coal Mining Development (IESC) is seeking comment on the draft IESC Information Guidelines Explanatory Note: Subsidence Associated with Coal Seam Gas Mining.

The IESC notes the draft nature of the Explanatory Note and welcomes feedback on the content, usability and applicability. In particular, views are sought on:

- **the technical content within the draft Explanatory Note. Are there any areas that are missing or not captured adequately?**
- **the relevance to your specific area of work; and**
- **potential options to increase uptake and adoption.**

The IESC and the Information Guidelines

The IESC is a statutory body under the Environment Protection and Biodiversity Conservation Act 1999 (Cth). One of the IESC's key legislative functions is to provide independent scientific advice to the Australian Government Environment Minister and relevant state ministers in relation to coal seam gas (CSG) and large coal mining (LCM) development proposals that are likely to have a significant impact on water resources.

The IESC Information Guidelines outline the information project proponents should provide to enable the IESC to provide robust scientific advice on the potential water-related impacts of CSG and LCM developments proposals. For some topics, Explanatory Notes have been written to supplement the IESC Information Guidelines, providing tailored guidance and up-to-date robust scientific methodologies and tools for specific components of Environmental Assessments on coal seam gas and large coal mining developments. Case studies and practical examples of how to collect and present relevant information are also included.

Information Guidelines Explanatory Note: Subsidence Associated with Underground Coal Mining

The *Information Guidelines Explanatory Note: Subsidence Associated with Coal Seam Gas Production* provides tailored guidance and up-to-date robust scientific methodologies and tools for assessing the risk and magnitudes of subsidence (one source of surface movement) and its environmental impact due to CSG development. It is targeted at prospective consultants and assessors dealing with CSG project proposals.

The EPBC Act lists "a water resource, in relation to coal seam gas development and large coal mining development" as a matter of national environmental significance. A water resource is defined under the Water Act 2007 (Cth). It covers surface water or groundwater or a watercourse, lake, wetland or aquifer (whether or not it currently has water in it) and includes all aspects of the water resource (including water, organisms and other components and ecosystems that contribute to the physical state and environmental value of the water resource.

Independent Expert Scientific Committee
on Coal Seam Gas and Large Coal Mining Development

Information Guidelines Explanatory Note

Subsidence associated with coal seam gas production

This report should be attributed as 'Subsidence associated with coal seam gas production: Explanatory Note, Commonwealth of Australia, 2023'.

This publication is funded by the Australian Government Department of Climate Change, Energy, the Environment and Water. The views and opinions expressed in this publication are those of the authors and do not necessarily reflect those of the Australian Government, the Minister for Climate Change and Energy, or the Minister for the Environment and Water.

Acknowledgements

This report was finalised by the Independent Expert Scientific Committee on Coal Seam Gas and Large Coal Mining Development (IESC) based on consideration of work commissioned by the Office of Water Science on behalf of the IESC in January 2022 through the Department of Climate Change, Energy, the Environment and Water .

The main contributor to this work was Christopher Leonardi (The University of Queensland). The contributions of the following (in alphabetical order) are gratefully acknowledged: Sarah Brennand, Katarina David, Phil Hayes (IESC), Sebastian Hörning, Mohsen Masoudian, Travis Mitchell, Iain Rodger, Vanessa Salomao de Santiago, Wendy Timms (IESC), Jim Underschultz, Mohammadreza Zare Reisabadi, and Fengde Zhou.

Contact details

For information about this report or about the work of the IESC, please contact:

IESC Secretariat
Office of Water Science
Department of Climate Change, Energy, the Environment and Water
GPO Box 787
CANBERRA ACT 2601

The report can be accessed at http://www.iesc.gov.au/

Images

Front Cover: McIntyre River | Location: Condamine catchment area | © Department of the Environment and Energy
© Department of the Environment and Energy (taken by staff)

All other images © Department of Climate Change, Energy, the Environment and Water unless specified otherwise.

Information Guidelines
Explanatory Note

Subsidence associated with coal seam gas production

1. Executive Summary

Coal seam gas (CSG) production is currently taking place in Queensland and New South Wales, Australia, and it is possible that CSG production will occur in Australia for the next half a century. For both current and future production, the potential impacts of subsidence on adjacent industries, particularly agriculture, must be managed. This Explanatory Note outlines the analysis and monitoring tools that can be used to manage ongoing CSG activities and assess new projects in the context of subsidence.

Since publication of the last IESC Explanatory Note on CSG-induced subsidence in 2014, a number of independent sources have confirmed that CSG production does induce subsidence, but the magnitudes of surface elevation and slope change are relatively low. Satellite-borne InSAR measurements indicate that most CSG-producing areas within the Surat and Bowen Basins, and the smaller Camden Gas Project in NSW, have subsided less than 100 mm. This is more than one order of magnitude less than that associated with underground longwall coal mining operations. In some areas the CSG-induced subsidence is of a similar order of magnitude as natural fluctuations, such as the shrinking and swelling of expansive clays, and so any impact of CSG operations needs to be considered in this context. Given that the magnitude of CSG-induced subsidence and differential settlement are both small and similar to natural fluctuations, the risk of impacts on infrastructure is low. Greatest attention must be given to locations that are sensitive to small changes in slope, such as flood-irrigated paddocks. However, there currently exists no evidence that CSG-induced subsidence has, or has the potential to, significantly alter surface drainage behaviour.

CSG-induced subsidence is driven by poromechanical compaction of coal and non-coal (i.e. rock) sedimentary layers in the subsurface, as well as desorption-induced shrinkage of the coal. Both mechanisms should be accounted for in future forecasts, noting that the degree to which shrinkage occurs *in situ* is an area of ongoing research. The quality of subsidence predictions is, consequently, dependent on the quality of predictions of water-gas transport and subsurface depressurisation. This is complicated by the stratigraphic complexity of, for example, the Walloon Coal Measures in the Surat Basin, where dozens of thin and laterally-discontinuous coal seams are interleaved with layers of clastic rocks that can be significantly less permeable than the coal. Well-justified assumptions must be used to simplify such complex stratigraphy in analysis. Analytical and numerical approaches both have their place in the prediction of CSG-induced subsidence. The former can capture much broader length and time scales, while the latter can better accommodate stratigraphic heterogeneity and geological features, such as faults, and include more detailed material properties, leaving them well suited to hypothesis testing and benchmarking of analytical solutions.

InSAR has been demonstrated to be effective at monitoring basin-scale surface movement, of which CSG-induced subsidence is one part of the total signal. InSAR is not (yet) effective in areas prone to decorrelation (e.g. over areas of intensive cropping), where it is currently needed most. The deployment of LiDAR or other levelling methods is recommended to complement InSAR in these areas, as they (LiDAR in particular) are well-suited to capturing relative, as opposed to absolute, movement, which can be used to accurately determine changes in surface gradient.

The integrated use of monitoring and modelling for subsidence analysis and forecasting continues to advance around the world. The opportunity therefore exists to adopt some of these techniques for application related to CSG production. These include stochastic analysis, uncertainty quantification, inverse modelling, history matching, and geospatial data analysis. Finally, it should be recognised that there is uncertainty surrounding many of the drivers (e.g. stratigraphy, transport properties, mechanical properties) of CSG-induced subsidence. Some of this uncertainty is irreducible. In the past, uncertainty has been addressed by making conservative assumptions during the process of predicting potential future subsidence. This is not in the best interest of most, if not all stakeholders, and so it is important that continued research and development (see Section 10) is leveraged to narrow the various windows of uncertainty.

Table of Contents

2. Introduction

The production of coal seam gas (CSG) requires the extraction of associated water from the target formation to liberate methane that is adsorbed to the coal. Depressurisation of the subsurface leads to the compaction of geological units, a proportion of which can propagate to the surface, resulting in subsidence. An understanding of the magnitude and any risks of impacts associated with subsidence is of value to stakeholders including landholders, operators, local communities, and government regulators.

The Office of Water Science provides assistance to the Independent Expert Scientific Committee on Coal Seam Gas and Large Coal Mine Developments (IESC) in developing their IESC Information Guidelines. The guidelines outline to proponents and consultants the information requirements considered necessary to enable the IESC to provide robust scientific advice to government regulators on the water-related impacts of CSG and large coal mining development proposals. The IESC committed to the production of Explanatory Notes (EN), which give more detailed background information on selected aspects of the guidelines. This EN addresses subsidence related to CSG production, while a companion document (Hebblewhite, 2022) addresses underground coal mining.

The aim of this EN is to present tailored guidance and robust scientific methodologies and tools for assessing the potential for and subsequent monitoring of subsidence associated with CSG production. It has been prepared for a target audience of technical professionals commissioned with the preparation of environmental impact statements. Topics covered include:

- The production of CSG and the physical processes associated with compaction and subsidence;
- National and international perspectives on subsidence, including the potential impacts of subsidence;
- The prediction of subsidence, including parameter and model selection and the interpretation of results;
- Techniques for large-scale monitoring of subsidence in near-real-time;
- Australian experience in the estimation and monitoring of subsidence related to CSG production.

The production of CSG in Australia accelerated with the commencement of liquified natural gas (LNG) export in 2014. There are no other comparable projects internationally that extract CSG at the same scale. In comparison to conventional oil and gas production, the Australian CSG industry is young and thus the scientific literature and technical documentation focused on CSG-induced subsidence is limited. However, the volume of monitoring data (acquired from satellite and aircraft) continues to grow in terms of frequency and spatial extent. In addition to these data, this EN has been prepared using information available in the public domain, including journal articles, conference proceedings, scientific textbooks, government department reports, and industry and consulting reports.

The structure of this EN is summarised as follows. Section 3 provides background information on the production of CSG, including how a well is constructed, the physical processes relevant to CSG production, and the driving mechanisms of CSG-induced subsidence. Section 4 briefly discusses international and domestic examples of anthropogenic subsidence, with a focus on oil and gas production. Section 5 then presents information on sources and impacts of subsidence with a focus on those most relevant to areas of CSG production in Australia. Subsidence monitoring techniques such as interferometric synthetic aperture radar (InSAR) are presented in Section 6, along with examples of their use. Section 7 outlines approaches to subsidence assessment, including simple consolidation modelling and poromechanical analysis, while Section 8 provides guidance on selection of relevant modelling parameters. Past analyses and a subsidence case study are presented in Section 9 and then Section 10 concludes with a discussion of ongoing monitoring and assessment activity and future research requirements.

3. Mechanics of Coal Seam Gas Production

Coal seam gas (CSG), more commonly referred to as coalbed methane (CBM) outside of Australia, is natural gas extracted from coal seams. It is comprised primarily of methane (CH_4) and can be utilised for electricity generation, industrial and residential heating, and as feedstock in manufacturing (e.g. fertiliser). It is the same as other *conventional* sources of gas and can be distributed similarly, either in gaseous form or after cooling to liquified natural gas (LNG).

Commercial production of CSG commenced in Australia in the 1990s. To the end of 2019, approximately eight trillion cubic feet (tcf) of CSG had been extracted, with a further 30 tcf of *reserves* and 24 tcf of *resources* (Geoscience Australia, 2021) in place throughout Queensland and New South Wales. In 2014, the export of CSG as liquified natural gas (LNG) commenced at Curtis Island in Queensland, resulting in a rapid increase in the number of wells drilled and the annual rate of production. In combination with gas produced from conventional reservoirs, the CSG-LNG industry has positioned Australia as the largest LNG exporter in the world.

3.1 What is coal seam gas?

The exploitation of *conventional* oil and gas reserves typically involves the extraction of liquid and or gaseous hydrocarbons from porous, permeable formations remote from the original source rock. The classical example of this is an anticlinal trap, in which a sandstone reservoir holds hydrocarbons that have migrated from deeper source rocks due to buoyancy and been trapped by an impermeable caprock above. The production of CSG is classified as *unconventional* because the target hydrocarbons exist within and are extracted directly from the source coal seams. Additionally, the target formations may exhibit low permeability, requiring artificial stimulation (e.g. hydraulic fracturing) to promote economic rates of production. The (usually) lower permeability of unconventional reservoirs may also manifest in greater well densities and associated surface infrastructure than in conventional operations.

The methane in coal is generated via biogenic or thermogenic processes, or a combination of these two. Biogenic methane is a result of the breakdown of organic coal matter by methanogenic microorganisms at moderate to low temperature (i.e. less than 56°C) and, therefore, depth. Conversely, thermogenic methane is generated at greater depths, where temperatures exceed 100°C, due to chemical degradation and thermal cracking of coal (Moore, 2012). The elevated temperature at greater depth also means that methanogenic activity of microbes is improbable at those locations. Consequently, biogenic methane is more likely to be found in lower-rank coals while thermogenic methane is more likely in mid- to high-rank coals subject to greater burial depth and temperature, as shown schematically in Figure 1(a). Assuming the methane does not escape, this also means that methane content increases for a given depth and coal grade (Aminian, 2020), as seen in Figure 1(b). Noting that other hydrocarbons will exist, the proportion of methane in CSG relative to those gases is referred to as *gas quality*.

CSG manifests in three different states, namely free gas within coal pores and cleats, molecules adsorbed to coal surfaces, or adsorbed within the molecular structure of the coal (Moore, 2012). The majority (between 90 and 98 % of all gas), however, is adsorbed to the coal surface within macro-, meso-, and micropores, representing the greatest proportion of gas that is extracted during CSG production. Due to the hydrostatic pressure of pore water (or *brine*), this adsorbed gas exists in a state of compression. The relationship between gas storage capacity and pressure is described by a sorption isotherm, represented by the data series in Figure 1(b) for coals of different maturity. In addition to the rank and pressure, these isotherms also depend on the temperature, moisture content, and mineral matter content of the coal.

Coal seams are typically interbedded between low permeability geological units (e.g. siltstone) and are of varying thickness relative to overlying and underlying strata. Seams may exhibit thicknesses of multiple metres with good

lateral continuity or, conversely, with thickness on the order of centimetres which pinch out (i.e. terminate) or bifurcate laterally, as shown schematically in Figure 2. In a macroscopic sense, coal seams usually possess *cleats*, which are discontinuities formed during coalification (i.e. dessication), and may also possess natural fractures, which are formed by tectonic deformation. The cleats usually occur in two sets, called *face cleats* and *butt cleats*, that are perpendicular to one another and perpendicular to bedding. The face cleats form in one direction first and exhibit a high level of continuity. The butt cleats form in the other direction, are discontinuous, and frequently truncated by face cleats. The permeability of a coal seam is dominated by the cleat network (Laubach et al., 1998) and, in the Australian context, the natural fractures. The greater continuity of face cleats typically results in greater permeability than in butt cleats. However, both provide enhanced permeability with respect to that of the intact coal matrix.

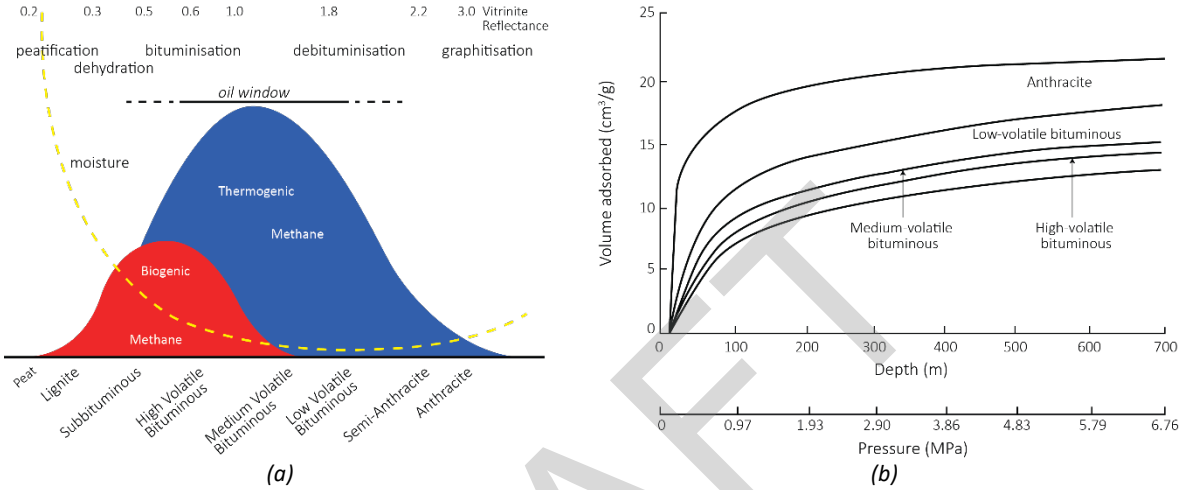

Figure 1: The relationship between coal rank/depth and gas type/content, showing (a) biogenic and thermogenic methane generation as a function of rank (reproduced from Moore (2012)) and, (b) gas content as a function of depth (reproduced from Aminian (2020)).

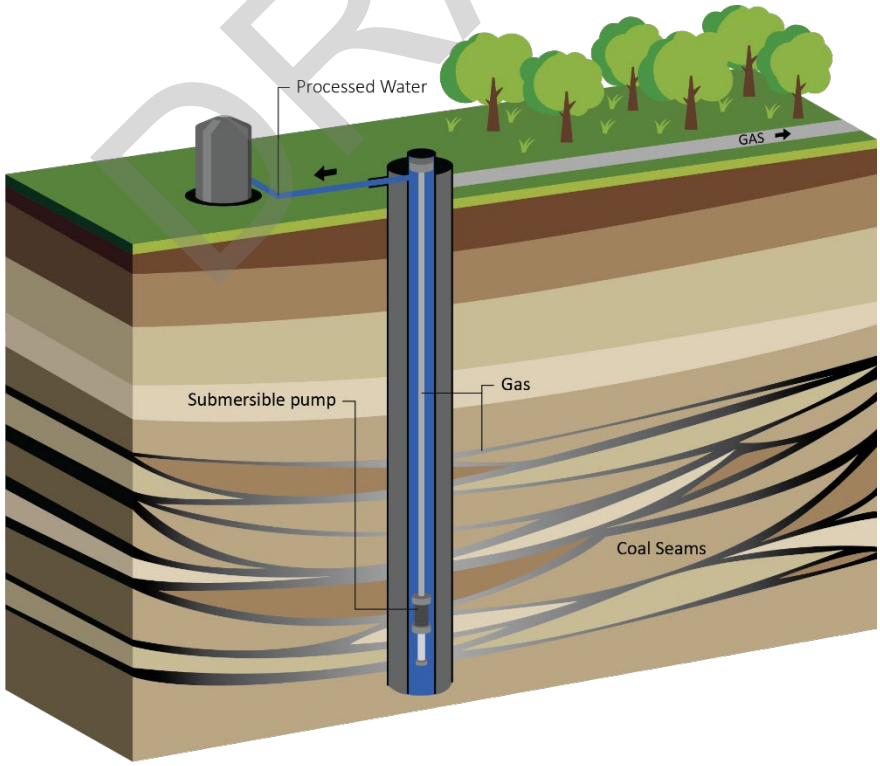

Figure 2: Schematic representation of CSG production, highlighting the existence of a number of adjacent seams that are initially saturated with brine, as well as being potentially discontinuous and interleaved with other sedimentary layers.

CSG production is typically undertaken in mid-rank coals (i.e. low- to high-volatile bituminous coals). This is because the desorption and diffusive transport of methane from high rank coals such as *anthracite* is very slow (Levine 1993; Rice 1993) and the residual gas content is low. The liberation of adsorbed methane is driven by the reduction of pore pressure, which in practice is achieved by the reduction of pressure head by pumping associated water from the coal seam. This is central to the issues of compaction and subsidence and is discussed in more detail in Section 3.3.

More detailed discussion of the processes of deposition, coalification, and the genesis of methane, can be found in the comprehensive text edited by Thakur (2020) or the more concise review by Moore (2012).

3.2 Coal seam gas production in Australia

Onshore gas was first discovered and produced in Australia by accident during the drilling of a water bore outside Roma, Queensland, in 1900 (Roberts, 1992). Numerous other instances of nuisance or unexpected gas discovery during the drilling of water wells and mineral exploration holes have been documented (Walker & Mallants, 2014). However, it was not until the 1960s that conventional gas accumulations were commercially exploited.

Dedicated exploration for CSG as a target resource commenced in Australia in the 1970s. In the 1980s, methane was first extracted directly from Australian coal during the drainage of seams prior to underground longwall mining (Black & Aziz, 2009). This was, and still is, necessary to reduce the risk of explosion during mining operations. Historically, the produced gas was typically flared off but is now captured and utilised on site. By 1990, approximately 30 CSG-specific wells had been drilled in the Bowen Basin. Approximately 160 wells had been drilled by 1995, mostly in the Bowen Basin. In 1996, commercial production commenced from the Baralaba Coal Measures at Dawson River, near Moura, to service the domestic market in south-east Queensland (Towler et al., 2016). Commercial CSG production from lower-rank, sub-bituminous Walloon coal seams in the Surat Basin began in 2006 via the Tipton West, Kogan and Berwyndale fields located in the areas west of and between Dalby and Chinchilla. In 2007, CSG production exceeded conventional gas production in Queensland, and by 30 June 2008 certified reserves in the Surat Basin had surpassed those in the Bowen Basin. In 2011, the Surat Basin overtook the Bowen Basin as the chief producer of natural gas in general, but of CSG in particular (Geological Survey of Queensland, 2012). The construction of three distinct compression facilities at Curtis Island, near Gladstone, in Queensland facilitated the production of LNG from CSG and connection to global markets. In preparation for the first shipment of LNG in 2014, the rate of CSG well drilling increased in 2012. In 2022 the total CSG well count in Queensland was approximately 10,000, and this is projected to increase to approximately 22,000 by 2035 (OGIA, 2021).

Contemporary CSG production in Australia is still dominated by plays in the Surat and Bowen Basins in Queensland, whose locations are shown in Figure 3. In the Surat Basin, gas is primarily produced from thin, high-permeability coals in the Jurassic-age Walloon Coal Measures, while in the Bowen Basin production is sourced from several relatively thick Permian-age coal seams, of which the Baralaba Coal Measures and the Bandanna formation are the most important (Towler et al., 2016). In New South Wales, exploration and approvals for the Narrabri gas project in the Gunnedah Basin (see Figure 4) are, at the time of writing, ongoing. Other past and proposed developments are located within the Sydney, Galilee, Clarence-Moreton, Gloucester, Otway, Gippsland, and Cooper Basins located across Queensland, New South Wales, Victoria, and South Australia (Best et al., 2014).

The hydrogeological setting in CSG-producing basins typically comprise surficial alluvial aquifer systems (such as in sands or clays), underlain by consolidated sedimentary geological units (such as sandstone, siltstone, mudstone), with coal seams interbedded within the sedimentary units. The coal seams targeted for gas production are usually located at depths of 100 m or greater. Coal *measures* refer to the geological sedimentary unit in which potentially multiple coal seams are interbedded within a sedimentary profile. As previously mentioned, the coal seam thickness can vary widely along with their lateral continuity. For example, the Gloucester Coal Measures within the Gloucester Basin contain a number of relatively thick and continuous seams (as do the Baralaba Coal Measures of the Bowen Basin), while the Walloon Coal Measures of the Surat Basin are comprised of many discontinuous and relatively thin seams

(Best et al., 2014). As indicated across Figure 3 and Figure 4, the Permo-Triassic Age Bowen Basin forms the northern part of the Bowen-Gunnedah-Sydney Basin System of eastern Australia. The stratigraphic sequencing of the Bowen and Surat Basins is shown schematically in Figure 5, highlighting the relative locations of the Moolayember Formation, the Baralaba Coal Measures, the Moranbah Coal Measures, the Burunga Formation, the Bandanna Formation, the Flat Top to Buffel Formations, and the Walloon Coal Measures.

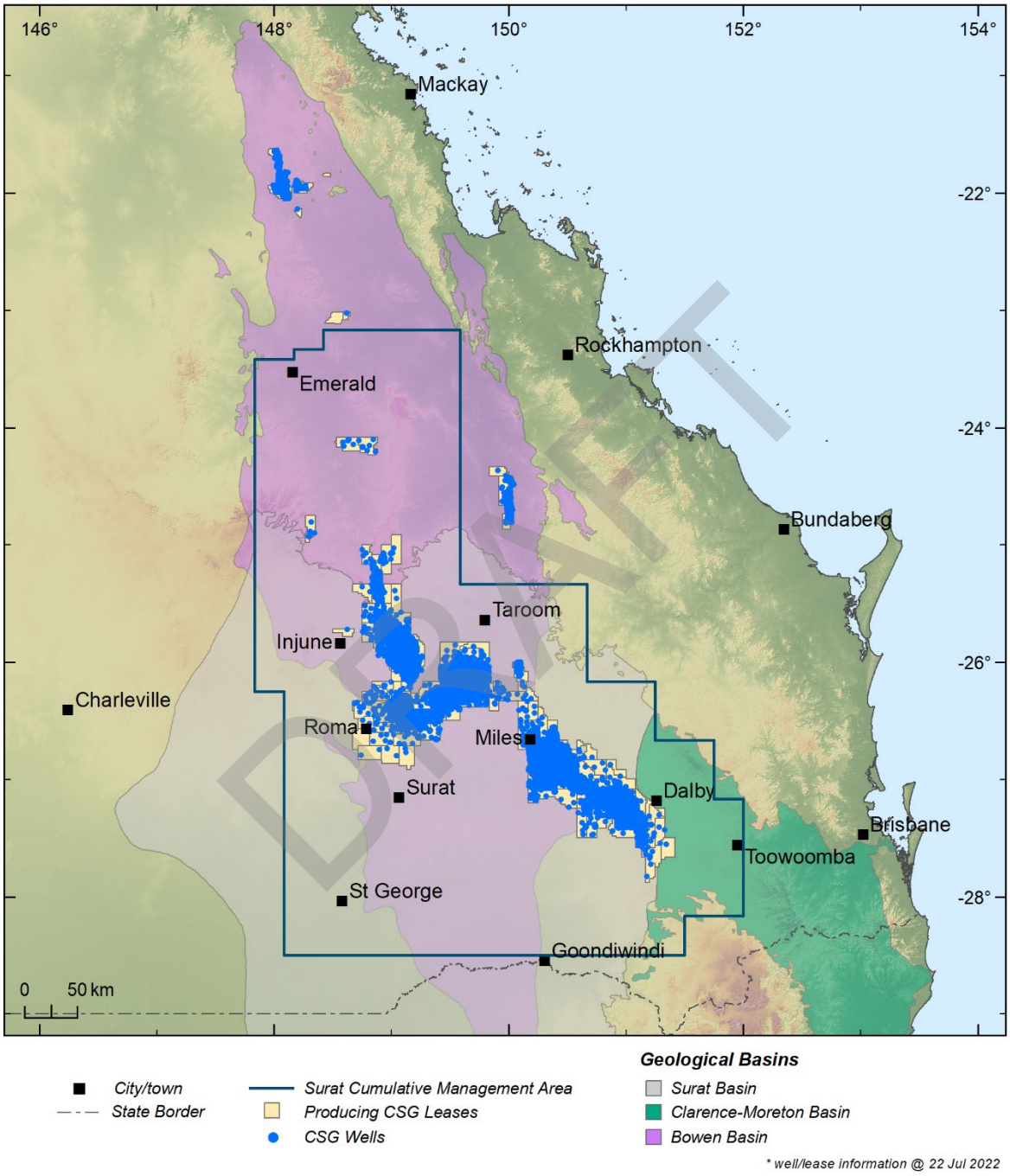

Figure 3: Map of the sedimentary basins, petroleum leases, and wells relevant to the CSG industry in Queensland. The outline of the Surat Cumulative Management Area (CMA) is included for reference.

The geological and petroleum-generating history of the Surat and Bowen Basins is long and complex. These petroliferous basins contain multiple source rock horizons, which includes extensive coal deposits. Thermogenesis has generated both liquid and gaseous hydrocarbons that are stored in conventional and unconventional reservoirs. Extensive biogenic gas generation has also occurred (Al-Arouri et al., 1998; Golding et al., 2013; Hamilton et al.,

2014), which continues today. Of Australia's 30 tcf of remaining proved and probable (i.e. 2P) *reserves* (as at the end of 2019), 24 tcf is located in the Surat Basin with the balance located in the Bowen Basin. Together, the Bowen and Surat Basins hold 19 tcf of contingent *resources* (3C), with an additional 2.3 tcf in the Galilee Basin, 1.8 tcf in the Gunnedah Basin, and 0.6 tcf in the Clarence-Moreton Basin (Geoscience Australia, 2021). Generally speaking, a resource is gas in place that cannot be commercially produced, while a reserve is gas in place that can be commercially produced (refer to the Glossary for more detailed definitions).

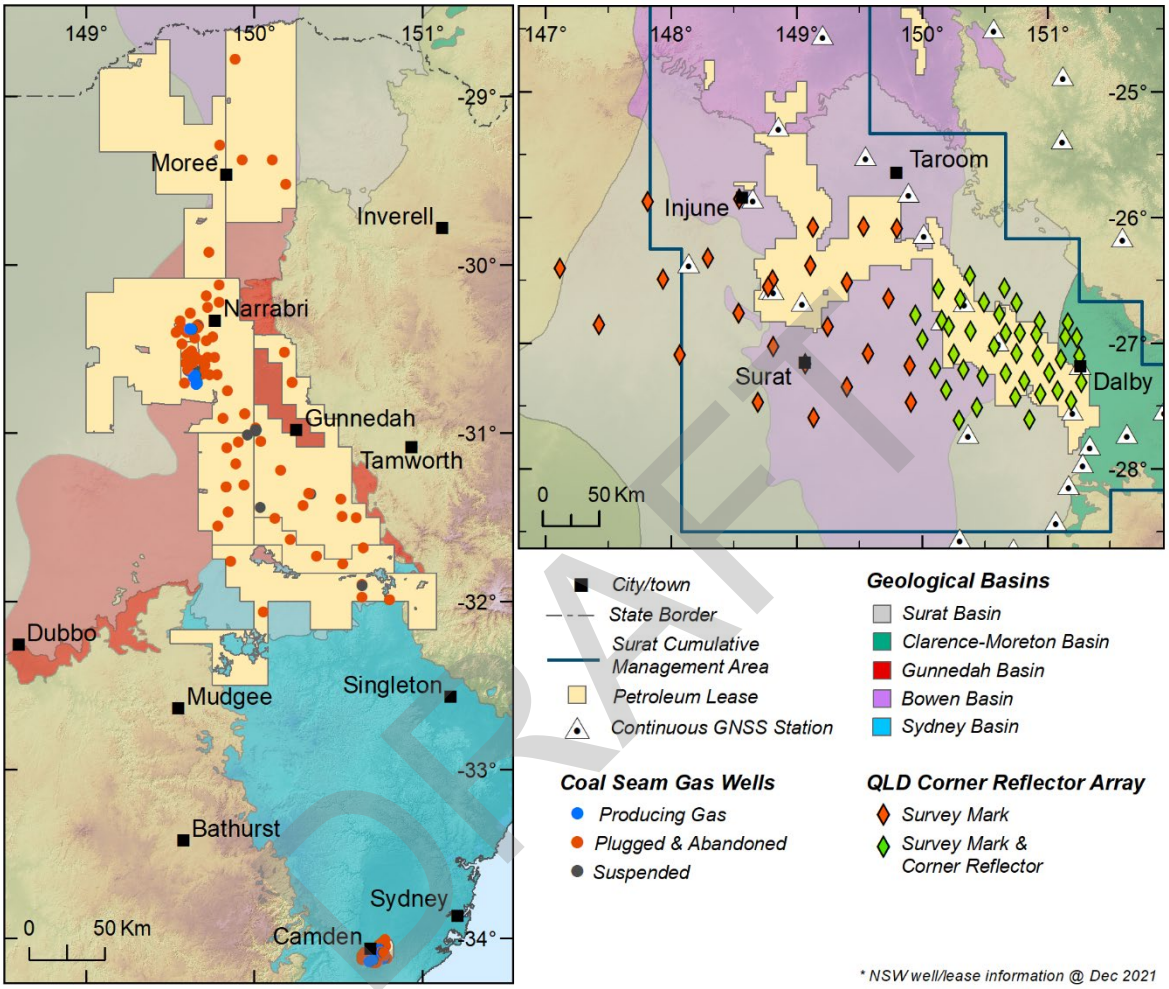

Figure 4: Map of (L) the sedimentary basins, petroleum leases, and wells relevant to the Narrabri gas project in New South Wales and (R) the location of corner reflectors and permanent survey markers in southern Queensland (refer to Section 6.4).

The CSG activity of different operators in Queensland, as delineated by petroleum leases, are often located directly adjacent to one another. Although these activities are located in areas of low population density, they are commonly co-located with or near to other economic activity such as intensive cropping (e.g. flood-irrigated arable farming), low-density grazing of livestock, high-density feedlots, or coal mining. Challenges related to social license to operate can arise when this combines with the large areas over which CSG production occurs, as compared to more conventional oil and gas production. One prominent example of the social license challenge is the effect of coal seam dewatering on agricultural and domestic water wells completed in the coal measures, particularly in water-stressed areas. Another example of social license challenges is the perceived possibility of localised changes in ground surface gradient caused by subsidence. If gradient change exceeds a threshold magnitude, this has the potential to alter the surface run-off characteristics of natural waterways, drainage networks, and irrigated paddocks. The latter is of direct relevance to this document.

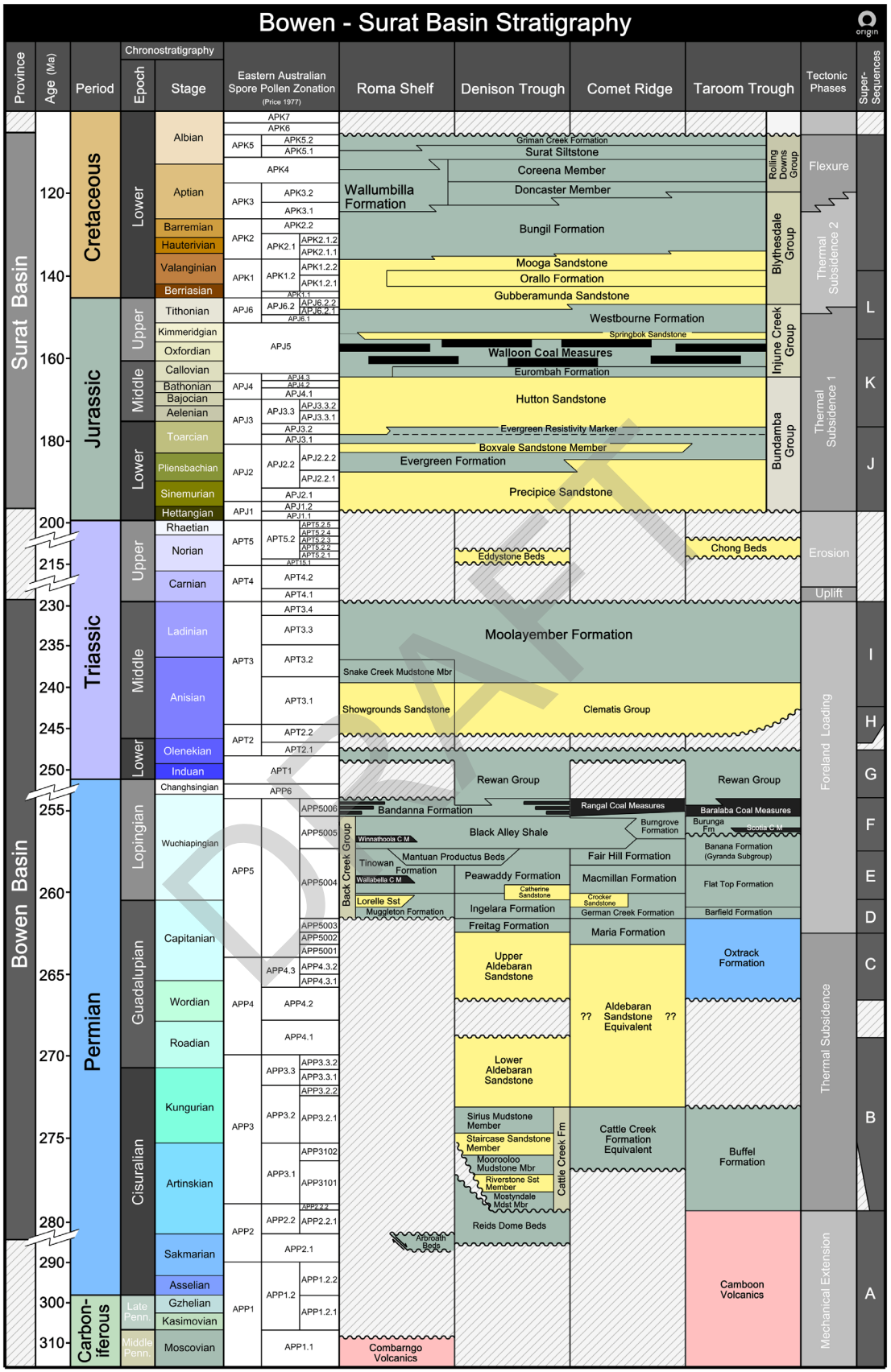

Figure 5: Stratigraphic diagram of the Bowen and Surat Basins (original by Cook (2013), further modified by Santos and Origin Energy). Formations of interest include the Walloon and Baralaba Coal Measures, and the Bandana Formation.

3.3 Physical processes relevant to CSG production

As with conventional oil and gas production, the optimal choice of drilling, completion, stimulation, and production techniques for CSG requires a comprehensive understanding of the subsurface, including geology, stratigraphy, geomechanics, and transport properties of the coal and adjacent rocks. However, the development and operation of a CSG field differs from that of conventional fields in a number of ways. Releasing adsorbed methane from the target coal requires pressure reductions which are induced by dewatering. Limits on the drainage area per well mean comparatively high well densities are required. CSG wells are typically shallower than shale or conventional wells, which reduces the engineering requirements of completion design, but the greater number of wells per unit area means field development must be optimised.

One challenge to CSG production is the degree of inherent heterogeneity of lithology, continuity, connectivity and stresses within and between coal seams, in addition to the variable interconnectivity between the coals and in the over- and underlying aquifers and aquitards (Towler et al., 2016). Improved description of stratigraphy and structural geology in the CSG-producing basins in Queensland is an area of active and ongoing research (de Andrade Vieira Filh et al., 2021; Schultz et al., 2021; Sobczak et al., 2021).

Drilling and completion

Each CSG production tenement is comprised of multiple wells, collectively known as a well *field*. The spacing of wells in a field is dictated by local conditions (e.g. permeability) and constraints. The average well density in Queensland is approximately 1.5 wells/km^2 (linear spacing of 800 m based on a square pattern). However, this varies in the Surat Basin from 1.2 to 1.7 wells/km^2 (900 to 750 m linear spacing), and in the Bowen Basin from 0.8 to 1.5 wells/km^2 (1,100 to 800 m linear spacing) (OGIA, 2021). Deviations from these averages and their regular layout are common, however, after well locations have been negotiated with landholders.

A number of different CSG well trajectories have been installed or proposed in Queensland, including vertical, horizontal, multilateral, deviated, surface-to-inseam (SIS), and high-angle-sump-horizontal (HASH) (Lin et al., 2018). Verticals, which produce from a large number of distinct seams (see Figure 6(a)), make up approximately 90% of wells drilled to date in the Bowen and Surat Basins (OGIA, 2021). Recently, Arrow Energy has installed deviated wells in the Surat Basin as a means to reduce surface footprint whilst maintaining necessary contact with the reservoir (Rajora et al., 2019). A single *pad* can accommodate eight or more wells, which can in turn increase well head spacing to up to 2,400 m, reduce gathering network and land access requirements, and provide increased flexibility on pad location (e.g. paddock corners or boundaries). A wider number of well types is employed in the Bowen Basin, depending on coal permeability and depth. This includes vertical, horizontal, SIS, hydraulically fractured wells, and cavitation completions. According to Towler et al. (2016), the most common historical completion type in the higher-permeability fields of the Bowen Basin (e.g. Spring Gully, Fairview) was cavitation.

In addition to constraints related to land access, the trajectory of non-vertical wells is often a compromise between productivity and well stability. Drilling orthogonal to the dominant cleat or fracture set maximises effective permeability but can degrade wellbore stability, which is a function of effective stress magnitude and orientation, and the geomechanical properties of the reservoir. This is exacerbated when drilling in depleted reservoirs as part of, for example, an infill drilling campaign (Zare Reisabadi et al., 2020; Zhong et al., 2022).

A range of well completion strategies, which are designed to connect the coal seam(s) to the well but isolate them from the rest of the subsurface, have been deployed in Queensland. As shown in Figure 6(a), a fully cemented casing is installed from the surface to the shallowest coal target to prevent migration of gas or brine to shallower aquifers or the surface. The integrity of the annular cement seal is pressure-tested after installation and can be inspected throughout the life of a well using, for example, a cement bond log (Jung & Frigaard, 2022). Where a cavitation completion is employed, the target formations are drilled and then reamed to create a large cavity (i.e. increased surface area via a diameter of up to 3 m) and remove any formation damage that occurred during drilling. The well is

either left open, or completed with an uncemented, slotted liner (Mastalerz & Drobniak, 2020). It is also possible to case and cement the well throughout the reservoir and use perforations to make contact with the target coal seams. Similarly, wells that require hydraulic fracturing are cemented along their length and then perforated in stages, each of which serves as the initiation point for a hydraulic fracture in the target coal reservoir.

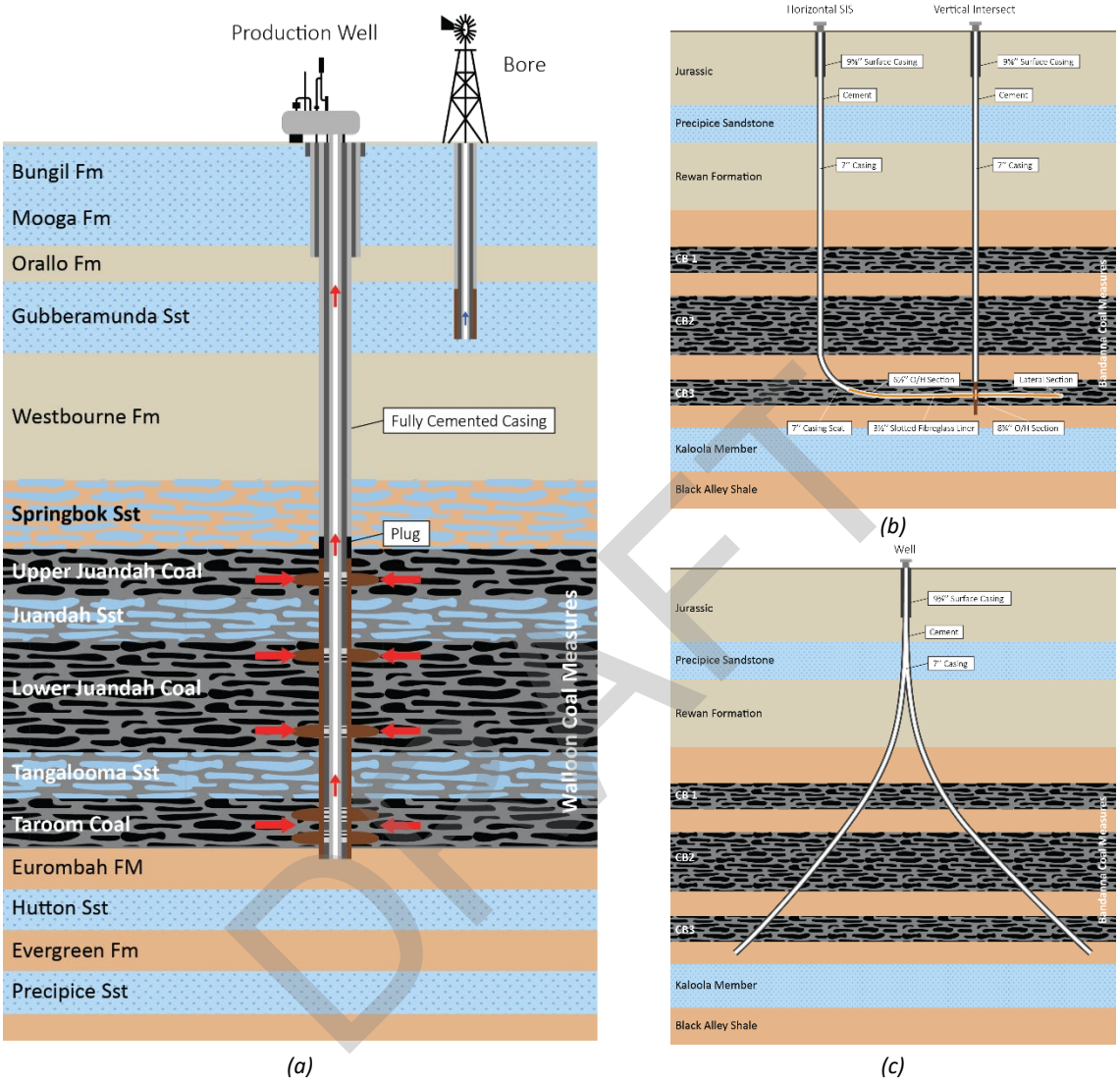

Figure 6: Schematic representation (not to scale) of CSG well trajectories, including (a) a vertical completed to access multiple seams within the Walloon Coal Measures, (b) a horizontal well drilled to intercept a vertical in a surface-to-inseam (SIS) configuration, and (c) a deviated well. Note that (b) and (c) show interception of coals within the Bowen Basin.

Hydraulic fracturing

Hydraulic fracturing is a reservoir stimulation technique used to increase the contact area between the well and the target coal seam(s). It is used to attain economic rates of production in low-permeability formations. Hydraulic fracturing does not cause subsidence. When deployed, however, it increases the spatial extent and degree of depressurisation that can be achieved from a well with naturally low deliverability, which in turn contributes to subsidence in a similar manner to that which occurs in higher-permeability, non-stimulated wells.

The widespread deployment of hydraulic fracturing was primarily responsible for the advent of the shale gas industry in the US (MIT Energy Initiative, 2011). Most CSG reservoirs exhibit sufficient permeability to negate the need for hydraulic fracturing, and thus only approximately 10% of Queensland CSG wells have been hydraulically fractured.

This rate is anticipated to increase to up to 40% as operators target more challenging formations. However, in the 2020 financial year only 12% of Queensland CSG wells were hydraulically fractured (GasFields Commission Queensland, 2021).

During hydraulic fracturing, a suspension of granular material, called proppant, is pumped into the reservoir, creating fractures that increase the volume of reservoir that is exposed to the well. This reduces the resistance to water and gas flow from the reservoir to the well and increases the rate of production. The role of the fluid is to induce stresses in the reservoir which are high enough to create a fracture and also to transport proppant. When the injected fluid is removed, the proppant remains in place to keep the fractures open. Additives are used to alter the rheology of the base fluid which increases its ability to suspend and transport particles and changes the rate of fracture growth.

Hydraulic fracturing in CSG wells is commonly deployed in multiple stages on either vertical or horizontal wells, as shown schematically in Figure 7. Vertical wells can include on the order of five to 10 stages, each targeting different coal seams at different depths, while horizontal wells can include on the order of 20 stages (or more) with the intention of increasing the stimulated reservoir volume (SRV). Indicative fluid volumes pumped per well, both vertical and horizontal, are on the order of 2 ML (Johnson et al., 2021; Pandey et al., 2017). This is in contrast to shale gas wells in Texas, which pump between 10 and 20 ML (Nicot & Scanlon, 2012).

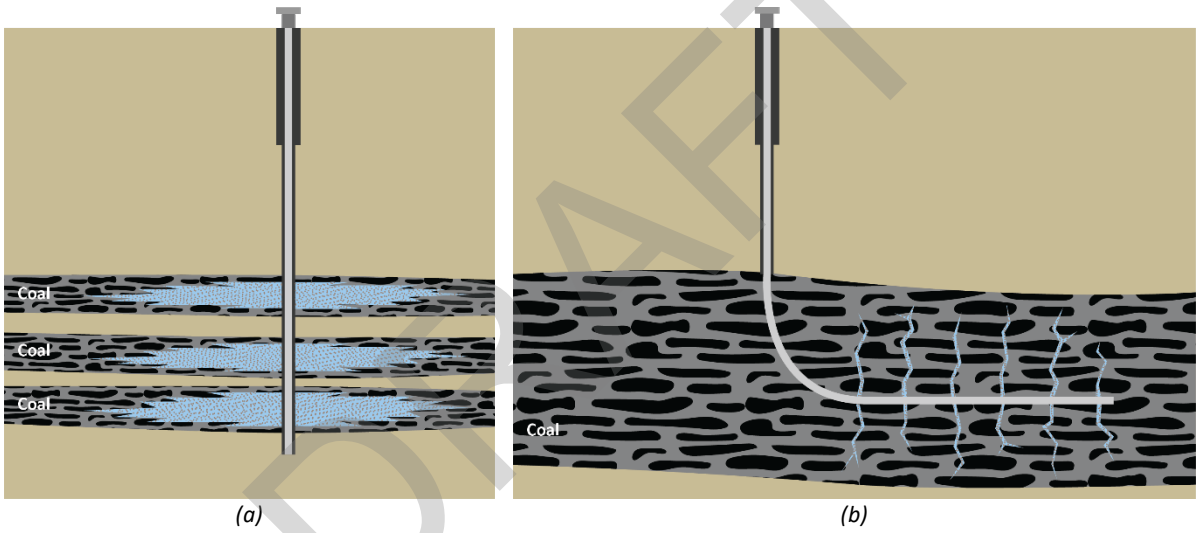

Figure 7: Schematic diagrams of multistage hydraulic fracturing in (a) a vertical CSG well and (b) a horizontal CSG well.

The direction of hydraulic fracture growth is governed by the subsurface stress regime, which is comprised of the vertical, S_V, maximum horizontal, S_H, and minimum horizontal, S_h, principal stress components. In normal faulting, $S_V > S_H > S_h$, and strike-slip regimes, $S_H > S_V > S_h$, fractures grow vertically in the plane perpendicular to the minimum horizontal stress, S_h, direction. In the reverse faulting regime, $S_H > S_h > S_V$, which is common at shallow depths in Queensland, the minimum principal stress direction is vertical and so fractures tend to grow horizontally (Busetti & Flottmann, 2018; Leonardi et al., 2019). This helps prevent propagation of fractures into aquifers above the fracturing stage. Horizontal fractures can also propagate when vertical fractures terminate at and then lubricate, for example, the interface between coal and non-coal layers. Both types of horizontal fractures can result in small, temporary uplift of the ground surface which can be measured using tiltmeter surveys of each of the well stages (Pandey et al., 2017).

Downhole pressure management

As shown in Figure 1(b), the volume of methane adsorbed to coal increases with pressure and so commercial CSG production typically requires a reduction of reservoir pressure to liberate gas. This is achieved by deploying a downhole pump to dewater the target coal formation(s). A progressing cavity pump (PCP) is installed on the tubing string close to, but not at, the bottom of the well, where it drives produced water up the central tubing of the well.

This facilitates downhole separation of water from the majority of gas, which flows to the surface via the annular gap between the well casing and the tubing. During this process, the groundwater level above the coal seam may remain largely unchanged, depending on the degree of hydraulic isolation, but the reduction in water pressure associated with groundwater abstraction from the seam promotes methane desorption (i.e. detachment from coal surfaces).

The rate of CSG associated water extraction from Surat and Bowen Basin wells within the Surat Cumulative Management Area (CMA) is summarised in Figure 8. This clearly shows the step-change in dewatering associated with the onset of CSG-LNG export. These data are collated and reported, along with future projections, by the Queensland Government's Office of Groundwater Impact Assessment (OGIA) in their series of Underground Water Impact Reports (OGIA, 2021). It has been observed that actual volumes of produced water are consistently lower than earlier industry predictions(Underschultz et al., 2018). Reasons for this include conservatism in research, regulation, and operation estimates, the use of basin-scale models that do not account for the effect of two-phase flow on near-wellbore saturation and permeability, decay of water extraction from wells with time, and installation of wells in infill locations where partial depressurisation (and potentially gas production) has already occurred (Underschultz et al., 2018).

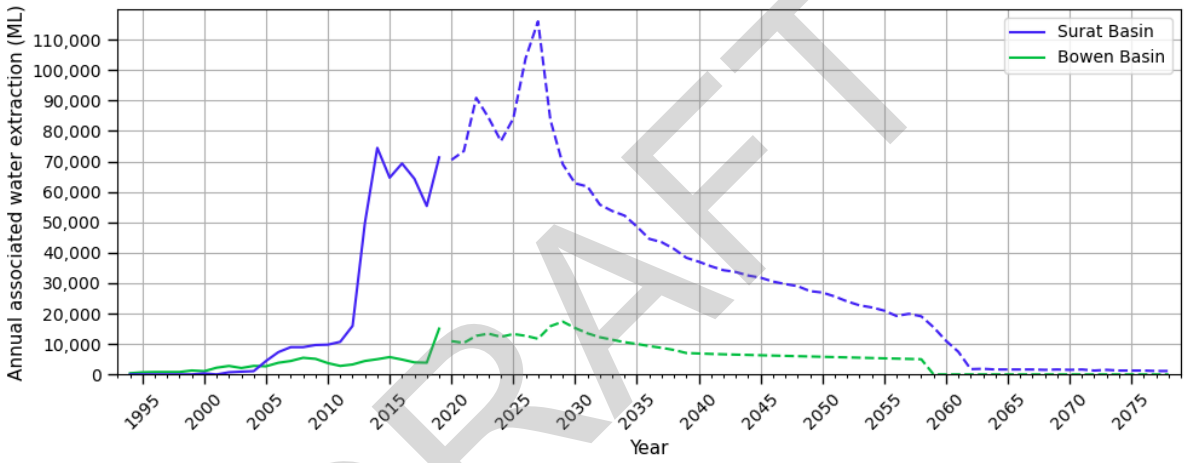

Figure 8: Annual rates of CSG-related water extraction from Surat and Bowen Basin wells within the Surat CMA (reproduced from OGIA (2021)). The dashed lines represent future projections.

The amount of water produced from an individual well is dependent on a number of factors, including the saturation and permeability of the coal, its internal connectivity and continuity, the nature of non-coal layers within the coal measures, and the regional state of water and gas depletion. Water rates are highest at the onset of production and then typically decay with time. The characteristics of methane desorption mean that the corresponding rate of gas production is initially low whilst initial depressurisation is occurring, and then increases to a peak a number of years after production commenced (see Figure 9(a)). Some Bowen Basin coals have been found to produce significantly less water than those of the Surat Basin (Towler et al., 2016), but this is possibly due to field (not basin) differences. Given the variability and uncertainty associated with the parameters that drive water production, and the spatial and temporal interaction of wells, it is almost impossible to precisely predict water production on an individual well basis.

The relationship between (pore) pressure and methane desorption from coals is not linear. This relationship is characterised using an adsorption *isotherm* test, which measures the maximum gas holding capacity of a coal sample at any particular pressure at a stable temperature. These data can then be fitted to the Langmuir equation (Langmuir, 1916),

$$V = \frac{V_L p}{p + P_L}, \quad (1)$$

where V is the maximum gas adsorption capacity at any particular pressure, p, and V_L and P_L are the Langmuir volume and pressure, respectively, which are both model parameters. Figure 9(b) presents examples of adsorption

isotherm curves for coals from the Bowen and Surat Basins (Connell et al., 2016). These curves can be used to estimate the total gas content (and saturation) of a reservoir at a certain depth (and therefore pressure and stress (Liu et al., 2017)) as well as the degree of depressurisation required for economic gas production. It is worthwhile noting that, at low pressures, more gas is desorbed per unit pressure change. In addition, the repeatability of adsorption tests is problematic, especially in the absence of a universal standard procedure, and that it is generally accepted that their uncertainty ranges from 7 to 20% (Crosdale et al., 2008; Mavor et al., 2004). Given the relationship between desorption, coal shrinkage, and compaction (see Section 3.4), these are important observations.

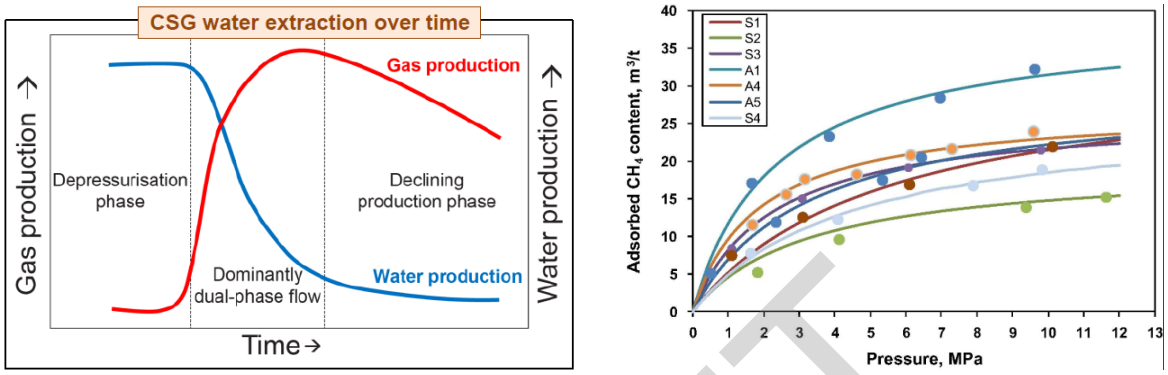

Figure 9: The relationship between water production and gas desorption and extraction showing (a) a schematic graph of the relationship between water and gas production rates and (b) the Langmuir isotherm of select Queensland coals (reproduced from Connell et al. (2016)).

Groundwater abstraction is the primary driver of subsidence in areas where CSG is produced, as discussed in Section 3.4. The historical and significant extraction of water for agriculture and other non-CSG purposes therefore presents a challenge to identifying baselines for surface elevation and rate of movement and identifying the impact of CSG production in isolation.

As mentioned in Section 3.2, CSG operations are often located beneath or adjacent to agricultural activity, which can result in real or perceived impacts to groundwater resources (OGIA, 2021). This is more acute in the Surat Basin, where intensive irrigated cropping occurs and the Walloon Coal Measures, which are the Queensland CSG industry's biggest producer, lie within the Great Artesian Basin (GAB). The GAB comprises a number of hydrogeological basins that cover an area of 1.7 million km^2. It is comprised of a series of aquifers, which exhibit a high degree of spatial variability and vertical connectivity. Within the GAB, aquifers are used to supply water to regional communities and agriculture and its importance to regional communities is emphasised by their location in low-rainfall and drought-prone areas (Towler et al., 2016). Aquifers within the GAB supply water to many regional towns (more than 30 in Queensland) with tens of thousands of bores supplying water for farming, domestic, and industrial use. They also provide irrigation water for major crops, such as cotton and grains, and horticulture. There is a long history of declining aquifer pressures through over-extraction (Smerdon & Ransley, 2012) with respect to the productive yield of the system, which has resulted in significant lowering of aquifer pressures.

3.4 Driving mechanisms of CSG-induced subsidence

In the context of gas production and the extraction of associated water from coal seams, the subsidence observed at the surface is driven by the depressurisation of the fluid bearing formation(s) beneath. Reducing the pore pressure increases the effective stress, which causes poromechanical compaction of each depressurised layer. It also promotes desorption of methane which results in *desorption-induced shrinkage*, which manifests as a reduction in the coal's bulk volume. These two phenomena are additive within a coal seam, resulting in a net change of height that can be summed over each depressurised layer. The fraction of this total compaction that propagates to the surface as subsidence is a function of the competence and thickness of the overlying and underlying strata. Similarly,

groundwater abstraction for municipal or agricultural use can also contribute to the total subsidence observed at a location. Therefore, the ability to predict future or interpret historical subsidence requires an understanding of two-phase flow in the reservoir, the porosity, permeability and relative permeability of coal, changes in effective stress and poromechanical compaction of geological units, and coal shrinkage. These facets of the problem are described in this section, while their interdependencies are shown schematically in Figure 10. It is important to note, however, that they are all active areas of research.

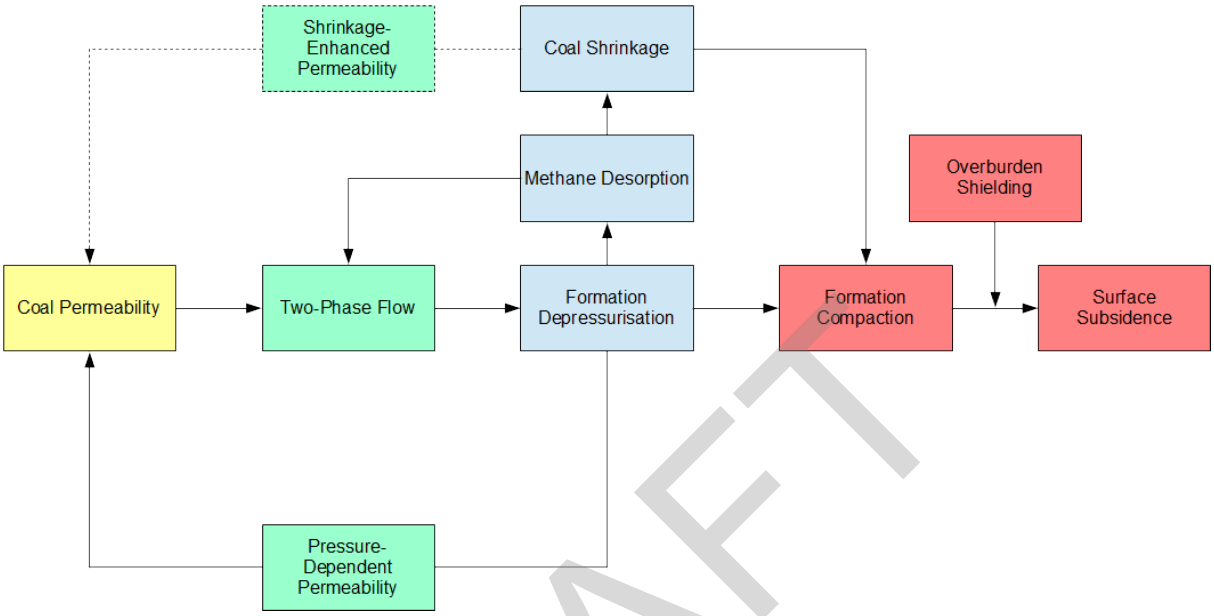

Figure 10: Schematic representation of the relationship between permeability, fluid flow, coal shrinkage, rock/coal compaction, and subsidence. Both formation depressurisation and coal shrinkage (dashed lines highlight that this is a more recent concept, subject to ongoing research) provide feedback in the system via permeability change.

Two-phase flow in a coal seam

The production of gas and water from a CSG well is described by three distinct stages (McKee & Bumb, 1987), as indicated in Figure 9(a) and described as follows.

1. At the onset of production, associated water is pumped from the coal seam to reduce pressure. In this stage, the flow is laminar and predominantly water in a saturated single-phase regime even though some free and dissolved gas may exist within the cleats and macropores of the coal.

2. After sufficient depressurisation, gas begins to desorb from the coal surface and diffuse through the matrix to the cleats, where it begins to form bubbles. The wetting characteristics of the gas-water-coal system keep these isolated bubbles trapped in the cleats, where they partially impede the flow of water towards the well. Consequently, this stage is characterised by unsaturated single-phase flow of water, but not gas.

3. Methane desorption increases with further depressurisation, resulting in the coalescence of bubbles which create a continuous pathway for gas flow within the cleats towards the well. In this stage, both water and gas are transported, which is characterised by two-phase flow in the coal seam. As production continues, the volume fraction of water and gas in the two-phase flow regime changes as the water rate decays, peak gas production is reached, and then the gas rate decays.

These stages of flow are sequenced in both time and space around a well (McKee & Bumb, 1987). Considering just the near-wellbore region, it transitions from saturated single-phase water flow to unsaturated single-phase water flow and then two-phase flow as time progresses. However, at any instant in time the degree of seam depressurisation

decreases with distance from the well, meaning that when two-phase flow occurs near the well, unsaturated single-phase water flow occurs at some distance from the well, and saturated single-phase water flow occurs at greater distance from the well.

The saturated, single-phase water flow in the seam is uncomplicated, in that it is laminar and can be modelled using Darcy's law. However, to accurately predict all regimes of gas and water flow in the seam, multiphase modelling with variable saturation is necessary. This is an important consideration, as the gas and water flow directly influences the spatial prediction of reservoir depletion, which is the key driver of subsidence. The evolution of mass and momentum balance for multiple, coexistent fluid phases in a reservoir can be modelled using a range of software packages (e.g. CMG-GEM, INTERSECT, MOD-FLOW). The Richard's equation (Richards, 1931) can also be used to approximate liquid flow in a variably saturated porous medium, in conjunction with the van Genuchten equation for saturation as a function of pressure (van Genuchten, 1980). It is important to note that this approach does not capture the diffusion of gas through the coal matrix, or the transport of the gas phase. Rather, it is assumed that desorption occurs instantaneously, making gas immediately available within cleats and macropores. More information on modelling gas-liquid systems with Richard's equation can be found in the literature (Taigbenu, 1999), including the basis for the approach taken by the Office of Groundwater Assessment (Herckenrath et al., 2015).

Porosity and permeability of coal

As described in Section 3.1, coal is a naturally fractured medium that, in the context of a natural gas reservoir, is commonly described as a dual porosity system (Clarkson & Bustin, 1999). This system is comprised of porous matrix blocks, with side lengths ranging from millimetres to centimetres, separated by face and butt cleats, which exhibit apertures ranging from micrometres to millimetres (Laubach et al., 1998). This is shown schematically in Figure 11. One of the properties that make coal such a unique material is its porosity, particularly the high specific surface area per unit volume. A single cubic centimetre of coal can contain pores with a total internal surface area of 3 m^2 (Mares et al., 2009; Radlinski et al., 2004). It has been reported (Yao et al., 2008) that the matrix pore network follows a fractal distribution, with individual pores classified by size as either micro-, meso-, or macropores (Şenel et al., 2001). A discussion of how these vary with coal rank can be found in Moore (2012). According to Gan et al. (1972), micropores have a diameter less than 2 nm, mesopores have a diameter between 2 and 50 nm, and macropores are larger than 50 nm. However, the usage of these terms is not universally consistent in the literature.

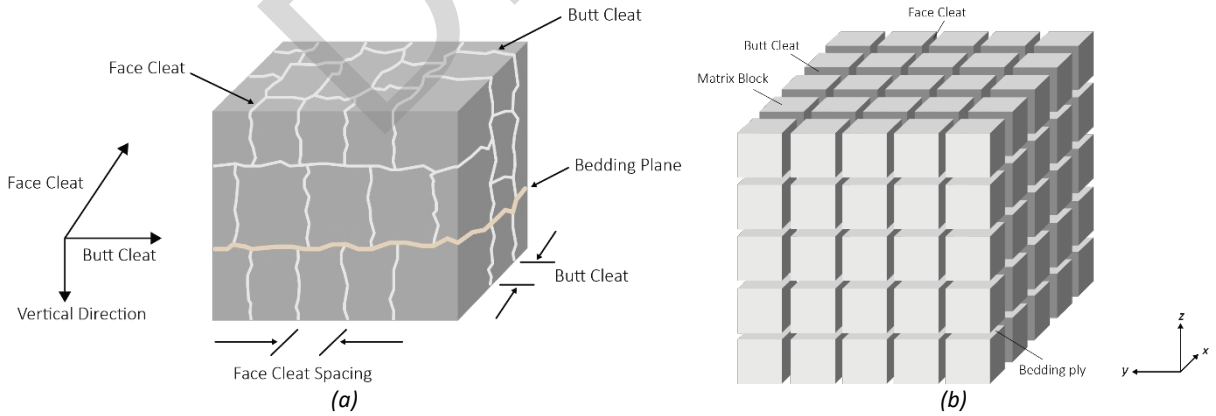

Figure 11: Schematic representation of cleats and matrix blocks in coal, showing (a) the relative orientation and termination of face and butt cleats with respect to bedding planes, resulting in anisotropic permeability, and (b) the simplification of the cleats and bedding planes as a cubic geometry (Robertson & Christiansen, 2008) resulting in isotropic permeability.

Typically, the permeability of the pore network in the matrix will be orders of magnitudes lower than that of the cleat network in the same coal. However, in the micropores and smaller mesopores (as per the above size classification), the Knudsen number of methane (which in this context is a function of reservoir pressure and temperature) would suggest that a continuum description of transport is not valid and therefore phenomenological concepts such as permeability do not apply. Consequently, it is generally assumed that gas flow through cleats is laminar and can be

described by Darcy's law, whereas gas transport in the coal matrix is controlled by a diffusive process that can be described (if it is to be included explicitly) by Fick's law. This diffusion links desorption of gas molecules from the coal to their subsequent viscous flow in cleats towards the well (Chen, 2011; Masoudian et al., 2016; Webb, 2006).

In the context of oil and gas production, coal seams are considered low-permeability reservoirs. The permeability of the cleat and natural fracture networks dominate flow behaviour (Laubach et al., 1998), as observed in the Walloon Coal Measures. In general, the properties of coal are anisotropic due to its depositional origin and the influence of the cleat network. This also applies to the *permeability tensor* because the horizontal permeability in the direction of face cleats, k_f, is typically five to ten times higher than the horizontal permeability in the direction of butt cleats, k_b, (Best et al., 2014) and the vertical permeability perpendicular to the bedding plane, k_v, is typically lower than either horizontal permeability (Massarotto et al., 2003). Therefore, rigorous prediction of gas and water transport in coal seams requires incorporation of the three principal components of the permeability tensor, which is facilitated by most commercial reservoir simulators and some groundwater modelling packages.

It has been well documented that coal permeability decreases with increasing depth, most likely because the associated increase in geomechanical stress acts to close the cleats (Enever et al., 1999; OGIA, 2016a; Somerton et al., 1975). As an indicative example, some coals can exhibit permeability on the order of hundreds of millidarcies (mD) at a depth of 100 m, which reduces to approximately 1 mD at a depth of 1,000 m. This relationship was demonstrated by Esterle et al. (2006) for coals from the central Bowen Basin and Hunter Valley although it was noted that, at any particular depth, significant permeability variation (e.g. two orders of magnitude) can exist. In addition, Bustin (1997) found that vitrain banding within some Australian coal seams had a significant effect on permeability, which was sometimes greater than that of the effective stress.

The horizontal stress regime within a basin or sub-basin affects a number of facets of CSG production. In the context of fluid flow, the effective stress, σ^e, in a basin has been shown to affect permeability (Bell, 2006; Sparks et al., 1995). The effective stress is defined as,

$$\sigma^e = \sigma - \alpha p, \quad (2)$$

where σ is the total stress, p is the pore pressure, and α is the *Biot coefficient*. The horizontal components of the net effective stress are a measure of the mechanical load on the cleats, which acts to close them. Interpreted differently, the effective stress is the difference between the reservoir pore pressure and the cleat opening pressure measured in the borehole or well (Esterle et al., 2006). As the least principal stress (i.e. the minimum effective stress) in the basin increases, permeability can decrease from nearly 10 mD at 1 MPa to less than 1 mD at 8 MPa (Sparks et al., 1995).

As a consequence of this characteristic behaviour, a number of pressure-dependent permeability models have been defined for coal (see Pan and Connell (2012) for a review). These include the works of Palmer and Mansoori (1998), Shi and Durucan (2005), and Cui and Bustin (2005), all of which assume uniaxial strain conditions (i.e. constant total vertical stress and zero lateral strain). Using the matchstick model of the relationship between permeability and porosity (Seidle et al., 1992),

$$\frac{k}{k_0} = \left(\frac{\phi}{\phi_0}\right)^3, \quad (3)$$

the Cui-Bustin permeability model can be written as,

$$\frac{k_s}{k_{s0}} = \exp\left\{\frac{3}{K_p}\left[\frac{1+\nu}{3(1-\nu)}\Delta\sigma^e - \frac{2E}{9(1-\nu)}\Delta\varepsilon^s\right]\right\}, \quad (4)$$

where K_p is the pore modulus, k_{s0} is the initial in-situ intrinsic permeability of the coal seam, E and ν are the Young's modulus and Poisson's ratio of coal, respectively, $\Delta\sigma^e$ is the incremental change in the effective stress, and $\Delta\varepsilon^s$ is the change in desorption-induced volumetric strain (i.e. shrinkage). The change in effective stress, $\Delta\sigma^e$, is equal to the negative of change in pore pressure, $-\alpha\Delta p$, assuming a constant total stress given $\Delta\sigma^e = \Delta\sigma - \alpha\Delta p$.

Note that the constant total vertical stress assumption has implications for the interpretation of saturation (i.e. water content) above the coal seam. The desorption-induced shrinkage, $\Delta\varepsilon^s$, is calculated as (Masoudian et al., 2019a),

$$\Delta\varepsilon^s = \varepsilon^s - \varepsilon_0^s = \frac{\varepsilon_L^s b_L p}{1+b_L p} - \frac{\varepsilon_L^s b_L p_0}{1+b_L p_0}, \quad (5)$$

where b_L is the Langmuir constant, ε_L^s is a constant representing the maximum volumetric swelling strain of coal, and p_0 is the pressure corresponding to the reference permeability.

The permeability-pressure relationship for the Palmer-Mansoori, Shi-Durucan, and Cui-Bustin models is compared in Figure 12(a). The difference between these models has in the past been (incorrectly) attributed to Palmer and Mansoori (1998) adopting a strain formulation, as opposed to the stress formulation adopted by Shi and Durucan (2004) and Cui and Bustin (2005) (Gu & Chalaturnyk, 2006; Li et al., 2017; Palmer, 2009). Zimmerman (2017) subsequently showed that the Palmer-Mansoori model is invalid when porosity is greater than zero or the Biot coefficient is less than one. Mathias et al. (2019) also analysed these three models by using them to derive associated expressions for the storage coefficient, the equation for which is well established for a reservoir under uniaxial strain. This found that only the Cui-Bustin model was able to reproduce the correct storage coefficient, and that issues with the Shi-Durucan model are due to inconsistencies in the theoretical derivations of both Seidle et al. (1992) and Shi and Durucan (2004). It was noted, however, that the Shi-Durucan model is often found (Shi et al., 2014; Zeng & Wang, 2017) to better fit experimental data, but this was attributed to the availability of two fitting parameters, as opposed to one in the Cui-Bustin model (Mathias et al., 2019).

In the case where both water and gas flow through a cleat or pore, the *relative permeability* is the primary parameter used to describe the flow regime. This parameter is strongly influenced by the wetting characteristics of each fluid (i.e. the preference for a fluid to coat a solid material), which are in turn a function of the nature of fluids, local coal chemistry, minerals, surface morphology, and local pressure conditions (Zhang et al., 2015). However, the subsurface is a complex system and the wetting state varies spatially. The best way to quantify the influence of this variability is an area of active research (Armstrong et al., 2021). High-fidelity computational modelling of two-phase fracture flows has recently been used (McClure et al., 2021) to study the influence of surface roughness, chemical heterogeneity, and dynamic events (e.g. Haines jumps). The quest to link these data to continuum-scale wettability indices continues (Sun et al., 2020a; Sun et al., 2020b).

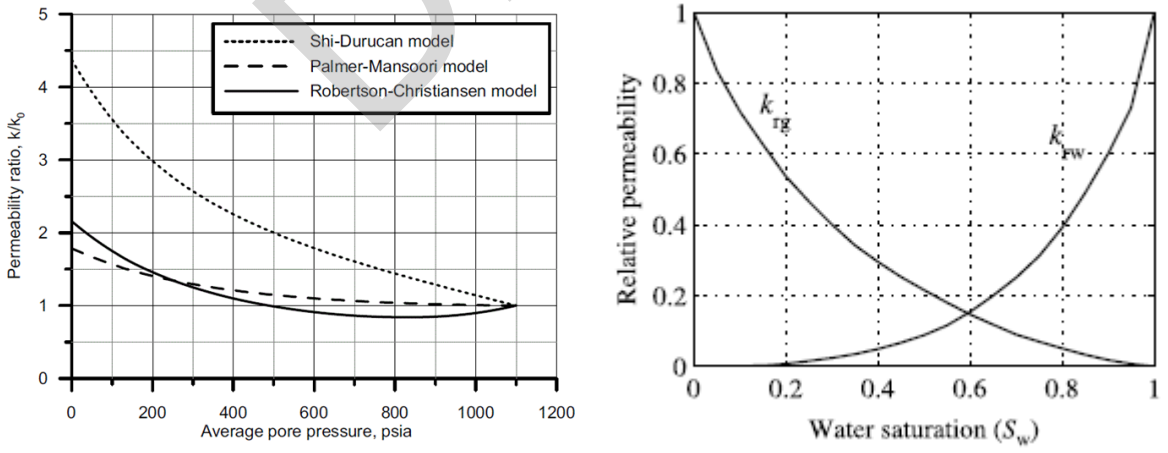

(a) *(b)*

Figure 12: Graphs of coal permeability, showing (a) a comparison of the stress-dependent permeability models of Palmer and Mansoori (1998), Shi and Durucan (2004), and Cui and Bustin (2005), and (b) the relative permeability curves of gas, k_{rg}, and water, k_{rw}, as a function of saturation (reproduced from (Gash, 1991)).

Several methods exist to measure relative permeability in the laboratory, including unsteady-state, steady-state, capillary pressure, and numerical inversion methods. A survey of the contemporary literature reveals ongoing investigation of relative permeability related to coal rank and lithotype (Mahoney et al., 2015), dynamic behaviour

(Shaw et al., 2019), history matching (Zhang et al., 2021), and more. The resulting data are used to inform curves like those shown in Figure 12(b), which describe the relative permeability of each phase as a function of saturation. It is important to note that the precision of these experimental approaches depends on the interpretation of the measured data (Zhang et al., 2015). Further, it has been observed that upscaling laboratory data to real reservoir conditions is subject to a great level of uncertainty (Müller, 2011), which propagates to predictions of gas and water production. Nevertheless, given the non-unique nature of gas-water relative permeability in coal and the complexity associated with measuring and upscaling it to that necessary for a field-scale simulator, it is common practice to choose a standard relative permeability curve and treat it as a model parameter subject to sensitivity analysis.

Poromechanical compaction

Poroelasticity defines the behaviour of a porous medium under internal and external forces. It relates the changes in internal pore pressures and external stresses to the deformation of the porous continuum and the solid frame. Reducing the pore pressure in a poroelastic, subsurface material results in poromechanical compaction, which manifests as subsidence when propagated to the surface. Groundwater abstraction, oil and gas production, and the dewatering of shallow sediments can all cause compaction and subsidence but, depending on the degree of consolidation of the geological unit(s), these can differ by orders of magnitude per unit drop in pressure.

The withdrawal of water from a porous geological unit results in a commensurate decline in the water level or hydraulic head. The largest decline in the formation exists at the point of extraction and decreases with increasing distance from the well. As the pore pressure in the formation decreases the effective stress increases proportionally and in unconsolidated sediments this can result in the rearrangement of grains, reduction of porosity, and ultimately subsidence. In some areas, where the formation is shallow and unconsolidated and groundwater extraction is extensive, this effect can become acute. For example, there are reports of up to 9 m of subsidence in Mexico City over regions of groundwater extraction from interbedded sand and clay layers (Ortiz-Zamora & Ortega-Guerrero, 2010). However, subsidence of this magnitude is not typical for oil and gas extraction, particularly CSG, because the depressurised geological units are consolidated and less susceptible to grain-scale deformation. They also exist hundreds or thousands of metres below the surface and so, depending on the lateral extent of the depleted zone and the stiffness of the overlaying geological units, the overburden may experience stress arching (Dusseault et al., 2007) or compaction driven surface deformation (Dusseault & Rothenburg, 2002; Geertsma, 1973; Hettema et al., 2002). The extent of deformation observed at the surface depends on multiple factors, which include:

1. Rock mechanical properties of the geological unit as well as the overburden and basement units;
2. The lateral and vertical extent of the compression causing matrix compaction, and;
3. Magnitude and orientation of the compaction with respect to vertical.

The magnitude of subsidence mainly depends on the depth and thickness over which depressurisation and compaction occurs, and the properties of geological units overlying the compacting geological units. Assuming that the mechanical behaviour of a rock or coal layer can be described by linear poroelasticity, the relationship between stress and strain can be modelled using Hooke's law. The normal strain in the three Cartesian directions can be written in terms of the effective stresses as,

$$\varepsilon_{xx} = \frac{1}{E}\left[\Delta\sigma^{e}{}_{xx} - \nu\left(\Delta\sigma^{e}{}_{yy} + \Delta\sigma^{e}{}_{zz}\right)\right], \quad (6)$$

$$\varepsilon_{yy} = \frac{1}{E}\left[\Delta\sigma^{e}{}_{yy} - \nu\left(\Delta\sigma^{e}{}_{xx} + \Delta\sigma^{e}{}_{zz}\right)\right], \quad (7)$$

$$\varepsilon_{zz} = \frac{1}{E}\left[\Delta\sigma^{e}{}_{zz} - \nu\left(\Delta\sigma^{e}{}_{xx} + \Delta\sigma^{e}{}_{yy}\right)\right]. \quad (8)$$

Assuming uniaxial strain conditions means that $\varepsilon_{xx} = \varepsilon_{yy} = 0$ and total vertical stress, σ_{zz}, is constant. After some manipulation (see Wu et al. (2019) for more details), an explicit equation for the strain in the vertical direction, ε_{zz},

can be derived and interpreted as the ratio of the change in height, Δh, and original height, H, of the target formation,

$$\frac{\Delta h}{H} = \varepsilon_{zz} = -\frac{1}{E}\frac{(1+\nu)(1-2\nu)}{(1-\nu)}\Delta\sigma^{e}{}_{zz} \quad (9)$$

Substituting for the effective vertical stress and extracting the layer compressibility (see Section 8.2),

$$C_m = \frac{(1+\nu)(1-2\nu)}{E(1-\nu)}, \quad (10)$$

results in,

$$\Delta h = C_m H \alpha \Delta p_f \quad (11)$$

The summation of Δh values for all depressurised layers gives an indication of the maximum subsidence expected at the surface due to poromechanical compaction.

The assumption of uniaxial strain is appropriate because the subsidence due to poromechanical compaction is primarily vertical. Formation heterogeneity, both in terms of geometry and permeability (i.e. propensity for depressurisation), can result in non-uniform compaction of a geological unit. At the surface, this can manifest as variation in subsidence as well as net horizontal movement. Extreme cases of differential surface movement, vertically or horizontally, could induce ground failures such as surface faults and earth fissures (Holzer, 1984). However, neither presents a significant risk in the context of CSG production (see Section 5.2 for discussion).

In unconsolidated sediments, where grain rearrangement can occur, the rate of poromechanical compaction is greatly influenced by the lithology. Larger-grained sand and gravel formations undergo faster rates of compaction, even though the extent of total compaction is limited. Fine-grained, saturated lithological units, such as clays and fine siltstones, on the other hand, compact at a very slow rate. The compaction (or uplift) in these low-hydraulic conductivity materials is time-dependent and could take several years before the completion of the whole process (Budhu et al., 2014).

It is important to note the potential for inelasticity, and subsequent irreversibility, in compaction associated with pressure cycling of a formation. This occurs when the effective stress increases to greater than the pre-consolidation stress, and is most significant in unconsolidated and loosely-consolidated sediments. Budhu et al. (2014) used a coupled groundwater flow-soil deformation model to investigate ground movements from aquifer recharge and recovery in Arizona, USA. The cyclic groundwater withdrawal and recharge-related subsidence and uplift clearly elucidated the hysteresis in the process. In areas of CSG production, where aquifers have a prolonged history of excessive depressurisation, this suggests that historical, irreversible subsidence may have already occurred.

Desorption-induced shrinkage

One of the key differences between the geomechanical behaviour of coal seams and conventional reservoirs is that the adsorption and desorption of gas lead to swelling and shrinkage of the coal matrix, respectively (Larsen, 2004; Saghafi et al., 2007). This behaviour manifests as volumetric strain that is analogous to the thermal expansion and contraction of materials, and distinct from elastic and poroelastic behaviour. Under the common assumption of uniaxial strain, desorption-induced shrinkage has an effect on the change in effective stress and permeability (via cleat aperture) caused by depletion (Masoudian, 2016). While reservoir models consider the shrinkage phenomenon when investigating the variation of the fracture aperture and subsequently the fracture permeability (as discussed in earlier in this section), many geomechanical models neglect or at best oversimplify its influence on the bulk volumetric response of the coal seam and consequently the displacement of the ground surface (Masoudian et al., 2016; Wu et al., 2018). Nevertheless, the total displacement at the ground surface is the sum of all compaction mechanisms occurring within multiple geological units. It is dependent on the magnitude and direction of compression (which are dictated by pressure changes from extraction of associated water and desorption of gas from

coal seams), the depth and depth-interval over which compression occurs, and the geomechanical properties of the geological units throughout the entire depth profile. Whilst the desorption-induced shrinkage of coal is well understood at the laboratory scale, including the stress-dependence of the processes at work (Liu et al., 2017), the degree to which this behaviour translates to the reservoir scale in CSG production is an ongoing area of research.

The rate of coal shrinkage or swelling with pressure change can be measured experimentally (see, for example, Dudley et al. (2019)). This is usually undertaken using small coal samples (i.e. matrix blocks) to eliminate the effect of cleats that exhibit much greater compressibility than the matrix. The data are then fitted to the Langmuir equation to describe the volumetric shrinkage strain, ε^s, as a function of pressure, p,

$$\varepsilon^s = \frac{\varepsilon_L^s b_L P}{1+b_L P}, \quad (12)$$

where b_L is the Langmuir constant and ε_L^s is a constant representing the maximum volumetric swelling strain of coal at infinite pore pressure. As described in Masoudian et al. (2016b), the desorption-induced shrinkage can be incorporated as an additional term in the elastic stress-strain constitutive equations. By again invoking the uniaxial strain assumption, the net shrinkage in the vertical direction, Δh_s, can be defined as,

$$\Delta h_s = \frac{\varepsilon_L^s b_L}{(1+b_L P)(1+b_L P_0)} \Delta p_f H, \quad (13)$$

in a similar manner to that for poromechanical compaction in Equation 11.

It is pertinent here to consider the relationship between the adsorption isotherm (Equation 1) and the sorption strain (Equation 12) for a particular coal sample. Just as the former has been noted to vary considerably for different coal types and ranks, the same is true for the latter (although considerably less shrinkage data are publicly available). In addition, both equations have the same characteristic form, resulting in an increase in the rate of change of desorbed gas or shrinkage with respect to pressure as the pressure decreases. In the context of subsidence, this suggests that the desorption-induced shrinkage component of coal seam compaction may increase as the reservoir pressure approaches its end state. This has been reported internally by the industry (Rai & Hummel, 2019), however, no evidence to support or refute this observation can currently be found in the literature.

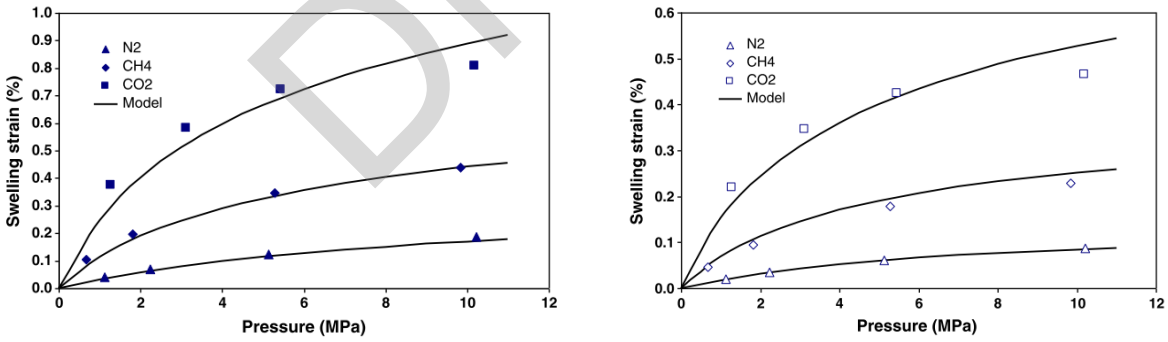

Figure 13: The volumetric swelling/shrinkage strain for a Hunter Valley coal sample when injected with N_2, CH_4, and CO_2, showing (a) the strain perpendicular to bedding, and (b) the strain parallel to bedding (Pan & Connell, 2011).

Due to their depositional nature, coal seams contain bedding planes that are approximately horizontal and perpendicular to the face and butt cleats. Consequently, coal at the bulk scale is completely anisotropic (Saurabh & Harpalani, 2019). This can be simplified for the purpose of flow modelling to assume that properties in the horizontal direction are uniform and the coal is thus transversely isotropic (Espinoza et al., 2015; Liu et al., 2016; Wang et al., 2014). Laboratory studies (Day et al., 2008; Pan & Connell, 2011) have shown that this concept of transverse isotropy also applies to desorption induced shrinkage. The work of Day et al. (2008) showed that when injected with supercritical CO_2 the expansion in the direction perpendicular to the bedding plane is 70% greater than in the parallel plane for two coal samples from the Hunter Valley and Bowen Basin, and approximately 30% greater

for a sample from the Illawarra. The Illawarra coal sample was higher rank, with a mean vitrinite reflectance of 1.29%, while the mean vitrinite reflectance was 0.89% and 0.95% for the Hunter Valley and Bowen Basin samples, respectively. These results indicate that lower rank coal tends to show stronger anisotropic swelling. Pan and Connell (2011) investigated the effect of different gasses on a Hunter Valley coal sample and revealed that the swelling strain in the direction parallel to the bedding was approximately 47%, 52%, and 60% of that in the direction perpendicular to the bedding for N_2, CH_4, and CO_2 adsorption, respectively. These results can be seen in Figure 13, where it can also be seen that swelling behaviour for different gases varies significantly but in a similar order to adsorption.

If the constants ε_L^s and b_L have been determined perpendicular to bedding (i.e. in the approximately vertical direction) they can be used directly in a uniaxial prediction of shrinkage (i.e. Equation 13). However, anisotropic shrinkage will have implications for the calculation of effective horizontal stresses, and the permeability derived from them (e.g. Equation 4), or in more complicated models in which a fraction of the total volumetric shrinkage strain is apportioned to permeability change and the rest is assigned to bulk shrinkage (Wang et al., 2014).

3.5 Considerations for shale gas and underground coal gasification

A literature search did not uncover any published research on subsidence associated with shale gas production. It has not emerged as an issue of interest in the widespread shale gas industry in the USA. Shale is significantly less compressible than coal and does not contain adsorbed gas to the extent that coal does. It is therefore not prone to poromechanical compaction or desorption-induced shrinkage, which probably explains the dearth of papers on the topic.

Underground coal gasification (Bhutto et al., 2013) necessitates the creation of a substantial underground void as the coal combusts. In this way it is more closely linked with underground coal mining methods and is therefore out of the scope of this document.

3.6 Beneficial aquifer injection and associated uplift

The associated water produced from CSG operations can be treated and injected into the subsurface to replenish depleted aquifers and, consequently, raise the groundwater table or pressure (Hayes et al., 2020). This process is known as managed aquifer recharge (MAR). One local example of this is the Reedy Creek project managed by Origin Energy (upstream operator for the Australia Pacific LNG joint venture), in which produced water is pumped into the Precipice Sandstone aquifer within the Surat Basin. In general, injection pressures are subject to limits so as to minimise the risk of creating new underground fractures which can damage aquitards and result in the unwanted hydraulic connectivity of geological units. As a consequence of the poromechanical behaviour described in Section 3.4, MAR has been associated with observed uplift of the ground surface, however the author is unaware of any public documentation of this phenomenon related to Queensland CSG activities. The elevation of pore pressure in the proximity of faults can be associated with elevated risk of induced seismicity (Ellsworth et al., 2019; Zang et al., 2014). However, injection into high-permeability formations means that the pressure diffuses and does not localise around the injection site.

Globally, there are a number of reported cases of surface uplift, ranging from millimetres to tens of centimetres, occurring over the time scale of a few months to a number of years. At Long Beach, California, land subsidence caused by hydrocarbon production was mitigated by pumping water in a controlled and well-monitored program which began in 1958 (Rintoul, 1981). The target Wilmington oil field (see Section 4.2 for more information) is made up of unconsolidated loose silty to sandy formations interbedded with shale layers (Mayuga & Allen, 1969). To mitigate the surface subsidence of as high as 9 m (Colazas & Olson, 1983), around 175,000 m^3/day of water (both from the sea and from oil production) was injected in the 1960s (Mayuga & Allen, 1969), which was later cut back to 90,000 m^3/day (Otott Jr & Clarke, 1996). A significant drop in the subsidence area was observed and for most of the field, subsidence was stopped. The subsidence rate in the middle portion of the reservoir was brought down from

71 cm/yr in 1951 to zero by 1968. In other parts, an uplift of approximately 33 cm was observed. In some parts of the field an uplift of approximately 20 cm above the original ground elevation was identified due to over injection (Colazas & Olson, 1983).

It is important to note the potential for inelasticity, and subsequent irreversibility, in compaction associated with aquifer pressure cycling. As one example, Chen et al. (2016) presented the estimation of skeletal storage coefficients and the temporal lag between subsidence measurements and head change using a combined analysis of InSAR (see Section 6.1 for a discussion of this technique) and well data. InSAR data were also used to estimate aquifer head over a broader region in the presence of significant decorrelation due to vegetation, as this is where monitoring wells are usually located. One of the key findings of this work was that the surface movement-aquifer pressure relationship was elastic, with a negligible amount of inelastic compaction observed. Surface movement data showed subsidence of up to 7.1 cm followed by uplift of up to 9.5 cm in the same location. The cyclical nature of the data suggested that the subsidence is associated with water abstraction during the summer and recharge during the winter. However, reducing the head below the pre-consolidation head will result in the inelastic compaction of clay units, which in turn results in an irreversible loss of water storage due to pore collapse and permanent drainage.

4. National and International Context

Causes of subsidence include groundwater abstraction, conventional oil and gas production, drainage of shallow soils, underground mining, earthquakes, and natural compaction such as that caused by sinkholes, peat oxidation, or thawing permafrost. Subsidence associated with CSG production simultaneously combines two of these processes, namely the depressurisation of geological units and the depletion of gas reservoirs. Mechanical sources of subsidence, such as the creation of a void during underground mining, are addressed in the companion to this document (Hebblewhite, 2022).

4.1 Subsidence due to groundwater abstraction

The development of subsidence in response to groundwater abstraction has been documented extensively in the literature. Gambolati and Teatini (2015) summarised a number of locations worldwide where the removal of groundwater had resulted in or was continuing to (at the time of publication) cause subsidence. A selection of these case studies is listed in Table 1.

Table 1 A selection of worldwide examples of subsidence caused by groundwater abstraction.

Location	Maximum Subsidence (m)	Recent Subsidence Rate (cm/yr)	Depth of Pumping (m)	Area of Subsidence (km^2)	Principal References
San Joaquin Valley	10 (1930–)	30 (2007–2011)	60–600	13,500	Galloway et al. (1999) Borchers and Carpenter (2014)
Mexico City	13 (1960–)	30 (2007–2011)	0–350	250	Ortiz-Zamora and Ortega-Guerrero (2010) Chaussard et al. (2014)
Jakarta	4.1 (1974–2010)	26 (2007–2011)	40–240	660	Ng et al. (2012)
Tokyo	4.3 (1900–1975)	−0.3 (1991–2005)	0–400	3,400	Ling et al. (2009)
Ho Chi Minh	0.4 (1996–2005)	4 (2006–2010)	50–240	250	Erban et al. (2014)
Venice	0.12 (1952–1973)	0.1 (2008–2011)	70–350	150	Gambolati (1974) Teatini et al. (2012)

Data sourced from Gambolati and Teatini (2015)

One of the greatest changes in land surface as a result of groundwater extraction was observed in the San Joaquin Valley, USA, where over 13,000 km^2 of agricultural land was affected by approximately 10 m of subsidence over 50 years. Beyond this extreme, there exists numerous examples of groundwater withdrawal for water supply, industrial use, and irrigation causing irreversible damage and land subsidence in over 60 countries around the world. Between

1975 and 2015 in the Houston-Galveston region, Texas, subsidence of approximately 1 m was measured (Kasmarek, 2012). In the Tongchuan region of China, 20 mm of subsidence occurred during the extraction of water between 2005 and 2009 (Wei et al., 2017). In the period from 1992 to 2002 in Venice, Italy, land movements varied from 2 mm/year uplift to 10 mm/year subsidence (Tosi et al., 2009). In the Mekong Delta, Vietnam, the hydraulic head decline as a result of pumping was on average 0.3 m/year resulting, on average, in 1.6 cm/year land subsidence (Erban et al., 2014). In Long Island and Galveston, Gulf of Mexico, 7.59 mm/year and 4.7 mm/year subsidence was recorded, respectively, for the recent time period (Kolker et al., 2011).

Examples of land subsidence in Australia as a result of groundwater extraction include the Latrobe aquifer (see Section 4.3) in the Gippsland Basin, Victoria (2 m subsidence), and the Lower Namoi valley in NSW. Ali et al. (2004) modelled the predicted subsidence in the Lower Namoi Valley, NSW, where groundwater extraction and crop irrigation have been occurring for approximately 60 years. A singular subsidence maximum of 0.5 m was found, however subsidence in the range of 0.05 to 0.3 m was more widely spread. This is consistent with the work of Ross and Jeffrey (1991), which reported subsidence of 0.07 m to 0.21 m in the period from 1981 to 1990. This study also found that groundwater drawdown can cause residual compaction (40 m drawdown caused land subsidence of 0.16 m) for a long period of time after the groundwater levels have stabilised (i.e. there can be a temporal lag between depressurisation and subsidence).

To summarise this brief discussion of examples, it can be seen that there are approximately two orders of magnitude difference between the subsidence observed in the San Joaquin Valley, USA, and Venice, Italy. However, in combination with rising sea levels, the comparatively small amount of subsidence in Venice comes with disproportionately high consequences (i.e. flooding of urban streets and buildings with tidal fluctuations). Therefore, it is important to note that the absolute magnitude of subsidence is not the sole driver of the impacts it generates (see Section 5.2 for further discussion of this point). It is also important to note that groundwater abstraction (e.g. for municipal or agricultural use) in areas of CSG production will also contribute to the subsidence at those locations, which complicates the assessment, measurement, and attribution of the CSG-induced component.

4.2 Subsidence due to oil and gas production

Subsidence associated with conventional oil and gas production is driven by the same mechanism as in groundwater abstraction. The extraction of fluids from the reservoir reduces the pore pressure, which results in an increase in effective stress. This manifests as increased mechanical force on the porous skeleton of the reservoir, which causes compaction that propagates to the surface. The first documented case of subsidence caused by hydrocarbon production is generally assumed to be the Goose Creek oilfield on the Texas coast of the Gulf of Mexico (Pratt & Johnson, 1926), where surface faulting and roadway subsidence was first noticed in 1918.

The brief review of compaction and subsidence associated with the petroleum industry by Nagel (2001) stated that hundreds, if not thousands, of academic and industrial documents have been published on the topic of oil and gas-related subsidence, with many dedicated to the analysis of a specific field. A survey of the contemporary literature shows that this number has continued to grow, as the challenges (and opportunities) that arise from subsidence are explored. It is prudent to note that reservoir *compaction drive* has the potential to provide a significant portion of the total drive energy of some reservoirs, resulting in increased production and ultimate recovery (Nagel, 2001).

A very small subset of subsidence cases related to oil and gas production from around the world is summarised in Table 2, including the Groningen natural gas field which is located in the northeastern part of the Netherlands. It is estimated that Groningen contained 97 tcf of technically recoverable natural gas, making it the largest natural gas field in Europe and one of the largest in the world. It can be seen in Table 2 that the maximum subsidence at Groningen is at least one order of magnitude smaller than that in the other fields listed. Nevertheless, subsidence on the order of tens of centimetres represented a serious challenge to the operation of the field as large parts of the

Netherlands are below sea level and protected by dikes. From the 1980s, production-induced subsidence was also accompanied by an increased level of seismicity (van Elk et al., 2017).

To help monitor subsidence above Groningen and calibrate predictive models of future movement, 16 levelling campaigns were undertaken in the period from 1964 to 2018. These data were used to forecast accumulated subsidence at 2025, 2031, and 2050 for a number of different operational scenarios (TNO, 2021) which decrease production to zero no later than 2030. Figure 14 shows a comparison of subsidence predictions and measurements for the period 1972 to 2018, clearly showing a subsidence bowl with a maximum magnitude of approximately 35 cm in the centre. Good correspondence between the predictions and measurements can also be seen. Future predictions indicate that the maximum at the centre of the bowl will reach 42 cm by 2031 and then not change significantly by 2050. At the time of writing (2023), production from the Groningen field is scheduled to cease before reserves have been exhausted because of the challenges presented by induced seismicity. Damage associated with subsidence is still possible due to differential movement of the phreatic groundwater level with respect to the surface.

Table 2 Selected worldwide subsidence examples caused by conventional oil and gas production.

Location	Maximum Subsidence (m)	Reservoir Thickness (m)	Reservoir Depth (m)	Principal References
Ekofisk Field, North Sea	6.0 (1971–1998)	Up to 300	>3,000	Smith (1988) Sulak et al. (1991)
Bolivar Coastal Fields, Venezuela	5.0 (1929–1988)	Up to 180	>300	Escojido (1981) Finol and Sancevic (1995)
Wilmington Field, California	9.0 (1932–1968)	800–2,000	700–1,800	Mayuga (1970) Mayuga and Allen (1970)
Groningen Field, Netherlands	0.3 (1972–2018)	120–270	~3,000	Schoonbeek (1976) TNO (2021)
Po Delta, Italy	3.2 (1951–1973)	Up to 600	100–600	Cassiani and Zocatelli (1998)

Data sourced from Nagel (2001)

Outside of Australia, there exists little documented discussion of subsidence associated with CSG production. Grigg and Katzenstein (2013) reported on InSAR observations of subsidence above CSG operations in the Powder River Basin, Wyoming. The data indicated that in the periods from July 1997 to July 2000 and August 2004 to July 2007, up to 4.7 cm and 8.3 cm of subsidence occurred, respectively. In this location, groundwater was reported to have been extracted at a rate of approximately 355 ML/day. In the east-central part of the study area, the largest subsidence values were found to be correlated with large clusters of CSG wells. In comparison to the typical CSG operation in the Bowen Basin, the target Powder River Basin seams are thick (between 7 and 22 m, with an average of 11 m), shallow (depths ranged from 140 to 460 m), and low-rank sub-bituminous. In contrast to these observations, Best et al. (2014) reported on predictions made by Case et al. (2000) using a simplistic formula for subsidence and an aquifer storage coefficient of 1×10^{-4} for the coal seam. The results suggested a total subsidence of less than 13 mm in the Gillette area of the Powder River Basin. It was also estimated that only a part of this compaction would be seen at the surface. In addition, the compaction of overburden was not included in the assessment and therefore this would have contributed to the underprediction of total subsidence. More recently, Du et al. (2018) reported on the use of InSAR to monitor subsidence in the Liulin District, China, during 2003 to 2011.

The observation of both low rates of subsidence and uplift across the region led to the conclusion that CSG production was not appreciably contributing to the signal (see Section 6.4 for more detail).

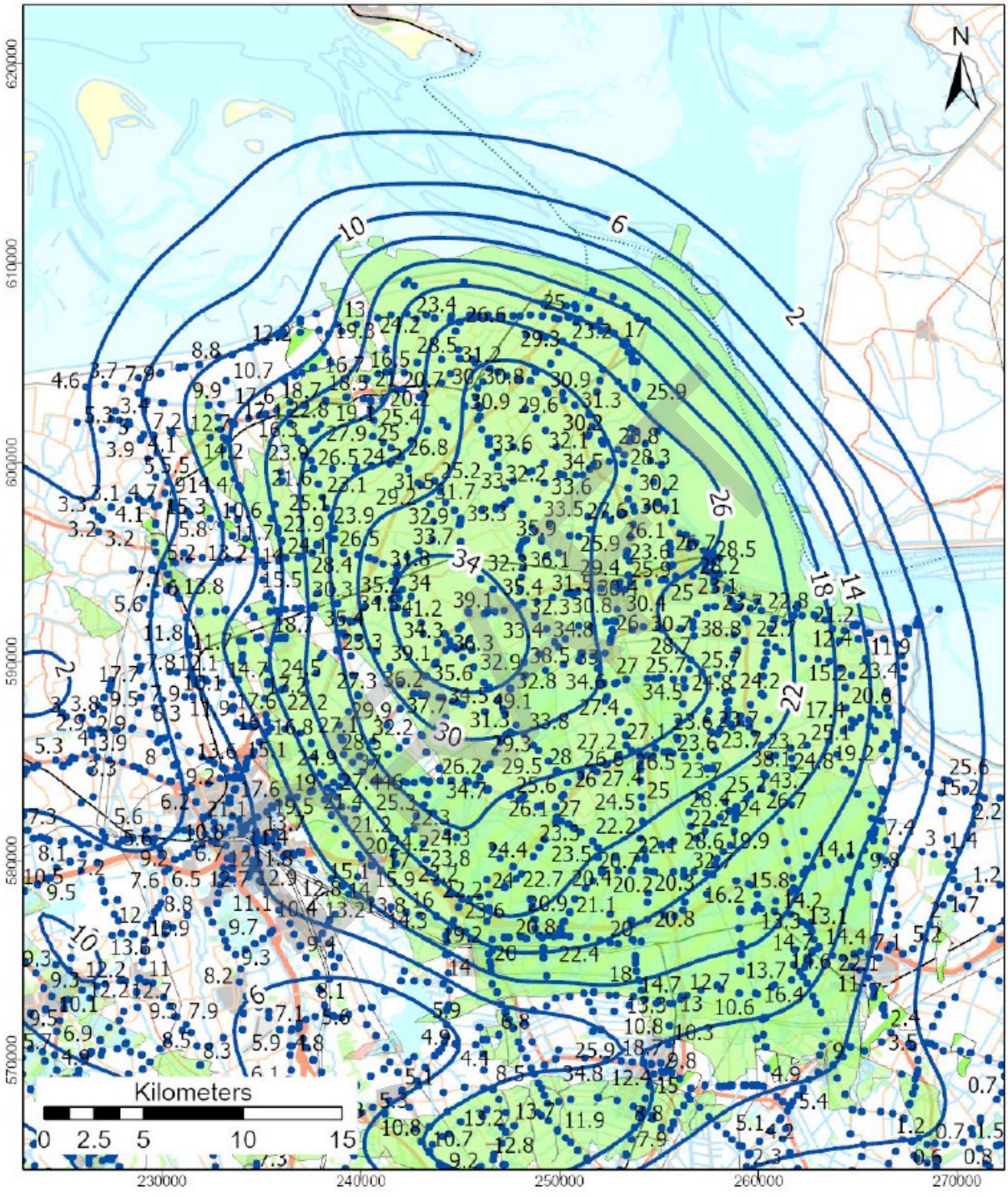

Figure 14: Predictions (solid blue contour lines) and measurements (labelled dots) of subsidence in centimetres above the Groningen gas field, Netherlands, in the period 1972 to 2018 (TNO, 2021).

4.3 Subsidence in the Australian context

Over the past five years, an increasing amount of subsidence data related to CSG developments has become available in the academic and industrial literature. Work related to modelling and prediction is discussed in Section

9.1 of this document, while work related to monitoring is presented in Section 6.4. Beyond this, there exists reports of land subsidence related to mining and the extraction of associated water. The subsidence occurring as a result of mining extraction is mainly related to the void being created due to the removal of coal, and to a lesser extent due to withdrawal of associated water. In most subsidence predictions of this kind, the subsidence as a result of water extraction is not considered.

The Gippsland Basin

The Gippsland Basin is located in southeast Victoria and has both an on-shore and off-shore component. On-shore, the basin is bounded by the Eastern Highlands in the north and the Strzelecki Ranges to the west and it extends southeast off-shore into Bass Strait. On-shore, the sediments reach more than 1,000 m thickness and they further thicken off-shore to more than 3,000 m. The Gippsland Basin contains vast brown coal resources that have been mined on-shore mainly in the Latrobe Valley and it represents Australia's primary source of liquid hydrocarbon production with conventional oil and gas reservoirs occurring mainly off-shore. Finally, the basin has unconventional hydrocarbon potential and contains significant groundwater resources mainly used on-shore for agricultural purposes and municipal water supply. The sediments themselves are composed of sands, clays, limestone and coal with some volcanics and there is a substantial documentation of the stratigraphy in the literature (Hocking, 1980; Holdgate & Clarke, 2000; Thompson & Walker, 1982).

One of the main aquifer systems in the Gippsland Basin is the Latrobe Group. Onshore this aquifer system is utilised for agriculture, it is dewatered in the Latrobe Valley in the vicinity of coal mines and it is the same strata that are produced for oil and gas in the off-shore (Holdgate et al., 2003). The cumulative effects of fluid extraction since the 1960s for agriculture, coal mining, and oil and gas production have led to a regional decline of water levels in the Latrobe Aquifer system. Hydrographs of the coastal area of the Gippsland Basin (Hatton et al., 2004) show water level declines ranging from 0.25 to 1.2 m/yr over about 30 years. Hatton et al. (2004) identified the main potential impacts of the declining water levels to be water availability to landowners with declining bore water levels and a risk of subsidence. This led to further study by Freij-Ayoub et al. (2007) who simulated the risk of coastal subsidence due to declining water levels and in parallel the Victorian Department of Primary Industries (DPI) conducting a field study of high-resolution GPS ground elevation measurements at 15 stations across the region.

Within the region of the Latrobe Valley open pit coal mining, there is substantial dewatering of the Latrobe Aquifer systems to keep the mines dry. Hatton et al. (2004) noted that in the immediate vicinity of the mine there has been cumulative subsidence measured of up to 2.3 m. This is a net result of mining and groundwater decline so cannot be attributed solely to water extraction. Coastal areas of the Gippsland Basin are, however, solely affected by water level decline. Freij-Ayoub et al. (2007) conducted geomechanical numerical simulation of this region to forecast land subsidence to the year 2056. The authors used several different methods, each with different assumptions, and followed the work of (Acar Yalcin & El-Tahir El-Tahir, 1986) where mechanical stiffness increases with confining pressure according to a power law with exponent 0.2 to 0.5. A second method (Helm, 1976) suggested scaling the skeletal specific storage coefficient down as the effective vertical stress increases.

The results of the geomechanical modelling by Freij-Ayoub et al. (2007) were compared with actual available data measured by the Victorian DPI from 15 high-resolution GPS ground elevation stations from June 2004 to November 2005. The geomechanical modelling (calibrated to measured data) showed on the order of zero and 15 mm subsidence over the period of June 2004 to November 2005 by both the numerical simulation and the field measurements. Freij-Ayoub et al. (2007) then used this calibration period to forward forecast potential subsidence to 2056 and produced a map of cumulative values ranging up to approximately 0.5 m by 2031 along the Gippsland coastline (see Figure 15).

Since the work of Freij-Ayoub et al. (2007), there has been further investigation into the contemporary hydrodynamics of the Gippsland Basin with Michael et al. (2013) examining further the distribution of Latrobe

Aquifer drawdown, the transient location of the freshwater wedge that extends from the onshore recharge areas into the offshore, and the potential of the offshore regions to store CO_2. In addition, Ng et al. (2015) used InSAR data acquired between 2006 and 2011 to investigate observable land surface movement over the whole Gippsland Basin region. They compared results with previously published reports, including the predictions to 2031 of Freij-Ayoub et al. (2007). The work showed that 98% of the measurement points from InSAR across the whole basin fall within ±10 mm/year surface movement. In the Gippsland coastal area, the InSAR data are in general agreement with the high-resolution GPS data of the Victorian DPI and by 2011 (latest InSAR data examined) were not indicating the cumulative subsidence predicted by Freij-Ayoub et al. (2007) for the forward projection to 2031. Freij-Ayoub et al. (2007) did mention, however, that the initial subsidence rate was low.

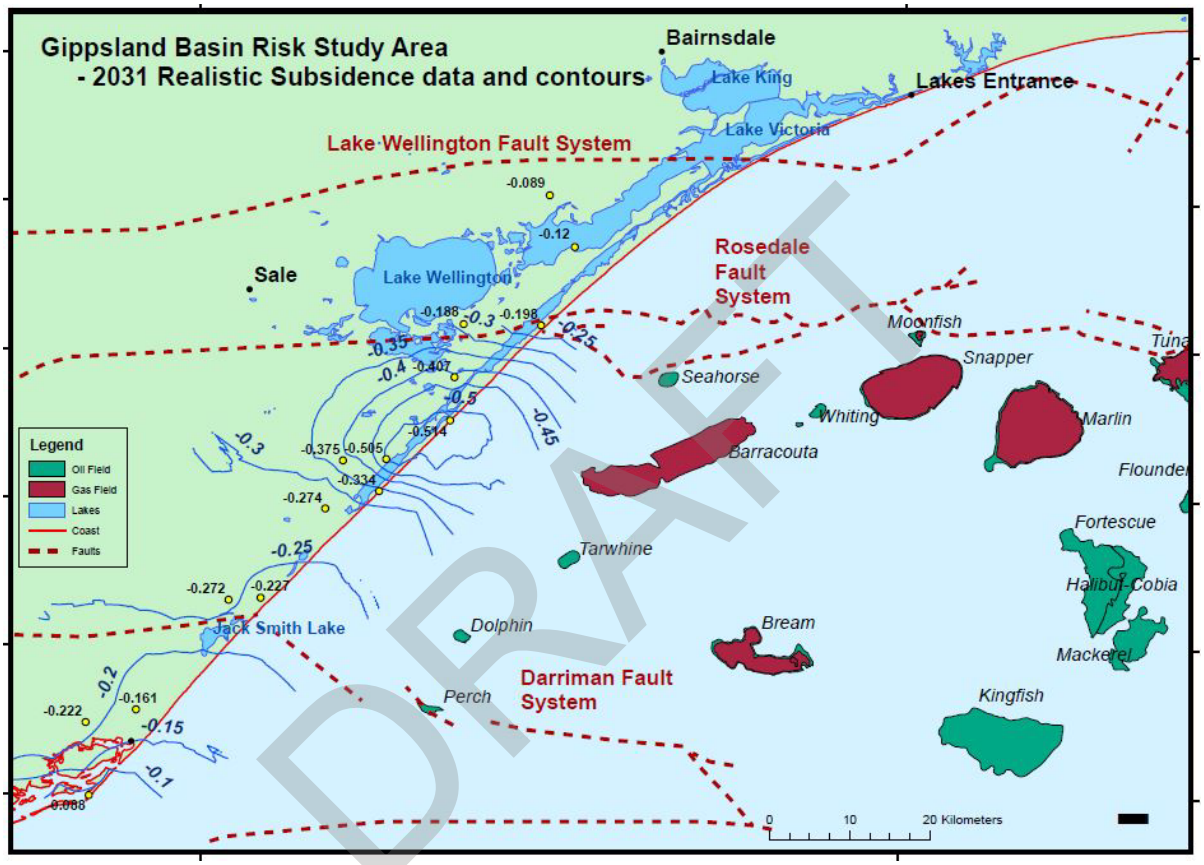

Figure 15: A map of the Gippsland Basin with contours of predicted cumulative subsidence in metres by 2031 due to Latrobe Aquifer water level decline (reproduced from Freij-Ayoub et al. (2007)).

5. Sources and Impacts of Subsidence

Subsidence associated with CSG production does not occur in isolation. Depending on the characteristics and usage of the land above a CSG field, other contributors to observed *surface movement* can include the shrinking and swelling of soils, depressurisation of shallow aquifers, and surface compaction and erosion. It is, therefore, important to be able to untangle the different components of net surface movement. This will facilitate better understanding of the distribution and significance of CSG-induced subsidence within the context of key geomechanical characteristics and processes of the shallow geological framework, more accurate forecasting of future subsidence caused by CSG production, and sound technical basis with which the industry and regulators can respond to real or perceived impacts of CSG development.

The concepts of disentangling the simultaneous processes that drive subsidence and establishing a baseline for surface movement have received some attention in the literature (Fokker et al., 2019; Masoudian et al., 2019b), but these works are far from complete, especially in the context of CSG production. In its latest Underground Water Impact Report, OGIA (2021) assessed observed and predicted CSG-induced subsidence in the context of a background trend of surface moment, rather than a reference level for surface elevation. This was intended to acknowledge the seasonal fluctuations in surface elevation that occur due to farming activities or the prevailing weather (i.e. rainfall), as well as the long-term trends that are seen in various locations throughout the Surat CMA but are not yet fully explained (Masoudian et al., 2019b).

In this chapter, a selection of natural and anthropogenic sources of subsidence (besides CSG production) and surface movement are discussed. Their relative magnitudes are contrasted with those related to CSG production and other activities such as groundwater abstraction, conventional oil and gas production, and underground mining. In closing, the potential impacts that could occur due to CSG-induced subsidence are discussed in the context of other more significant causes of subsidence.

5.1 Natural and anthropogenic sources of surface movement

Recent and ongoing studies (see, for example, Leonardi et al. (2017)) have attempted to quantify and then explain the drivers of surface movement that are unrelated to CSG production but still observed in large-scale InSAR (see Section 6.1 for a description of InSAR) surveys over the Surat CMA. Here, a summary of this work is presented, focusing on the most widespread and variable of these, which is the shrinking and swelling of shallow soils due to change in moisture (which may be natural or anthropogenic). A brief discussion of erosion and sedimentation and the influence of agricultural activity, particularly grazing, is also included.

Compaction and swelling of soils

Under changing moisture conditions, soils may exhibit compaction (i.e. shrinkage) or swelling, depending on soil parameters, resulting in upward or downward movement at the surface. Soil compression represents a reduction in pore volume. When soils are saturated this reduction in pore volume is associated with release of pore water equivalent to the change in pore volume. Soil swelling, on the other hand, is an increase in soil volume and when soil is saturated, the swelling will be a result of increased water absorption. Table 3, which has been reproduced from Leonardi et al. (2017), summarises subsidence and uplift cases related to soils and unconsolidated sediments. These have been defined as exogenic (i.e. related to surface activities and anthropogenic activity) or endogenic (i.e. related to natural earth movement) (Prokopovich, 1986).

Table 3 Summary of subsidence and uplift processes related to soil and unconsolidated sediments.

Location	Process	Endogenic or exogenic	Estimated subsidence or uplift (m)	Comments and References
Soils (up to a depth of approximately 10 m)	Swelling and shrinkage	Exogenic	Up to ± 0.16	Dependent on the clay type Tu and Vanapalli (2016) Crilly and Driscoll (2000) Briaud et al. (2003)
	Natural climate variation	Exogenic	0.06 maximum recorded	Fityus et al. (2004) McIntyre et al. (1982)
	Erosion and flooding near coastal areas	Exogenic	Approximately 0.001 to 0.015 per year	Erosion and flooding near coastal areas
	Earth tide and barometric loading	Endogenic	0.3 to 0.4 maximum	Phillips et al. (1999)
Alluvium (up to a depth of approximately 130 m) and colluvium	Earth tide and barometric loading	Endogenic	0.3 to 0.4 maximum	Phillips et al. (1999) Watson et al. (2006)
	Irrigation	Exogenic	Up to 0.04	Swelling clays in Namoi valley Ross and Jeffrey (1991)
	Groundwater head fluctuation	Exogenic	0.04 to 0.075	Seasonally variable elastic compaction Fityus et al. (2004)
	Excessive groundwater pumping	Exogenic	0.08 in four years (Narrabri)	Inelastic compaction

Data sourced from Leonardi et al. (2017)

Swelling and shrinking of clay-rich units depends mostly on mineralogical content of clays and the water retention properties of soils. Of the three main clay mineral groups, smectites have most tendencies for swelling with time, followed by illites and kaolinites (de Vallejo & Ferrer, 2011). This shrink–swell phenomenon is a natural hazard throughout the world because cycles can cause differential settlement of ground (Nowamooz, 2014). Other factors include climate variations and tree and ground cover. In Australia, 20% of the surface is covered by expansive clays (Fityus et al., 2004) and a number of studies have been undertaken to improve understanding of their behaviour. For the purpose of estimating the change in swelling and shrinking, the active depth (seasonal water suction) is typically assumed between 1.5 and 2 m (in accordance with the AS 2870 for the Newcastle area, NSW). At shallow depths, subsidence caused by changes in the water table is related to changes in soil saturation (McIntyre et al., 1982). At these soil depths, it is important to understand the soil suction (saturation) relationship with the water retention properties and the volume changes.

The extent of soil shrinkage can be irreversible if the soil tensile strength is exceeded and fissuring occurs (Pineda & Sheng, 2013). In other cases, the water table rise will result in an increase in volume of swelling clays (e.g. Jahangir et al. (2012)). Vertical swelling is related to the absorption of water which is expressed at depth. The response of ground movements, such as subsidence, is found to be dependent on accumulated rainfall and temperature variations. McIntyre et al. (1982) found via experiments that soil saturation occurs such that initially the water enters the soil via macropores and saturates the matrix, after which wetting is followed by filling of macropores. With the increase in infiltration in the experiment, the swelling increased to 60 mm. The extent of swelling and shrinking is dependent on the period in the wetting/drying cycle and therefore the soil suction, and whether the soil is in the initial state of saturation or if it has been rewetted before.

The extent of ground surface movement as a result of this process has been measured between 47 and 75 mm at a site near Newcastle, Australia (Fityus et al., 2004). Crilly and Driscoll (2000) found that the driver of movement occurred in the top 8 m of soil but was not limited to this depth. The ground movement in their study, which focused on a site in Kent, England, varied between 60 to 160 mm for 35% water saturation and 100 to 200 kPa soil suction. Briaud et al. (2003) found that at their study site in Arlington, Texas, the active zone extended to an approximate depth of 3 m and the heave on the surface was 37 mm.

Changes in hydrogeological conditions, including natural groundwater response to rainfall recharge, response to groundwater abstraction, and also seasonal irrigation and drainage, can result in cyclical fluctuations in volume in clayey material which then causes swelling or shrinking. For example, soil cracks that occur during drying periods can increase the hydraulic conductivity of soil by one to three orders of magnitude (Sadek et al., 2007; Yesiller et al., 2000). The swelling and shrinking of soils is influenced by crack development because such cracks provide high conductivity flow paths that allow deeper layers to be subjected to variations in water content (Auvray et al., 2014).

The mechanism that drives compaction of shallow soils is analogous to that in deeper aquifers and reservoirs. When groundwater is withdrawn from storage, the hydraulic head is lowered and as a result the mechanical support that was previously provided by pore water is now transferred to the skeleton (i.e. an increase in effective stress). If the loading on the aquifer skeleton is excessive (i.e. too much water is withdrawn) then the strata may be irreversibly compressed. This causes permanent compaction for highly compressible units such as silt and clay (Alley et al., 2002). In addition to pore pressure drop and compaction, another mechanism occurs during extraction of fluid. Lateral shrinkage of strata also occurs where the water table was lowered (Pineda & Sheng, 2013). Consequently, Doornhof et al. (2006) introduced side-burden as material which is not compacted during the fluid extraction but serves as support by providing an arching effect.

Given that sand exhibits a higher hydraulic conductivity than that of clay, the water moves rapidly in and out of the formation. As a comparison, clayey layers will require longer to depressurise and the drainage will occur until the excess pore pressure equals that in the sand layer. The processes that occur in both clay and sand formations are similar. However, during a reduction in hydraulic head, the orientation of clay particles in clay layers changes to that normal to perpendicular load (Kasmarek, 2004). Dewatering and change in grain orientation reduces the porosity and results in compaction. Gabrysch (1975) indicated that 90% of the compaction in clay is permanent and, therefore, the change in potentiometric head will have little effect on surface elevation. They also conclude that although the clay layers are generally inelastic, if a significant number of clay layers are present, then compounding compaction can occur resulting in surface subsidence. To generalise, within clay and silt layers with low hydraulic conductivity and high compressibility, the process will take longer and will depend on the pore pressure change and will continue until it reaches equilibrium. This time is dependent on specific storage, thickness of material and vertical hydraulic conductivity.

The inelastic nature of sediments can be observed from gradual change in water level with subsidence. Earlier studies (Helm, 1975) indicate that compaction or expansion of clay layers is proportional to the effective stress. Therefore,

for confined sediments assuming no change in overburden load, compaction, Δb, is proportional to change in head, ΔH_f (Kasmarek, 2004),

$$\Delta b = -S_s B_0 \Delta H_f, \quad (14)$$

where S_s is the skeletal component of elastic or inelastic specific storage and B_0 is the thickness of the layer. This equation assumes instantaneous equilibration of heads with no consideration for a delay in drainage (Erban et al., 2014). Ideally, this behaviour would be reversible under small strains. However, the behaviour of soil following repeated loading and unloading due to dewatering is not perfectly elastic (Galloway et al., 1998). The response of unconsolidated, higher-permeability sediments to change in head is different to that in clayey aquitards. The change in head in the former system will not change the geostatic pressure. As a result, the increase in effective stress will be equal to the decrease in fluid pressure and the compaction will be instantaneous. When the head recovers the deformation will recover, but to a minor extent (Poland, 1984).

In addition to water table fluctuation, the thickness of the vadose zone and the capillary moisture storage will have significant implications for the transfer of moisture to deeper layers. For example, organic-rich soils have high water retention capacity, which can retain water for longer time periods preventing the drying of the surface layer. In addition, the presence of vegetation plays an important role in reducing the complete drying of soils.

Sedimentation and erosion by water flow, dissolution, and weathering

Sedimentation, erosion, weathering, and dissolution are slow geological processes which can take a long period of time to occur (e.g. 1 to 2 cm per million years). During the geologically recent Cainozoic era, the overall erosion rates have increased. However, this process is slow relative to human life spans. For example, erosion or sediment accumulation rates in the Alps have been estimated at 10,000 km^3 per million years (Schumer & Jerolmack, 2009). Given that such processes are very slow, they are unlikely to be of significance relative to CSG-induced subsidence.

A review (Leonardi et al., 2017) of active tectonics found that it is detectable in sediments, the landscape, and earthquake records, in the form of uplift, escarpment, upwarping, and depressions. In addition, active tectonics can be expressed via subtle effects on sedimentation. Alluvial systems are sensitive to local/regional changes in topographic gradient, and respond with changes in the pattern, the style of surface flow, and also in the volume of sediment discharge.

The natural material loading related to river sediment deposition is much more significant (e.g. the deposition of 300 to 500 million tons of sediment each year by the Mississippi River delta (Allen, 1984)). This sediment deposition is naturally also accompanied by subsidence, mainly as a result of the rearrangement of grains and the continuous influence of water and compaction.

River deltas are sensitive to increasing risk from land subsidence and related to global sea-level rise and climate extremes. Delta sediments naturally compact over time, and to maintain the land elevation new sediment fluxes are provided from the upstream river network to the delta surface (Syvitski & Saito, 2007). Land subsidence is compounded by rising sea levels and the changing intensity and distribution of extreme events related to climate change (Knutson et al., 2010). Ingebritsen and Galloway (2014) report the rates of natural subsidence of unconsolidated sediments at approximately 0.1 to 1 cm per year.

Movement of soil and sediments as a result of barometric (un)loading

Barometric pressure and earth tides exert pressure on the ground surface and due to their cyclical nature result in loading and unloading effects. These changes in barometric pressure and earth tide fluctuations exert pressure on hydraulic heads. For example, the daily change in barometric pressure of 20 hPa results in 20 cm change in groundwater levels. The ratio of the responses of hydraulic head to the atmospheric pressure change is a measure

of aquifer barometric efficiency. Loading efficiency is the reciprocal of barometric efficiency and it can be used to estimate the formation compressibility and aquifer specific storage.

Acworth et al. (2016) developed a method that quantifies the earth tide component allowing the analysis of aquifer properties. This research built on earlier work (Gonthier, 2007; Merritt, 2004) to improve the method for quantifying and removing the impact of earth tide. The major application of this approach is in assessing worldwide problems of land subsidence or groundwater resource evaluation that both occur due to groundwater abstraction (Acworth et al., 2016). David et al. (2017) applied these techniques to estimate compressibility and storage changes in overburden rock during subsidence associated with longwall coal mining. Recent works by McMillan et al. (2019) and Rau et al. (2022) have significantly improved in-situ estimation of barometric and earth tide and application of this method to both natural and induced groundwater level variations.

Other contributions to the background trend

To investigate the existence of a background trend of net surface movement within the Surat CMA, Masoudian et al. (2019b) analysed InSAR observations (see Section 6.1 for a discussion of InSAR) over regions featuring no active CSG wells (herein referred to as non-producing regions) for the period July 2012 to November 2016. The first step in this process was to inspect the surface elevation change over the entire dataset to identify a number of regions of interest for further interrogation. This resulted in the selection of four focus areas, within which a maximum apparent subsidence of 50 mm (approximately 10 mm/year) was observed.

The spatial distribution of net surface movement and the temporal distribution of rainfall for two of these focus areas are reproduced in Figure 16. One focus area (FA1) covers greater than 450 km^2 over the Dawson River, southwest of Taroom. Land use information for FA1 indicates that it is primarily classified as grazing native vegetation, with some cropping. The other focus area (FA4) is approximately one order of magnitude smaller than the others studied in Masoudian et al. (2019b). It is located near the Yuleba State Forest, between Roma and Miles, and covers almost 27.5 km^2. The land use classification for FA4 is primarily grazing native vegetation, with some production native forests, and cropping.

Whilst all of the four focus areas exhibited apparent downward surface movement (i.e. subsidence) over the period of observation, this was most pronounced in FA1 and FA4. In FA1, the apparent subsidence was widespread, with localised maxima of approximately 50 mm (see Figure 16(a)). The average movement for the area showed a consistent downward trend, with temporal fluctuations that appear to correlate with periods of high rainfall (see Figure 16(b)). The local, temporal minima coincide with heavy rainfall events during the wet season. Following these events, it can be seen that the ground surface moves upwards (uplift), reaching the largest uplift almost immediately after the peak of rainfall. Thereafter, the ground surface returns to a downward (subsidence) trajectory during the dry season. This (and other cases discussed in Masoudian et al. (2019b)) suggests that the fluctuations observed in the mean surface displacement are due to the effect of rainfall infiltration into shallow soil layers near the surface. Further data interrogation in FA1 found that the soil composition is susceptible to consolidation and the swelling and shrinkage that can be induced by rainfall infiltration. However, this apparent correlation cannot fully explain the overall trend of downward movement of the ground surface, it can be argued that the effect of rainfall infiltration may be associated with some hysteresis so that the downward movement of the ground surface does not fully recover during the wet season. Alternatively, the background trend may be due to a longer-term period of soil and alluvia drying due to below-average rainfall.

The surface movement data in FA4 (see Figure 16(c)) showed a well-defined region of approximately 50 mm movement, which appears to align with paddocks. The absence of InSAR data in the middle of FA4 is most likely due to low coherence and poor data quality as a consequence of seasonal plant growth or erosion. Looking at the average movement for the area (see Figure 16(d)), it can be seen that it does not fluctuate with rainfall to the same

degree as FA1. This suggests that the (unattributed) cause of net surface movement associated with agricultural activity is a bigger contributor than seasonal infiltration and drying in this location.

Another interesting observation made during this study is highlighted in Figure 17, which plots the net surface movement observed in a diamond-shaped region at Savannah, south of Roma. This shows apparent subsidence of approximately 50 mm. However, interrogation of the satellite image of this area suggests that it is delineated by a fence line used for holding livestock which have (probably) contributed to compaction and or erosion. Although the magnitude of movement is similar to that observed in FA1 and FA4, the underlying cause is significantly different.

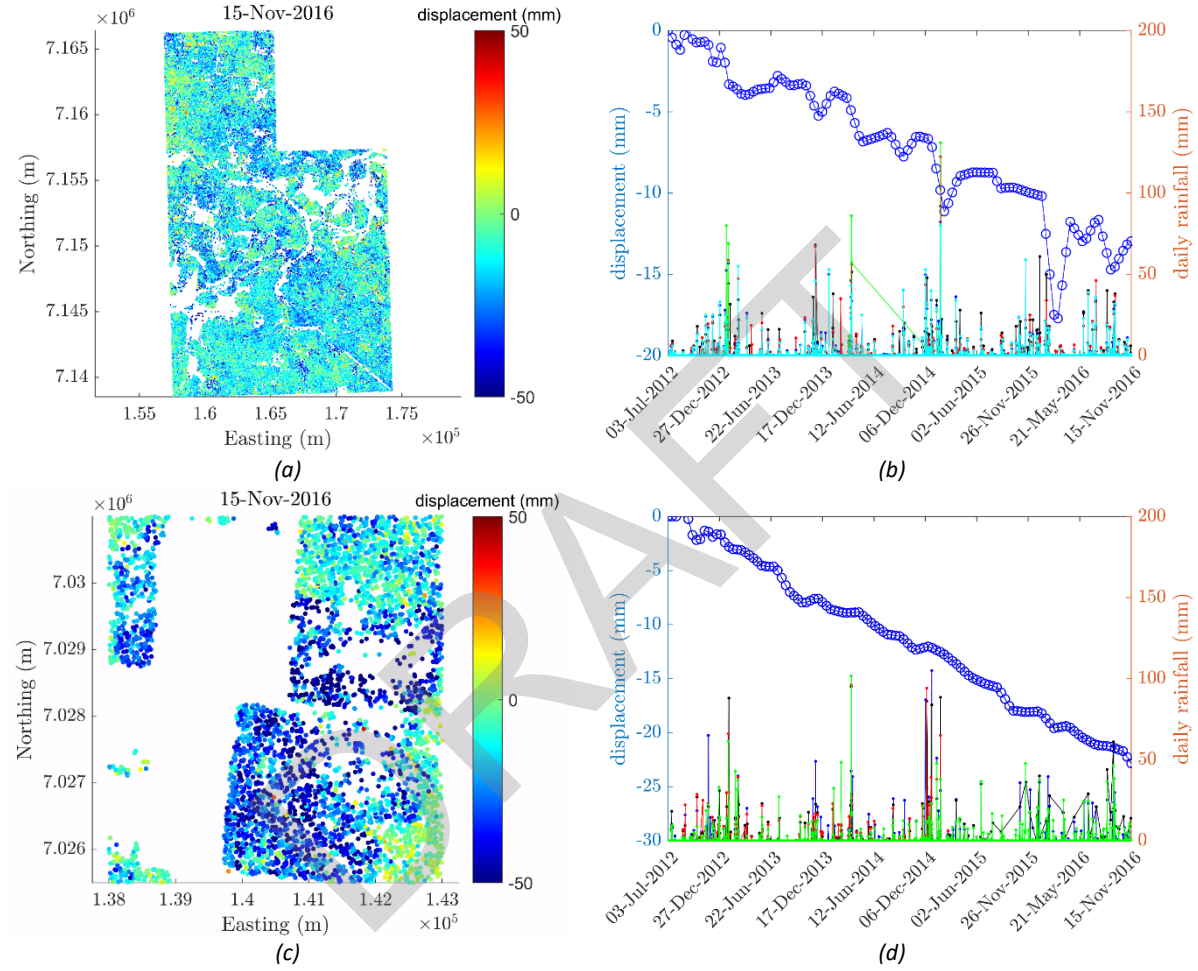

Figure 16: Observations of net surface movement and rainfall in the period July 2012 to November 2016 for two non-CSG producing regions (FA1 and FA4) in the Surat CMA. The images show (a) InSAR measurements of net surface movement in FA1, (b) the average movement of FA1 and rainfall data from four gauges, (c) InSAR measurements of net surface movement for FA4, and (d) the average movement of FA4 and rainfall data from four nearby gauges (reproduced from Masoudian et al. (2019b)).

5.2 Potential impacts of CSG-induced subsidence

Some manifestations of subsidence can be dramatic, resulting in damage to roads and buildings or exposing cities to ingress of seawater. Certainly, some of the subsidence magnitudes associated with aquifer depletion worldwide (e.g. San Joaquin Valley) are extreme. When considering the potential impacts of subsidence associated with CSG production, it is also important to consider their magnitude in the context of other natural and anthropogenic drivers, particularly those likely within Australia. Figure 18 helps with this comparison by highlighting the characteristic subsidence profile and typical magnitudes associated with CSG production, bord and pillar coal mining, longwall coal mining, and multi-seam coal mining. In terms of absolute magnitude (and also gradient), it is

clear that underground coal mining is the most significant source of historical and potential future subsidence. By way of further comparison, local CSG-induced subsidence data are similar to those observed from CSG production in the Powder River Basin and of the same order of magnitude as surface elevation fluctuations caused by seasonal variation of clayey soils. The magnitude of subsidence expected from CSG production is not large and may be similar to other natural phenomena that could be expected to occur in the same area (e.g. localised erosion, the shrinking and swelling of soils and alluvia).

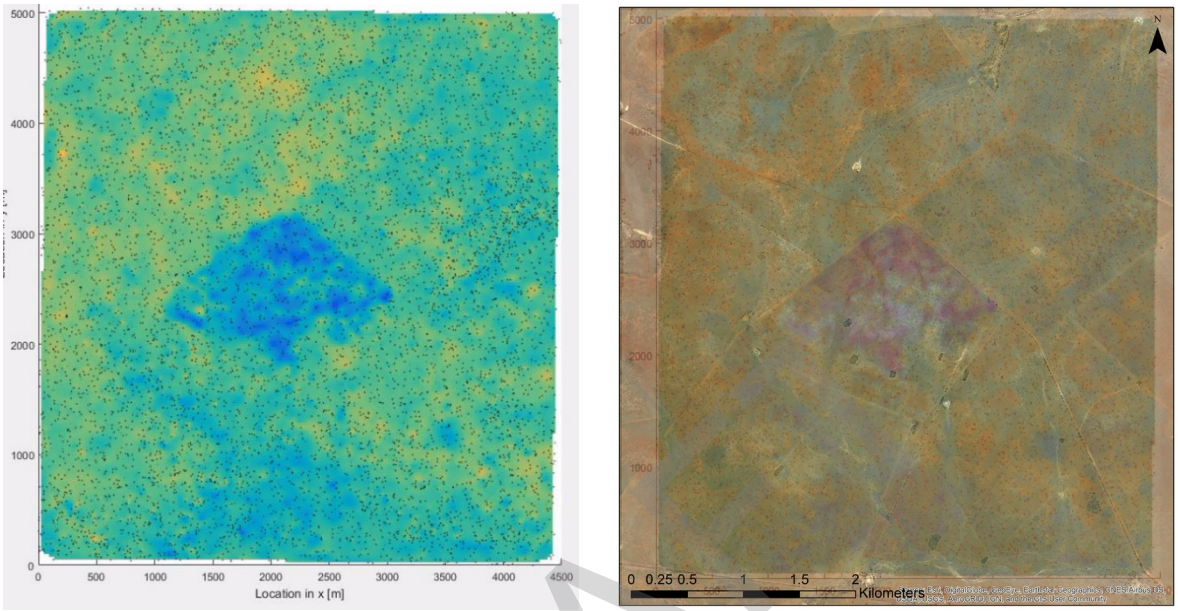

(a) *(b)*

Figure 17: Observed net surface movement in an area approximately 4.5 × 5 km at Savannah, south of Roma, showing (a) surface movement away from the satellite (i.e. downward) in the period July 2012 to November 2016 ,and (b) a satellite image of the same location highlighting a fenced paddock (reproduced from Masoudian et al. (2019b)).

To assist with the management of potential impacts of CSG-induced subsidence, the GasFields Commission Queensland (GFCQ) commissioned two interrelated bodies of work in 2022. The first is a review of the regulatory framework related to CSG-induced subsidence while the second is an investigation of the potential for and consequences of CSG-induced subsidence at the scale of a co-located property, such as a farm. The review (GasFields Commission Queensland, 2022) found that, although landholders are protected by existing compensation liability for CSG-induced subsidence impacts, there existed scope for enhancement and clarification of the regulatory framework. This resulted in the tabling of eight recommendations to the State Government of Queensland, which were designed to "enhance existing protections and provide clarity to landholders and the gas industry" (GasFields Commission Queensland, 2022)

Research on the potential for CSG-induced subsidence impacts and consequences at the farm scale is being conducted by GFCQ in partnership with the Office of Groundwater Impact Assessment (OGIA). At the time of preparing this document (2023), this work was ongoing with reporting expected in 2023.

Impacts on built infrastructure

A review of the literature reveals no peer-reviewed research or verified accounts of adverse impacts caused by CSG-induced subsidence. Best et al. (2014), therefore, summarised a range of potential impacts based on the experience associated with coal mining and groundwater abstraction for irrigation or mining. In the intervening years, it has become apparent that many of the listed impacts are not relevant to CSG production in Australia because of increased understanding of the maximum subsidence magnitudes to be expected. In addition, CSG-induced subsidence will not result in the surface curvature that can be seen at the edge of a subsidence trough above a

longwall coal mine. Therefore, the likelihood of impacts on built infrastructure due to differential settlement, such as large gradient change or surface fissures, is extremely low.

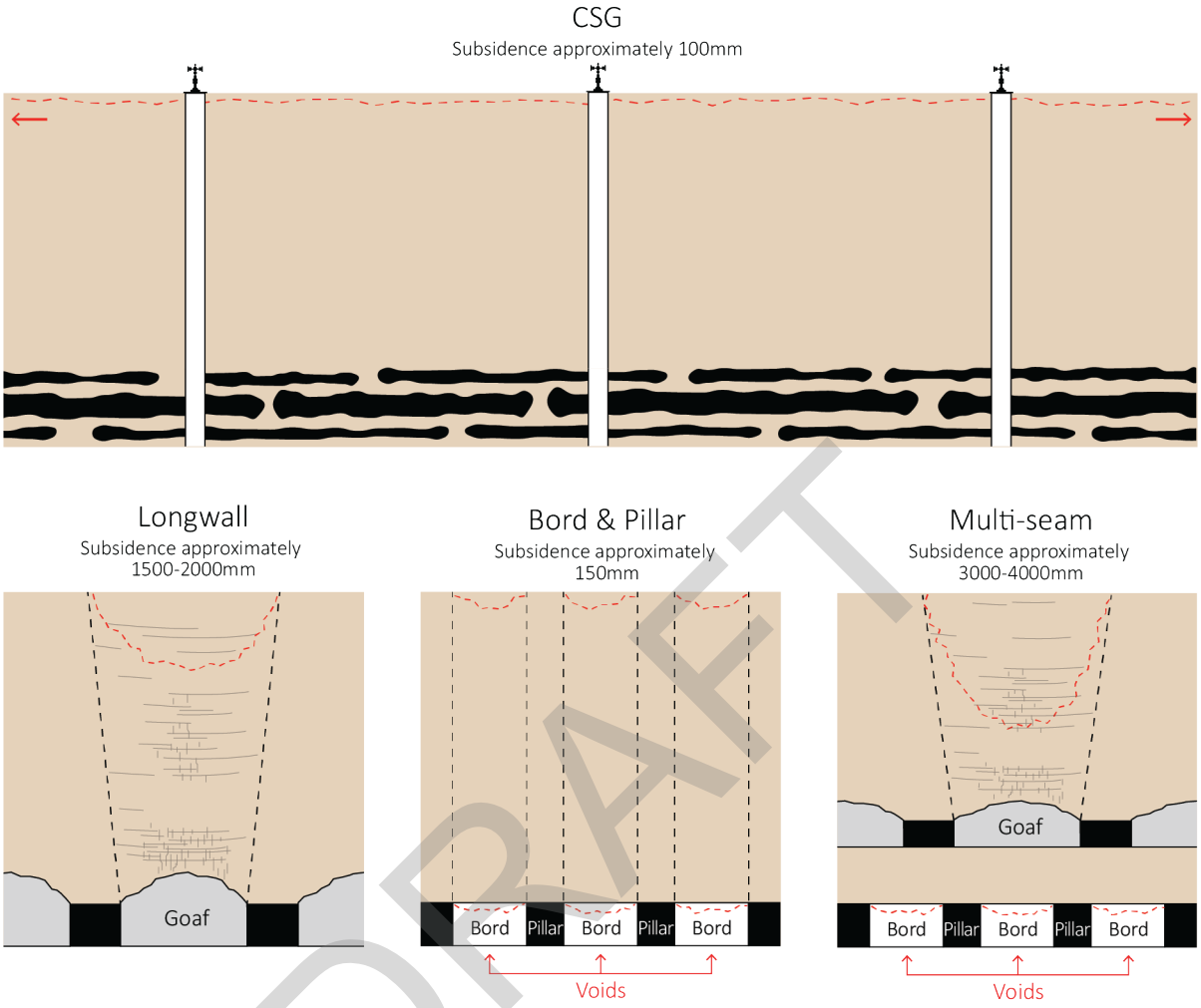

Figure 18: A comparison of the subsidence profile and magnitude associated with CSG production, longwall coal mining, bord and pillar coal mining, and multi-seam longwall mining in Australia.

Some Queensland CSG production is co-located with intensive, irrigated cropping on vertosols that contain a high percentage of expansive clay minerals. Depending on the site classification of clay type and reactivity (Standards Australia, 2011), the range of vertical soil movement (i.e. shrinking and swelling) can be up to 75 mm. Indeed, some Class E sites in South East Queensland have been known to move up to and in excess of 150 mm (Queensland Building and Construction Commission, 2022). The variation in soil moisture underneath and adjacent to building foundations can, consequently, induce differential movement which damages structures, as shown in Figure 19. Australian construction standards (Standards Australia, 2011) prescribe the maximum design differential footing deflection for different types of construction. The maximum differential deflection gradient ranges from 1:300 for clad frame to 1:2,000 for full masonry construction, while the maximum differential deflection for these categories are 40 mm and 10 mm, respectively. These design gradients are several orders of magnitude greater than that expected and observed from CSG-induced subsidence (see discussion related to water resources and infrastructure below). In this context, the risk of additional impact to structures from CSG-induced subsidence is deemed low.

Induced curvature in buried pipelines can create tensile and compressive stresses due to bending. Bracegirdle et al. (1996) presented empirical data outlining the gradient limits beyond which damage would occur. For relatively rigid

pipes, more than 200 mm in diameter, the induced slope limitation was listed as less than 1:140. For relatively flexible pipes, less than 200 mm in diameter, the induced slope limitation ranged between 1:140 and 1:40. Exceeding the more conservative of these limits (i.e. 1:140) would require 100 mm of subsidence to develop over a distance of 14 m, which is not expected to occur due to CSG production and thus not a significant risk.

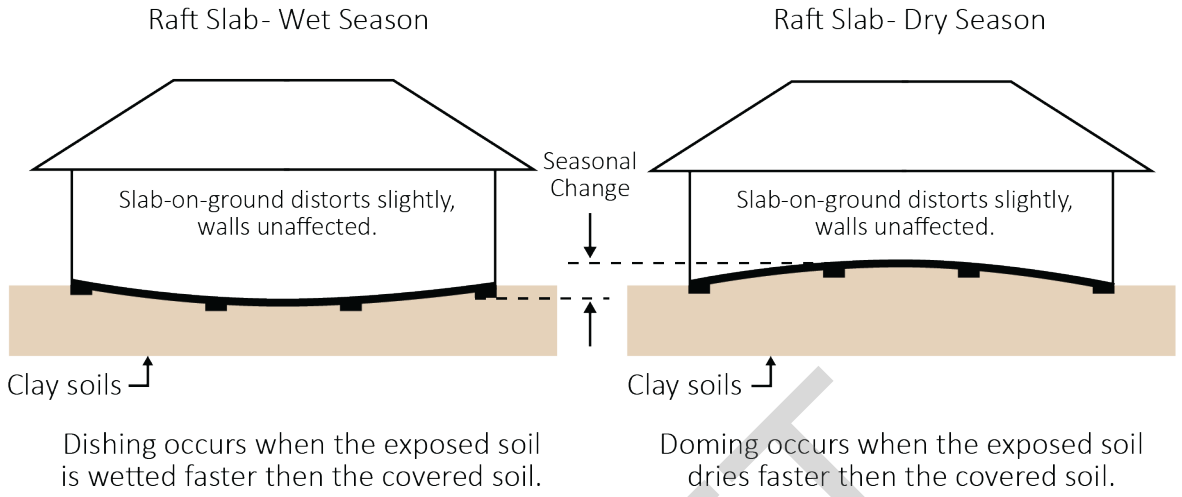

Figure 19: The mechanisms of foundation deformation due to gradients of soil moisture surrounding a structure (reproduced from Queensland Building and Construction Commission (2022)).

Subsidence has the potential to damage the casing of water bores and gas wells. Ross & Jeffrey (1991) reported on the increased failure rate of production bores in the Namoi Valley, which was attributed to the subsidence caused by groundwater removal. The greatest proportion of CSG-induced subsidence stems from compaction in the coals (Masoudian et al., 2019a). Many groundwater bores are completed in formations above the coals, which reduces the likelihood of damage to these bores. The potential for damage (e.g. casing shear and distortion, screen collapse) to deeper bores and gas wells remains.

Vertical settlement, horizontal strain and compaction, tilt and ground curvature can cause damage to roads, which may manifest as compression humps, tension cracks, and a distortion of the road surface (Best et al., 2014). The potential for this to be caused by CSG-induced subsidence is dependent on the change in surface gradient. The limits on allowable change in grade of road pavements are typically 0.3% in 40 years for concrete pavements and 0.5% in 20 years for flexible pavements (Wong & Summerell, 2012), which are significantly greater than the predictions and measurements published by OGIA (2021). Therefore, the risk of impacts to roads associated with CSG production are considered small, and the same conclusion can be drawn for rail infrastructure. It should be noted that the ARC Training Centre for Advanced Technologies in Rail Track Infrastructure at the University of Wollongong, in collaboration with The University of Queensland, commenced research in 2022 investigating the effect of moisture and cyclic loading on the deformation of railway embankments and expansive soil subgrades. In 2021, this project established long-term field monitoring at the West Moreton System in Chinchilla for the collection of data on local weather conditions, surface settlement, and soil moisture and suction profiles with depth at two railway transects.

Impacts on water resources and infrastructure

Subsidence due to groundwater withdrawal can result in impacts to hydrological systems such as aquifers, lakes, streams, springs, and other surface water resources. This can manifest as a change in the drainage pattern of streams and channels, the ponding of water within subsidence troughs (if they form), the deepening or widening of pools in streams, or alteration of riparian ecosystems and geomorphological stability. Subsidence can also increase the impact of, or exposure to, riverine flooding or delayed drainage. Coastal impacts such as storm surge or the impact of tides are no risk to CSG-producing regions in Australia.

Where CSG operations are co-located with intensive agriculture, one potential impact relates to changes in terraformed surface gradients which are used to control the flood irrigation of crops such as cotton and grain (see Figure 20). This approach to broadacre irrigation requires paddocks to have a planar, but furrowed, surface of constant gradient on the order of 0.1% (i.e. 1:1,000, or 1 m fall per 1,000 m) but no less than 0.06%. Paddock slopes of less than 0.06% are considered too flat to drain effectively and will become waterlogged during periods of above-average rainfall (Purcell, 2012). Flood irrigation is most effective in paddocks with uniform gradient as this helps maintain even wetting of the soil profile, and so farmers will periodically deploy techniques such as *laser levelling* to remediate gradient changes that occur over time (e.g. the formation of *gilgai*, or small water holes).

At the time of writing (2023), no scientifically verified accounts or technical reports of significant changes to surface gradient as a consequence of CSG-induced subsidence had been documented. However, it is instructive to consider the potential for this to occur based on the current understanding of likely subsidence magnitudes, noting that the thickness of compressible formations (e.g. coal seams) changes over large distances and the depressurisation of those formations is diffusive. Put another way, the two key drivers of CSG-induced subsidence vary in space over distances on the order of hundreds of metres, and thus the same could be expected of the associated compaction. Recent predictions and observations of CSG-induced subsidence within the Surat CMA (OGIA, 2021) are approximately 100 to 150 mm. If this magnitude of movement were to develop over a distance of 1 km, it would result in a gradient change of 0.01 to 0.015%, which could result in marginal to poor drainage of a paddock that was initially close to the threshold of 0.06%. However, according to OGIA (2021) the change in ground slope from CSG-induced subsidence in most areas is predicted to be less than 0.001% (i.e. 10 mm over 1 km), with some areas up to 0.004% (i.e. 40 mm over 1 km). During parametric uncertainty quantification, it was found that in a localised area north of Cecil Plains there exists 80% probability of the maximum change in slope exceeding 0.005% (OGIA, 2021), which is still significantly less than that required to alter drainage patterns.

Figure 20: Flood irrigation of a furrowed cotton paddock near St George, in the southwest corner of the Surat CMA (modified from commons.wikimedia.org/wiki/File:StGeorgeCottonIrrig.jpg).

As a part of the Water Monitoring and Management Plan for the Surat Gas Project, Arrow Energy commenced the use of airborne LiDAR survey to measure baseline gradient changes within their tenements (Arrow Energy, 2022). Amongst other objectives, the intent of this work was to describe the representative slope on dryland or irrigated cultivation within the company's tenure, the accuracy with which the surface and slope on cultivated land can be measured, and the variation in ground surface elevation that can be observed with soil moisture changes. According to the analysis of slopes, most of the cropping paddocks of the Darling Downs and within Arrow's tenement have slopes ranging from 0.12% to 0.5%, which are two orders of magnitude greater than any changes predicted by OGIA (2021). Using strip cropping as an indicator of swelling and shrinking, it was found that up to 200 mm surface elevation difference can result due to soil moisture changes. As this longitudinal study continues, more quantitative

information on natural and anthropogenic sources of surface movement in locations of intensive agriculture will become available.

No documented cases of adverse impacts to agricultural dams caused by CSG-induced subsidence, or other sources of surface movement, could be found in the academic literature or Queensland Land Court records. Given that the magnitude of elevation and slope change caused by CSG-induced subsidence are small, the future risk to agricultural dams is considered to be low.

6. Subsidence Monitoring Techniques

The large spatial extent of CSG production regions make accurate monitoring of any widespread surface movement challenging. While in-situ monitoring techniques can produce high accuracy measurements, the spatial extent is limited to the immediate installation location. This makes the widespread use of these techniques inadequate and cost-prohibitive for large-scale monitoring. They can, however, be used to complement large-scale monitoring methods. Outlined in this chapter is a summary of the main techniques that can be used to monitor surface movement in regions of CSG production.

6.1 Interferometric Synthetic Aperture Radar (InSAR)

A well-established surface movement monitoring technique is interferometric synthetic aperture radar (InSAR). It has been successfully used for over 25 years to detect and monitor surface movement for a range of applications, including sub-surface infrastructure development (e.g. transport tunnels), underground mining activities (e.g. longwall mining), groundwater extraction, aquifer recharge and discharge, magma chamber inflation and deflation, and the interseismic, coseismic and postseismic stages of the seismic cycle (Ferretti, 2014; Hanssen, 2001; Moreira et al., 2013). While InSAR provides large spatial coverage, it has lower accuracy compared to in-situ measurements.

InSAR uses two synthetic aperture radar (SAR) images taken at different times over the same area to identify any topographic height changes. Each image observes the same ground point from slightly different geometry, which enables relative differences in distances (i.e. phase) between the images to be obtained via trigonometry. If the Earth's surface has moved between image acquisitions, a *phase shift* occurs, as shown schematically in Figure 21. This shift is represented in an interferogram as a series of colour cycles or interference fringes, where one fringe represents a phase change of 2π radians. The colour order determines if there has been a shift towards or away from the SAR sensor. The interferometric results provide estimates of topographic heights and surface movement, with height measurements comparable to optical remote sensing methods.

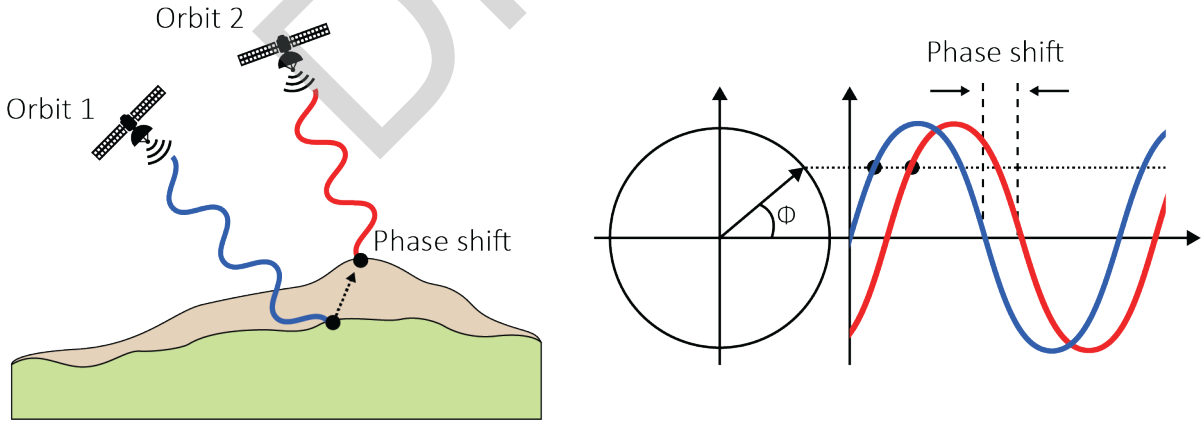

Figure 21: Schematic representation of the phase shift between SAR images where the Earth's surface has moved between image acquisitions.

Differential InSAR (D-InSAR) takes InSAR a step further, by isolating surface movement signals through the removal of the topographic signal component (Hanssen, 2001). For monitoring slow (i.e. over a number of years) surface movement changes, such as those that may be associated with CSG production, a time-series dataset using multiple interferograms is required.

Synthetic aperture radar systems

SAR systems transmit pulses of microwave energy to the Earth's surface and record the amount backscattered. The pulses' two-way travel time is then used to resolve a surface object's range and physical characteristics. The ability for microwave energy to penetrate rain (unless wavelength is less than 4 cm) and clouds provides SAR systems with an all-weather, day and night capability (Hanssen, 2001; Jensen, 2000; Ulaby & Long, 2014).

SAR systems are side-looking, and most SAR satellite systems are right-looking systems, where they transmit energy pulses from the system's right side relative to the flight direction (line of sight; LOS). All systems have the same geometric components (see Figure 22(a)), however the parameters for components such as altitude, incidence angle and swath width can vary between systems. The resulting SAR imagery appears with slant range geometry. which looks different to the imaged ground surface. However, the imagery can be corrected to ground range geometry.

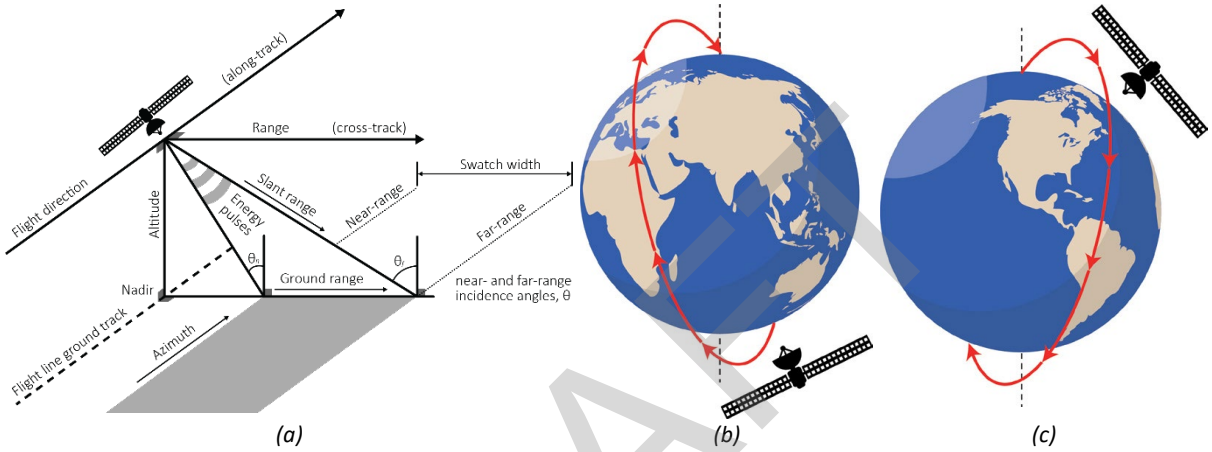

Figure 22: Aspects of a right-looking SAR satellite's trajectory, showing (a) the azimuth direction (parallel to the flight direction), emitted energy pulses perpendicular to the azimuth (range direction), the nadir (the point on the ground directly below the satellite's position), the incidence angle (angle between the energy pulse and the nadir line) including near- and far-range angles as these constrain the swath width (modified from Jensen (2000)). Also included is the general polar sun-synchronous orbit orientation for SAR systems, showing (b) south to north (ascending) tracks and (c) north to south (descending) tracks.

Each pixel in a single look complex (SLC) SAR image contains a complex number, with real in-phase (I) and imaginary quadrature-phase (Q) components. These components may also be described as amplitude and phase information. The amplitude details the ground surface's backscatter properties, and the phase represents the two-way travel distance. Phase differences between two SLC SAR images are exploited in the D-InSAR technique.

Due to the oblique or slant range geometry, geometric distortions are inherent in SAR imagery and need to be considered when working with such imagery. Topographic distortions occur in nearly all imagery, unless the ground surface is truly flat. The distortions include foreshortening, layover, shadowing and speckle (Jensen, 2000; Ulaby & Long, 2014; Woodhouse, 2006).

SAR satellite systems use a polar sun-synchronous orbit which allows the same ground spot to be revisited at the same local time, thus enabling the same region to be imaged through time along a pre-defined pass or track. As the systems orbit, they can image the same region in ascending (south to north) and descending (north to south) tracks (Figure 22(b,c)). Imagery acquired along each track can then be sliced into products or frames for further processing.

Coherence

For interferometry to be effective, the phase signals need to be coherent. This means that while the amplitude and phase components differ between two SAR images, the waves for each image have identical frequency signatures (see Section 3.4 of Ferretti (2014) for a detailed description). Coherence loss, or decorrelation, can be caused by

either geometric or temporal factors. Geometric decorrelation occurs when the perpendicular baseline between images is too large, there are very steep topographic slopes, and or the surface deformation gradient is too great for surface changes to be detectable. Temporal decorrelation results from changes in surface properties with time, such as weathering and vegetation changes (Ferretti, 2014; Hanssen, 2001; Woodhouse, 2006). The effects of decorrelation can be reduced through selection of interferometric image pairs with small perpendicular and temporal baselines. Coherence information can also be used to identify surface changes, such as soil moisture and the extent and complexity of ruptured fault traces.

D-InSAR time-series processing workflow

To create a D-InSAR time-series dataset, there must be regular, repeat SAR imagery acquisitions over the study area. It is important to note that not all SAR imagery is suitable for interferometry. Some SAR satellite systems automatically take repeat acquisitions (e.g. ALOS1/2, Sentinel-1), while other satellite systems need to be tasked with taking imagery over specific areas (e.g. RADARSAT-1/2, TerraSAR-X). For the Surat CMA, there is full or partial coverage of suitable SAR imagery available since 2007.

Interferogram generation

A range of software packages are available for the generation of differential interferograms (e.g. SNAP, GAMMA, GMTSAR, ICSE). While each program has its own processing workflow, they all incorporate the necessary steps required to produce interferograms. Each initial interferogram contains different signal components that can be represented as (Pepe & Calò, 2017),

$$\Delta\emptyset_{int} = \Delta\emptyset_{def} + \Delta\emptyset_{orb} + \Delta\emptyset_{topo} + \Delta\emptyset_{atm} + \Delta\emptyset_{scat} + \Delta\emptyset_{noise} \quad (15)$$

To isolate the deformation signal, $\Delta\emptyset_{def}$, the initial interferogram (Figure 23(a)) is refined by estimating and removing other phase signal contributions. The expected phase for a *curved earth*, the orbit geometry, $\Delta\emptyset_{orb}$, is calculated (Figure 23(b)) and removed to *flatten* the interferogram. A digital elevation model (DEM) is used to calculate the expected phase signal from topography, $\Delta\emptyset_{topo}$, (Figure 23(c)) and is removed from the flattened interferogram. The flattened interferogram is then filtered to further reduce any residual noise, $\Delta\emptyset_{noise}$, and scattering, $\Delta\emptyset_{scat}$, effects. The resulting filtered interferogram should contain the isolated deformation signal and potentially atmospheric signals if the deformation signal is small. Atmospheric affects, $\Delta\emptyset_{atm}$, are not mitigated during interferogram generation, but are considered during time-series generation.

The filtered interferogram is *wrapped* and displays deformation signals as a series of fringes or 2π cycles (Figure 23(d)). To obtain the continuous phase signal, the fringes can be *unwrapped* to show the net relative surface movement between the two SAR image acquisitions in radians (Figure 23(e)). The final step is to geocode the interferogram by converting from radar to geographic coordinates. There is an option to convert the radian values to linear displacements at this stage as well.

Time-series generation

In order to detect slow movements, such as interseismic deformation or groundwater extraction, a stack of interferograms (i.e. more than 20) covering a long time period is required to generate a time-series of cumulative surface movement. Time series techniques can be based on their use of persistent scatterers (PS), distributed scatterers (DS) or a combination of both (Xue et al., 2020). As the name suggests, persistent scatterer interferometry (PSI) relies on PS, while small baseline subset (SBAS) uses DS. Regardless of the time-series technique used, phase signals from atmospheric affects need to be considered, as these can mask signals related to slow surface movement. This is achieved by estimating atmospheric signals through either spatio-temporal filtering or calculating signals from external weather model data, for example PyAPS (Jolivet et al., 2011). A more detailed overview of time-series techniques can be found in the literature (Crosetto et al., 2016; Osmanoğlu et al., 2016; Xue et al., 2020).

SBAS was developed by Berardino et al. (2002) and utilises DS targets in interferograms separated by small baselines to minimise spatial decorrelation. DSs tend to be found in rural and mountainous terrain and are characterised by having several small and random scatterers that can be used to create a stable scatterer. This technique requires multi-looking to improve signal responses and therefore reduces image resolution (Osmanoğlu et al., 2016; Xue et al., 2020).

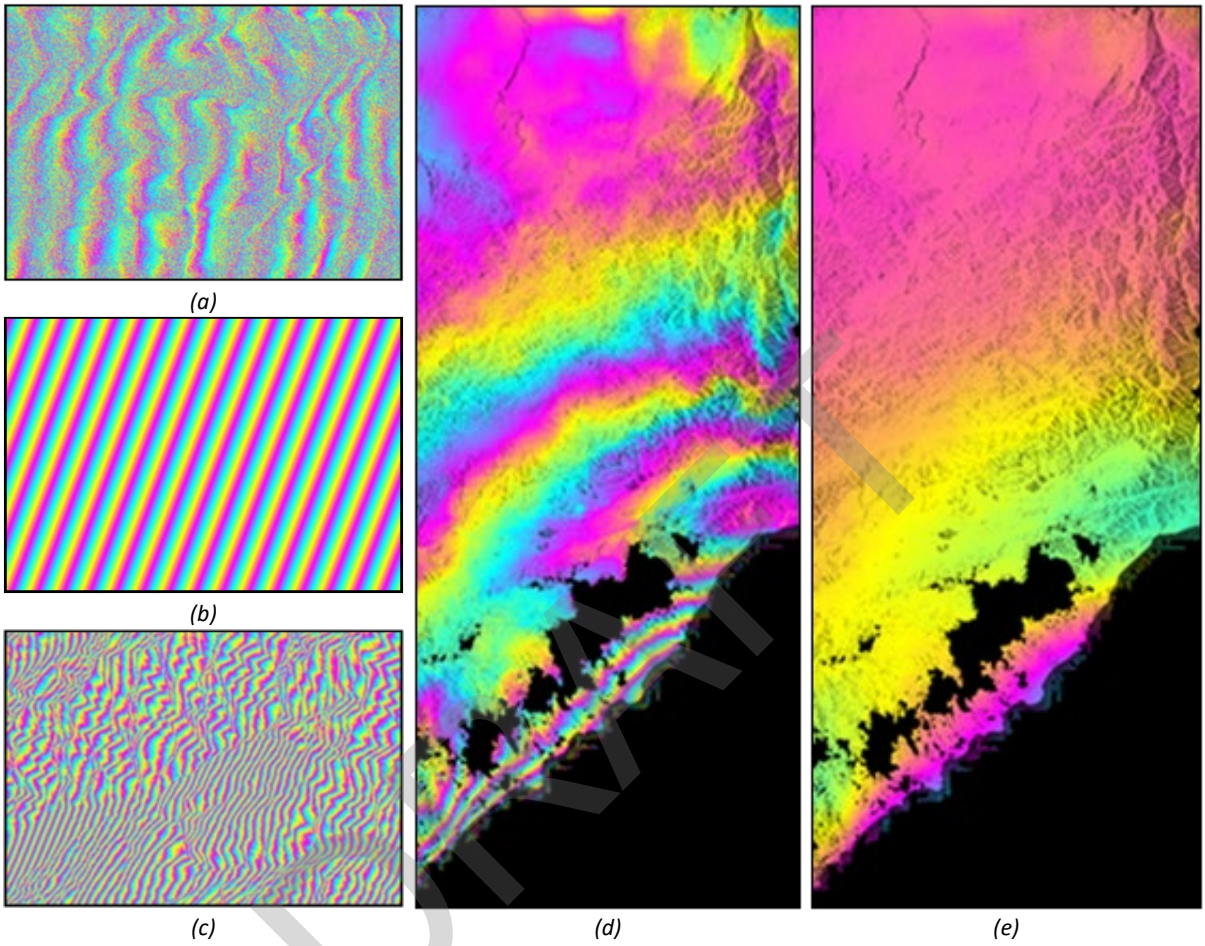

Figure 23: Steps in the D-InSAR processing workflow, showing (a) the initial interferogram, (b) orbital signal correction, (c) topographic signal correction, (d) wrapped differential interferogram, and (e) unwrapped differential interferogram (reproduced from Lawrie (2012)).

PSI was first introduced by Ferretti et al. (2001) with the development of permanent scatterer SAR interferometry (PSInSAR®). PSI uses PS targets which have a strong, stable response over long time periods. PSs are commonly found in urban areas, where buildings and other infrastructure provide ideal target responses. In contrast, they are often not present in rural and mountainous terrain because of the changing nature of the landscape. These scatterers also have dimensions smaller than the image resolution cell, which makes them unaffected by baseline decorrelation when compared to SBAS (Osmanoğlu et al., 2016; Xue et al., 2020). To overcome the limitations of PSI in non-urban areas, an advanced PSI technique, SqueeSAR®, was developed to integrate PSInSAR® into the SBAS technique (Ferretti et al., 2011). Other techniques that use PSI include interferometric point target analysis (IPTA) (Werner et al., 2003) and the Stanford method for persistent scatterers (StaMPS) (Hooper et al., 2004).

The time-series results represent the relative surface movement measurements in the line of sight (LOS). To obtain absolute surface movement measurements, the use of in-situ monitoring measurements is required in combination with, for example, corner reflectors. The geometry, orientation and size of these reflectors is linked to the microwave wavelength properties used by the SAR sensor. If they match, the reflectors will appear as a

distinct pattern in the SAR imagery. This enables the reflector's precise ground location to be tied to a pixel location in the imagery and the rate of change of absolute elevation calculated (Garthwaite et al., 2015).

Resolving three-dimensional movement

D-InSAR measurements are one dimensional along the LOS, so measured movement is either towards or away from the satellite. To resolve movement in three dimensions (i.e. north, east, and up), different viewing geometries are required. One limitation is that D-InSAR derived from SAR satellite systems is insensitive to north-south movements. This is due to the near-polar orbits and small variation in incidence angles in the north-south direction. By using SAR imagery from ascending and descending tracks (see Figure 22(b,c)), different viewing geometries are available, making it possible to resolve both horizontal (east-west) and vertical (up-down) movements (Hu et al., 2014; Ozawa & Ueda, 2011; Wright et al., 2004).

Some D-InSAR processing workflows mathematically convert LOS measurements to vertical while disregarding the horizontal component. This often occurs when only one viewing geometry is available (i.e. ascending or descending). While this approach makes it easier to explain movement results to end users, it is likely to lead to errors. Pure vertical movement is unlikely to occur across a whole study area and there will be some horizontal component present, for example in a subsidence bowl. If only one viewing geometry is available, it is preferable to leave the results in LOS and not approximate the vertical component of movement.

Limitations of InSAR techniques

As previously discussed, the total interferometric phase that is calculated from SAR data is the sum of components due to flat-earth differences in range distance, topography changes, ground movement, atmospheric effects, and noise. Atmospheric phase effects are a function of water vapour, air temperature, and pressure along the observation path, while water bodies and vegetation create dispersion in the reflected SAR signal (Tomás et al., 2014). Consequently, an important issue related to InSAR is the precision, and associated uncertainty, of the measurements it provides. Within this context, precision is defined as a function of the dispersion of the displacement measurements around an expected value, and is a function of a number of parameters which are not discussed here.

The maximum surface movement detectable by InSAR is governed by the wavelength, λ, of the radar. The maximum difference in phase for two neighbouring pixels can be 2π. This corresponds to one fringe which is equal to $\lambda/2$ (Mastro et al., 2020; Zhou et al., 2009). In their study of InSAR applications in Spain, Tomás et al. (2014) found that typical precisions for displacement rate and total displacement were ±1 mm/yr and ±5 mm, respectively, which is broadly consistent with other estimates found in the literature. In Finnegan et al. (2008), the uncertainty of relative displacement measurements was estimated to be approximately 5.4 mm, based on a comparison of the RADARSAT-1 InSAR data with GPS measurements. This is similar to the uncertainty of 5.6 mm found in the Los Angeles, USA, area by Casu et al. (2006), who also noted that this uncertainty can increase with distance from a reference pixel (e.g. a high-quality estimate from a reflector location) at a rate of approximately 0.05 mm/km. Finally, Reeves et al. (2014) explored the use of InSAR data, which is both spatially and temporally dense, to infill spatial information on the hydraulic head in the confined aquifer system in the San Luis Valley. In this context, the uncertainty of the InSAR observations was estimated to be approximately 10 mm.

The most significant limitation on the utility of D-InSAR is temporal and geometric decorrelation. Depending on the satellite and wavelength used, decorrelation may not be a major issue. Recent satellites, such as Sentinel-1, have regular revisit times and small perpendicular baselines, so decorrelation is more likely due to major surface changes between acquisitions. Longer wavelengths (L-band) are more tolerant of larger temporal baselines, compared to shorter ones (e.g. C-band). Topographic characteristics can impact geometric decorrelation through the presence of geometric distortions (e.g. layover, foreshortening), but different viewing geometries can reduce the impact of these distortions. Vegetation density and growth can also affect geometric decorrelation, and the use of longer wavelengths in affected regions can mitigate the impact. This is particularly relevant over areas of intensive, irrigated cropping.

There are other limitations or considerations that should be understood when using D-InSAR. The insensitivity to north-south movement from satellite derived SAR imagery can limit some study areas, such as faults oriented in the same direction. This can be overcome by using airborne SAR systems, as the flight path can be customised. Understanding that the relative surface movement in the LOS is being recorded is important and that D-InSAR cannot be used for real-time monitoring as the revisit time is fixed for satellites.

6.2 Differential Global Navigation Satellite Systems (DGNNS)

Precise location information for a ground point can be derived from global navigation satellite systems (GNSS). GNSS is the generic term used for satellite positioning systems which consist of satellite constellations that transmit positioning and timing data to ground receivers. There are several constellations currently deployed, including Galileo (European Union), GLONASS (Russia), BeiDou (China), and GPS (United States). Data from a minimum of four satellites are required to obtain precise three-dimensional locations, however signals can suffer from errors or delays during transmission to the Earth's surface. These errors can be mitigated via differential GNSS (DGNSS), by using data from one or more GNSS receiver stations whose precise locations are known (Hofmann-Wellenhof et al., 2008; Kaplan, 2017).

DGNSS has the ability to measure locations with centimetre precision and be used to identify changes in location through time. In a partnership between Australia and New Zealand, the Southern Positioning Augmentation Network (SouthPAN) is working towards improving positioning accuracy from 5 to 10 m down to 3 to 5 cm where mobile internet exists, and to 10 cm elsewhere. This will particularly benefit regional and remote regions, with improved access to precise positioning services (Geoscience Australia, 2022a).

Data can be collected by campaign measurements or from continuously operating reference stations (CORS). Campaign data collection requires temporary installation of a GNSS receiver for a specified period of time. To obtain a time-series of any 3D location movement, repeat campaigns are required. There are 25 CORS currently operating in the Surat CMA (Geoscience Australia, 2022b). However, the spacing of these sites is likely to be too large to detect local or regional scale surface movement (Garthwaite et al., 2015).

In 2014, a regional network of 65 permanent survey marks and 40 co-located corner reflectors was installed across the northern Surat Basin. The aim of this network was to use InSAR and GNSS observations to understand how resource extraction impacts the ground surface, with annual campaign GNSS surveys proposed (Garthwaite et al., 2015). To date, campaigns have been conducted in 2015, 2016 and 2019. In 2020, a report on the status of the 40 corner reflectors positions was produced to refine the locations and associated uncertainties for satellite calibration and validation activities (Fuhrmann et al., 2020).

6.3 Light detection and ranging (LiDAR)

Light detection and ranging (LiDAR) is a remote sensing technique that is used for a range of applications, including atmospheric studies, surface characteristics and heights, infrastructure monitoring, and navigation. LiDAR systems transmit electromagnetic energy in the optical and infrared ranges to detect objects, calculate distances between objects and the sensor, and determine physical properties of phenomena. The output produced is a highly accurate point cloud with 3D geometric information, with vertical accuracy less than 10 cm (Benedek et al., 2021; Diaz et al., 2017; McManamon, 2019).

LiDAR systems are mainly airborne mounted, with unmanned aerial vehicles (UAV) or fixed-wing aircraft used for data acquisition. These systems rely on a local GNSS data network to tie observations to ground control points (McManamon, 2019). For monitoring gradual changes in ground movement, repeat acquisitions are required at regular intervals. While LiDAR is an active remote sensing system, like SAR, its use of shorter wavelengths may cause dependencies on day/night operations and weather conditions (Diaz et al., 2017; McManamon, 2019).

In terms of ground surface elevation, the airborne LiDAR surveys commissioned by Arrow Energy are precise to 5 cm (Arrow Energy, 2022). However, the relative accuracy between points in any single observation is much better than this. In practice this means that, although LiDAR survey is not well suited to monitoring changes in absolute surface elevation, it performs very well for monitoring changes in gradient.

6.4 Application of InSAR to the monitoring of CSG fields

The application of InSAR to the monitoring of subsidence above CSG fields has been documented in a limited number of cases. Grigg and Katzenstein (2013) reported on the use of InSAR to measure subsidence above CSG operations in the Powder River Basin (see Section 4.2 for further discussion). More recently, Du et al. (2018) reported on the use of InSAR to monitor subsidence in the Liulin District, China, during 2003 to 2011. The results of the study suggest that the surface is largely stable over the observation period. The findings are questionable, however, due to peculiarities in the workflow. The SAR data used are prone to large errors due (in part) to poor constraint of the satellites' orbital tubes. The interferogram network used does not attempt to mitigate this factor and even suggests that different acquisitions have identical baselines, which is extremely unlikely given the orbital tube constraints. The wrapped interferograms clearly contain a strong topographic signal. This shows the workflow is inadequate in mitigating this signal and it will impact the final surface movement signal calculations. Beyond these examples, the most widespread and advanced application of InSAR to monitor CSG-induced subsidence now occurs within Australia. Two such examples are discussed in the remainder of this section.

The Camden Environmental Monitoring Project (CEMP)

A recent study commissioned by Geoscience Australia (Garthwaite & Fuhrmann, 2020) used InSAR and GPS to identify subsidence over the Camden Gas Project (CGP), which is located approximately 65 km southwest of Sydney. A total of 144 producing gas wells have been drilled in the CGP since it was commissioned in 2001. However, these are being progressively decommissioned and all production is scheduled to end in 2023 (AGL, 2022).

As a part of the CEMP, a new geodetic monitoring network was installed to facilitate direct comparison between the InSAR and GPS measurements. The locations of the 20 new geodetic monitoring sites, CA01 to CA20, are shown relative to the location of the CGP wells in Figure 24. Of these sites, 16 were used to acquire campaign measurements, while the other four measured continuously. Each measurement campaign involved collecting 24 hours of GPS observations concurrently across all geodetic monitoring sites in the network, at approximately monthly intervals. These data were supplemented with data from three pre-existing, continuously operating reference stations from the CORSnet-NSW network (NSW Department of Customer Services Spatial Services, 2020).

InSAR data from three satellite missions were used in the analysis. These included Envisat, a C-band (56 mm wavelength) radar operational between 2006 and 2012, ALOS, an L-band (236 mm wavelength) radar operational between 2006 and 2011, and RADARSAT-2, a C-band radar operational since 2007. Data from RADARSAT-2 were acquired during the period July 2015 to July 2019 for both ascending and descending tracks (see Figure 25(a)). Each track makes an acquisition every 24 days, with an offset of 12 days between them. The GAMMA interferometry software (Wegmüller & Werner, 1997) was used to generate a network of interferograms for every viewing geometry of each satellite. StaMPS (see Section 6.1) was then used to conduct independent time-series analysis of every interferogram network and derive LOS displacement and velocity data sets. Finally, the LOS displacement and velocity data from ascending and descending tracks were used to calculate vertical and horizontal surface displacement and velocity data for each satellite (Fuhrmann & Garthwaite, 2019).

The CEMP made some significant findings, which are briefly summarised here. The comparison of RADARSAT-2 and GPS data for the period July 2016 to June 2019 showed that the LOS displacements observed in ascending and descending InSAR tracks are relatively consistent and within 5 mm of the GPS displacements (which had to be

converted from the up-down, east-west coordinate system to LOS). This provided confidence in the InSAR technique as a large-scale subsidence monitoring system. In general, no significant subsidence was observed over the CGP. However, Envisat and RADARSAT-2 produced almost no useful data in that area because of the inability of the shorter wavelength (56 mm) to penetrate vegetation on the surface. Low coherence and poor data quality is also a challenge to InSAR observations at locations of intensive cropping within the Surat CMA. More broadly, the Envisat data in the period 2006 to 2010 showed 96.8% of velocity measurements to range between ±3 mm/yr. The RADARSAT-2 data in the period 2015 to 2019 showed 96.7% of velocities also being within the range of ±3 mm/yr, while the ALOS data showed that 78.0% of velocity values were within the uncertainty level of ±4.2 mm/yr. These small fluctuations were attributed to seasonal changes in soil moisture and associated shrinking and swelling. No correlation between subsidence and the location of CSG wells could be found. The most noticeable subsidence observed in this study was found to be located above underground coal mines in the Southern Coalfields, including 800 mm at the Tahmoor mine and 600 mm at the Appin longwall mine, as shown in Figure 25(b).

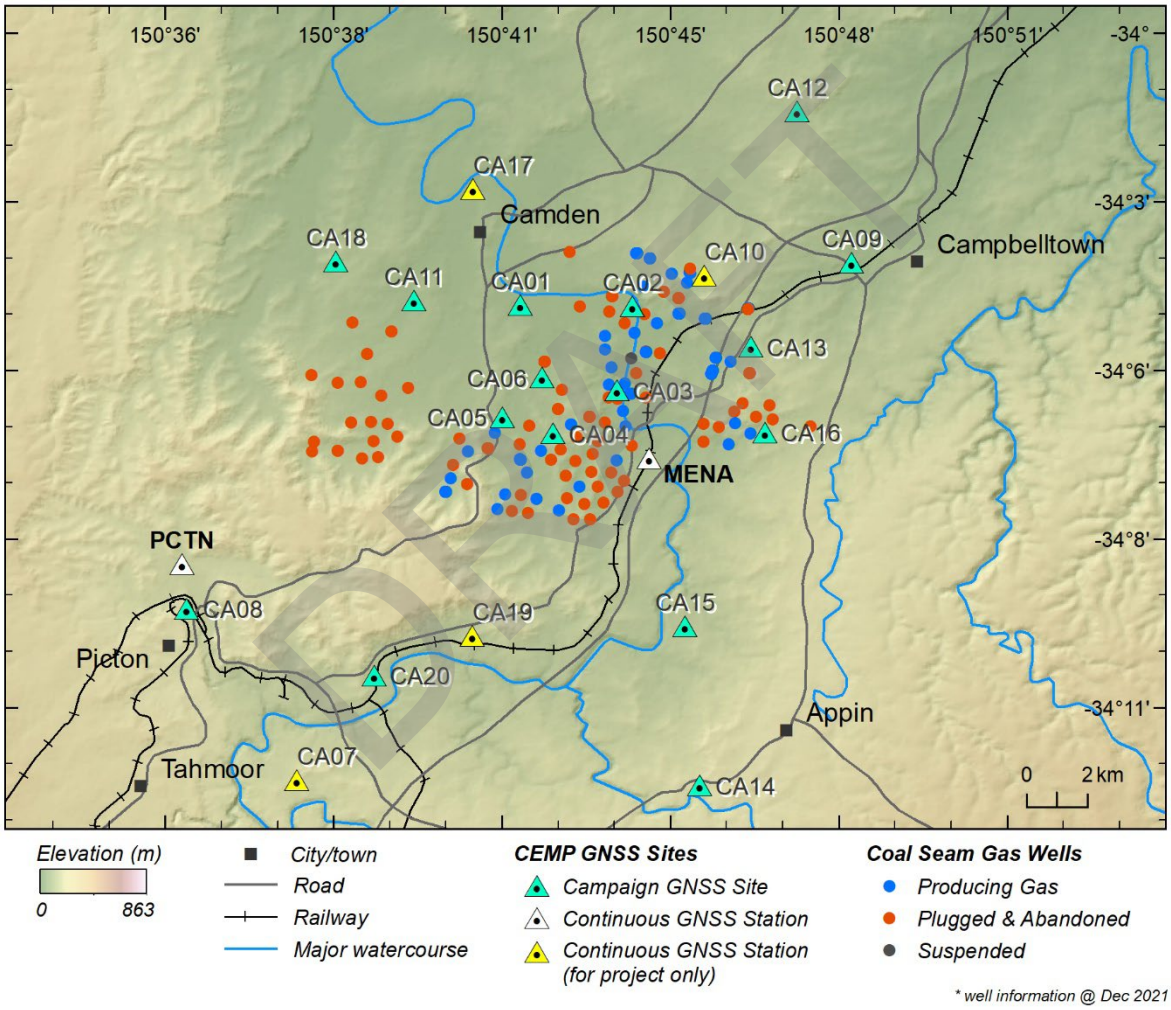

Figure 24: The location of geodetic monitoring sites installed as a part of the Camden Environmental Monitoring Project (Garthwaite & Fuhrmann, 2020) and the CSG wells, both producing and plugged and abandoned, of the Camden Gas Project.

The Underground Water Impact Report (UWIR)

Following legislative changes in 2016, the Queensland Office of Groundwater Impact Assessment (OGIA) is now required to report in its Underground Water Impact Report (UWIR) on subsidence that has occurred or is likely to occur. In the latest UWIR (OGIA, 2021), this was done by presenting an analysis of InSAR data along with

predictive modelling of compaction and subsidence. To support the InSAR analysis, OGIA acquired surface movement data that had been purchased by the major Queensland CSG producers (Santos, Origin Energy, Shell QGC, Arrow Energy) from a commercial provider. These data included ALOS observations at an interval of 46 days for the period 2006 to 2011, RADARSAT-2 observations at an interval of 24 days for the period 2012 to 2017, and Sentinel-1 observations at an interval of 12 days since 2015 (six-day interval from 2017 onwards). As had been identified by Masoudian et al. (2019b), background trends of surface movement are observed at locations remote from CSG production. In some locations, the trend suggests consistent downward movement (i.e. subsidence) with seasonal fluctuations due to rainfall. Such background trends will also exist above CSG fields, and so OGIA aimed to report on CSG-induced subsidence in the context of the surface movement baseline. This approach is necessary to try and understand impacts associated with CSG production.

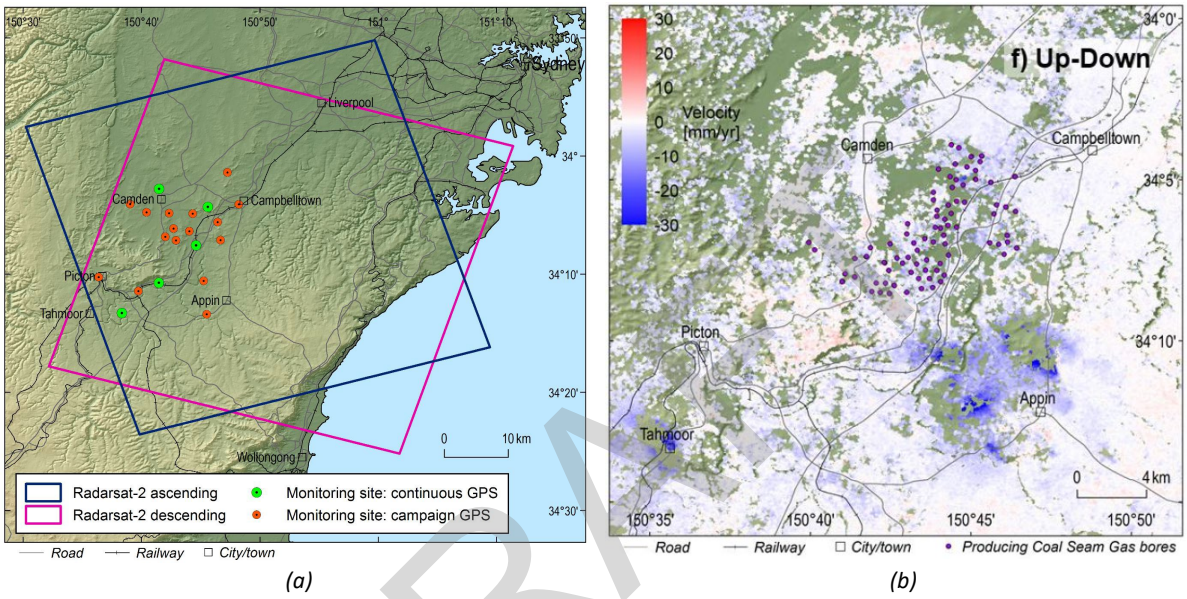

Figure 25: Aspects of the Camden Environmental Monitoring Project, showing (a) the overlap of the ascending and descending tracks of RADARSAT-2, and (b) the up-down velocity data from ALOS in the period 2008 to 2010 (reproduced from Garthwaite and Fuhrmann (2020)).

Interrogation of the InSAR data showed maximum downward surface movement of approximately 100 mm in the CSG fields in the east of the Surat CMA, which correlates well with the onset of CSG production in the area. Less surface movement was observed at the edge of these CSG fields. No significant surface movement was observed outside of these fields. These trends are summarised in Figure 26, including Figure 26(c) which indicates that the rate of subsidence might be reducing with time (OGIA, 2021).

Inspection of surface movement in non-producing regions, both within and outside the Condamine Alluvium, indicated velocities of up to 25 mm/yr and localised displacement fluctuations of 25 mm over a separation distance of 100 m. This is broadly consistent with the findings of Masoudian et al. (2019b), and was similarly attributed to variations in soil type in combination with changes in moisture content. Some regions of uplift were also observed in the eastern part of the Condamine Alluvium which appeared to correlate with rainfall pattern.

Poor coherence resulting in a lack of data coverage was also identified in cultivated regions. Nevertheless, it was inferred from the available data that surface movement within farms is highly variable, both spatially and temporally, and therefore it is not appropriate to use changes in surface elevation as a metric of the influence of CSG production.

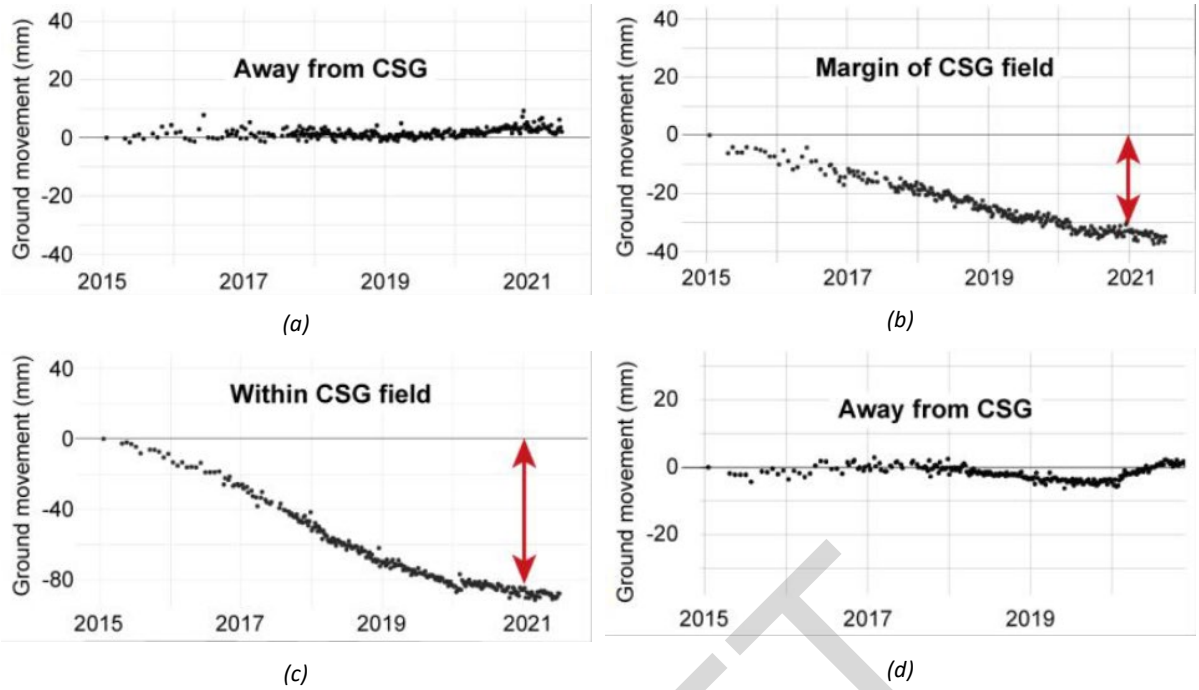

Figure 26: InSAR measurements of surface movement at four locations moving from west to east in the Surat CMA, including (a) approximately 15 km from CSG production on the western side, (b) at the boundary of CSG production on the western side, (c) within the CSG producing field, and (d) approximately 10 km from CSG production on the eastern side (reproduced from OGIA (2021)). Plots have been generated using an average of all surface movement data over respective squares of 250×250 m.

6.5 Subsidence monitoring strategies

Subsidence monitoring can be used to meet a number of objectives. These include quantification of the baseline trend of surface movement in areas where CSG is not (and will not be) produced as well as in petroleum leases prior to CSG development, estimation of the surface movement that is attributable to CSG-induced subsidence after production commences, and validating predictive tools for calculating CSG-induced subsidence. Further, surface movement data can be used to calibrate predictive models in a process called history-matching. However, this must be approached with caution because the surface movement signal from InSAR, for example, will aggregate the contribution from a number of additional processes (e.g. shrinking and swelling of soils) which might not be captured in the model being calibrated.

An example of best-practice subsidence monitoring is documented in Arrow Energy's 2022 Water Monitoring and Management Plan (Arrow Energy, 2022). This is comprised of large-scale InSAR monitoring of changes in ground surface elevation (i.e. surface movement), annual LiDAR surveys to monitor ground surface slope and any change in slope since the last survey, and geodetic measurement using a combination GNSS reference stations and survey markers as quality assurance on the InSAR and LiDAR data. The GNSS and survey locations were deliberately chosen to be adjacent to permanent scatterers, where the quality of InSAR is likely to be greatest, and to capture a diversity of land resource area (i.e. combination of geology, topography, soil, vegetation and land use) as well as spatial distribution across areas of CSG production.

This approach is recommended for the assessment of new developments, whereby InSAR is used for field-scale monitoring of elevation change, LiDAR is deployed only in locations that might be sensitive to small changes in slope or where InSAR coherence is poor or anticipated to degrade, and fixed monitoring stations are used as control on the two remote sensing techniques. To assist the determination of the surface movement baseline, both inside and outside a proposed CSG development, it is recommended that InSAR and LiDAR (where deemed necessary)

data acquisition commence prior to production to establish temporal trends. The interpretation and analysis of surface movement data should be supported by the ongoing monitoring of groundwater pressures.

The accessibility of InSAR data continues to increase including, for example, surface movement reporting by OGIA and Geoscience Australia. If necessary, commercial operators routinely provide processed InSAR data as a service. Further, surface movement mapping can be completed independently using the free and open data acquired by the European Space Agency's Sentinel satellites. Similarly, a number of companies can provide aerial LiDAR survey.

7. Approaches to Subsidence Assessment

Subsidence is the manifestation of subsurface compaction driven by fluid extraction and the resultant interaction of the remaining fluid and porous solid. Consequently, predictions of subsidence (or uplift) require an approach that considers both of these coupled processes (i.e. fluid dynamics and solid mechanics). By extension, the quality of subsidence predictions is heavily dependent on the quality of predictions of water (and in the context of CSG production, gas) flow in the subsurface.

The geomechanical response of a compressible formation depends on the geological characteristics of the in-situ rock and the tectonic stress environment, which in combination with the pressure and temperature variation profile, defines the stress path controlling elastic and inelastic behaviour. However, real geometries are large and complex, and the properties required for making predictions are commonly subject to a large degree of uncertainty. Therefore, a range of different strategies, of varying complexity and fidelity, are available for the prediction of the poroelastic behaviour that drives subsidence and uplift. These techniques can be divided into two classes, namely analytical or semi-analytical closed-form solutions, and numerical methods. These are discussed briefly in this chapter.

Any change in surface elevation associated with CSG production will typically be a result of the summation of volume changes in a number of geological units underground. Within the Surat CMA, the compaction of a number of coal seams (of varying thickness) and interbedded sedimentary units will propagate through overlying geological units with some degree of attenuation. These units include surficial alluvial aquifer systems such as sands or clays, which would be expected to grow in thickness with proximity to drainage paths (i.e. rivers), and underlying consolidated sedimentary strata such as sandstones, siltstones, or mudstones (Best et al., 2014).

As an older sedimentary basin, the Bowen Basin tends to exhibit lower permeability geological units, while the younger Surat Basin tends to possess higher-permeability geological units. On this information alone, one could assume that poroelastic compaction would be more prevalent in the Surat than in the Bowen. Its geological history means that the Permian coals in the Bowen Basin tend to have relatively low permeability. Produced water is lower, which is another indicator that subsidence could be expected to be lower. In the Surat Basin, produced water is greater due to higher permeability. However, it can take much longer to reach the target seam pressure (i.e. up to months). This could be a proxy for greater compaction associated with production. In the regions within proximity of Australian CSG production, the geological units most likely to undergo compaction are sandstones and claystones (Best et al., 2014). So, whilst compaction would be expected to be greatest within the dewatered coal-bearing formation, the compaction of other strata, and their subsequent contribution to subsidence, cannot be discounted. This applies also to locations where groundwater is pumped for water supply.

7.1 Analytical, semi-analytical and closed-form solutions

These techniques typically rely on a number of simplifications of the problem in order to provide a solution. They can be formulated using one-dimensional Terzaghi consolidation, an elastic half-space (Booker & Carter, 1986, 1987), or a nucleus of strain concept (Fokker, 2002; Fokker & Orlic, 2006; Geertsma, 1973). Tractable solutions to such models require assumptions about the mechanical properties of the strata (i.e. elastic) and the stratigraphy itself (i.e. continuous). However, the superposition of a number of solutions (e.g. multiple strain nuclei) can generate solutions in the presence of multiple wells.

Calderhead et al. (2011) employed one-dimensional Terzaghi consolidation on top of a three-dimensional flow model to simulate land subsidence in Toluca Valley, Mexico, as a result of groundwater abstraction. Borehole extensometers and InSAR data were employed for the model validation. Similar modelling work was performed

by Gambolati and Freeze (1973) and Gambolati (1974) to simulate subsidence caused by groundwater withdrawal at Venice, Italy. This work employed a three-dimensional finite element flow model alongside a one-dimensional land subsidence model. Similar methodologies have been widely employed to predict future surface movements at sites that contain comprehensive records of groundwater level changes along with borehole extensometer derived compaction-subsidence data (Epstein, 1987; Hanson, 1988; Helm, 1984; Helm, 1978; Liu & Helm, 2008a, 2008b; Pope & Burbey, 2003; Pope & Burbey, 2004). MODFLOW-based software packages can be employed for such modelling methodologies.

The one-dimensional consolidation model assumes rock deformation only in the vertical direction and horizontal displacements are generally ignored under the uniaxial strain assumption. This is necessary to make the analytical calculations tractable. The work of Wolff (1970) was perhaps the first case to highlight the importance of the inclusion of horizontal strains. Burbey (2001b) demonstrated that the use of a 1D consolidation model, while ignoring horizontal deformation, could lead to overestimation of vertical compaction.

Best et al. (2014) demonstrated the use of one-dimensional consolidation to predict compaction in a synthetic model based on conditions representative of a CSG producing region. The coal seams were homogenised into a coal bearing formation, and as such were assigned averaged geomechanical and hydraulic properties. It was assumed that the rocks above the coal remain saturated, ignoring the potential for significant changes in the water table. This model was tested with an increasing amount of model complexity, using four different formulations:

1. Uniform geology model: 1D consolidation model, groundwater at steady state, uniform hydraulic and consolidation properties. Predicted a total subsidence of 97 mm;
2. Variable permeability model: 1D consolidation model, groundwater at steady state, varying hydraulic properties, uniform consolidation properties. Predicted a total subsidence of 86 mm;
3. Variable ground model: 1D consolidation model, groundwater at steady state, variable hydraulic and consolidation properties. Predicted a total subsidence of 72 mm;
4. Transient groundwater flow model: 1D consolidation model, transient 2D analysis of groundwater head due to source/sink using ECLIPSE and SEEP/W. Predicted subsidence of 38 mm after two years in the vicinity of the well.

The results show that the one-dimensional variants of the consolidation model give similar estimates of subsidence. By solving for the pore pressure field, the transient model generated a significantly lower prediction of subsidence, which is likely to be more realistic (in the context of contemporary InSAR observations). This approach also facilitated the investigation of a two-dimensional well configuration and their interaction.

Other analytical and semi-analytical models grounded on poroelastic theory have also been employed for surface movement prediction with some success. Brown et al. (2014) used the analytical solution of Geertsma (1973) to model the surface movement due to CSG operations in the Surat Basin. To test the validity of the analytical model, its predictions for surface deformations were compared with the results from a 3D coupled numerical model employed by Tenthorey et al. (2013) for the Iona gas field. The surface subsidence and uplift predictions of the analytical model were reasonable when compared with the results of the numerical model.

More recently, Wu et al. (2018) compared predictions of CSG-induced subsidence made using two analytical solutions and one numerical solution. The analytical solutions were based on a disc-shaped reservoir with the nucleus of strain concept (Geertsma, 1973), and uniaxial compaction (including desorption-induced shrinkage). The numerical solution was based on a finite element solution for linear elastic solid mechanics and two-phase Darcy flow solved using COMSOL. Subsidence predictions from the nucleus of strain model were unable to incorporate the permeability of layers above the coal seam and were also found to be heavily dependent on the assumed depth. The uniaxial compaction solution, by definition, could not incorporate lateral variations in pressure distribution that

drive subsidence. Ultimately, it was shown that CSG-induced subsidence is difficult to predict using analytical methods due to the complex response of pore pressure within the typically discontinuous geological profile.

In summary, Terzaghi's one-dimensional consolidation theory, in conjunction with 1D or 3D flow models, is regarded as the conventional modelling approach to modelling subsidence among most groundwater hydrogeologists (Hsieh, 1996). One-dimensional consolidation has underpinned the majority of CSG-induced subsidence estimates to date (see Section 9.1). Gambolati et al. (2000) and Burbey (2001b) demonstrated that both approaches, 1D compaction theory and 3D poroelasticity theory, yield similar values of head and volume deformation distributions. But when it comes to simulating the displacement field, the conventional 1D approach has fallen short, especially near the pumping centres and in the heterogeneous regions of the aquifer where the horizontal deformations are large (Burbey, 2001a, 2001b, 2002). Heterogeneity or nonlinearity will limit the application of analytical models for surface deformation predictions.

7.2 Numerical modelling in two and three dimensions

Poroelastic modelling is a coupled, three-dimensional consolidation approach based on the Biot (1941) equations, which aims to predict both vertical and horizontal surface deformations in the context of subsidence. Poroelastic modelling can fully describe the coupled behaviour of an aquifer system while considering both flow and deformation. The first process involves modelling of porous media flow in order to predict the pressure variation within the aquifer. The second process entails the quantification of rock deformation in response to the pressure variations. Popular options for modelling (single phase) groundwater flow include MODFLOW, FEFLOW and SEEP/W. The simultaneous transport of water and gas is an important aspect of CSG reservoirs, so multiphase reservoir simulators such as INTERSECT or GEM can be employed to more accurately capture the pressure field. For full 3D geomechanical simulation of compaction and subsidence, commercially available finite element (FEM) or finite difference (FD) modelling packages such as VISAGE, Elfen, PLAXIS, ABAQUS, SLOPE/W, and FLAC can be employed. Assuming they are applied in a manner consistent with their formulation, any combination of these software packages could be employed to analyse CSG-induced subsidence. This is, however, not an exhaustive list of the available packages.

There is a number of published cases in hydrogeology where finite element solutions have been employed to analyse soil compaction and land subsidence (Sandhu, 1979). Lewis and Schrefler (1978) carried out coupled poroelastic modelling to simulate the land subsidence for Venice, Italy. Safai and Pinder (1979), Safai and Pinder (1980), Bear and Corapcioglu (1981), Hsieh (1996), and Burbey and Helm (1999) all present examples of this coupled modelling approach. Hernandez-Marin and Burbey (2010), Hernandez-Marin and Burbey (2012), and Yeh and O'Sullivan (2007) document the application of FEM packages ABAQUS and ANSYS for the prediction of surface movement. ABAQUS has also been demonstrated to successfully reproduce surface heave observed by tiltmeters during an aquifer recharge test in Upper Palatine, Germany (Jahr et al., 2008; Teatini et al., 2011).

While standard poroelastic modelling assumes linear elastic behaviour of the rock, this assumption can become invalid for an aquifer undergoing cyclic fluid extraction and injection (e.g. unconsolidated strata subject to grain realignment). For such conditions, elastoplastic models need to be considered. Budhu et al. (2014) employed the modified Cam-Clay (Roscoe & Burland, 1968) elastoplastic model to simulate uplift due to flow from injection ponds. The results from the model were validated against InSAR-derived uplift data. In the Yangtze Delta, China, a subloading Cam-Clay model in ABAQUS was employed for simulation of surface uplift due to artificial groundwater recharge. A field test was carried out to model the uplift for the city of Shanghai and the behaviour of both soil and water was modelled under cyclic loading conditions. The results from this model proved to be more reliable as compared to standard elastic modelling simulations. The study concluded that this numerical model can successfully capture the surface rebound as a result of artificial recharge (Huang et al., 2015).

The shortcomings of 1D compaction models, and other analytical solutions, in accurately predicting the magnitudes of surface movement, both in the vertical and horizontal directions, thus points to the superiority of two- and three-dimensional poroelastic modelling for more precise prediction of surface movement. Such numerical methods allow full, two-way coupling between porous media flow and geomechanics, heterogeneous stratigraphy and material properties, and the inclusion of geological discontinuities (if discrete element contact is included). However, the additional model complexity requires additional model parameters, which may not be available, and highlights issues related to the subsurface heterogeneity of coals (see Section 7.4). Best et al. (2014) noted that surface movement could become prominent at locations where a fault intersects a coal seam and the surface, as this has the potential to result in a discontinuity in the otherwise smooth spatial distribution of surface movement observations. The ability to explicitly capture such features in both flow and geomechanical models could be beneficial.

Geomechanical modelling will capture the three-dimensional nature of the stress and strain field and, therefore, help identify conditions which either exacerbate or mask any movement at the surface. In one-dimensional consolidation theory, the summation of the compaction of all porous strata will give a worst-case estimate of the deformation at the surface. In reality, the geomechanical properties of the geological units have the potential to attenuate some of the subsurface compaction (e.g. a strong intermediate layer acting as a support for underlying compaction). A geomechanical model will capture this effect, along with movement that occurs in the horizontal direction. A 3D prediction of the pore pressure and stress field will also provide information of the magnitude of subsidence with increasing distance from bores.

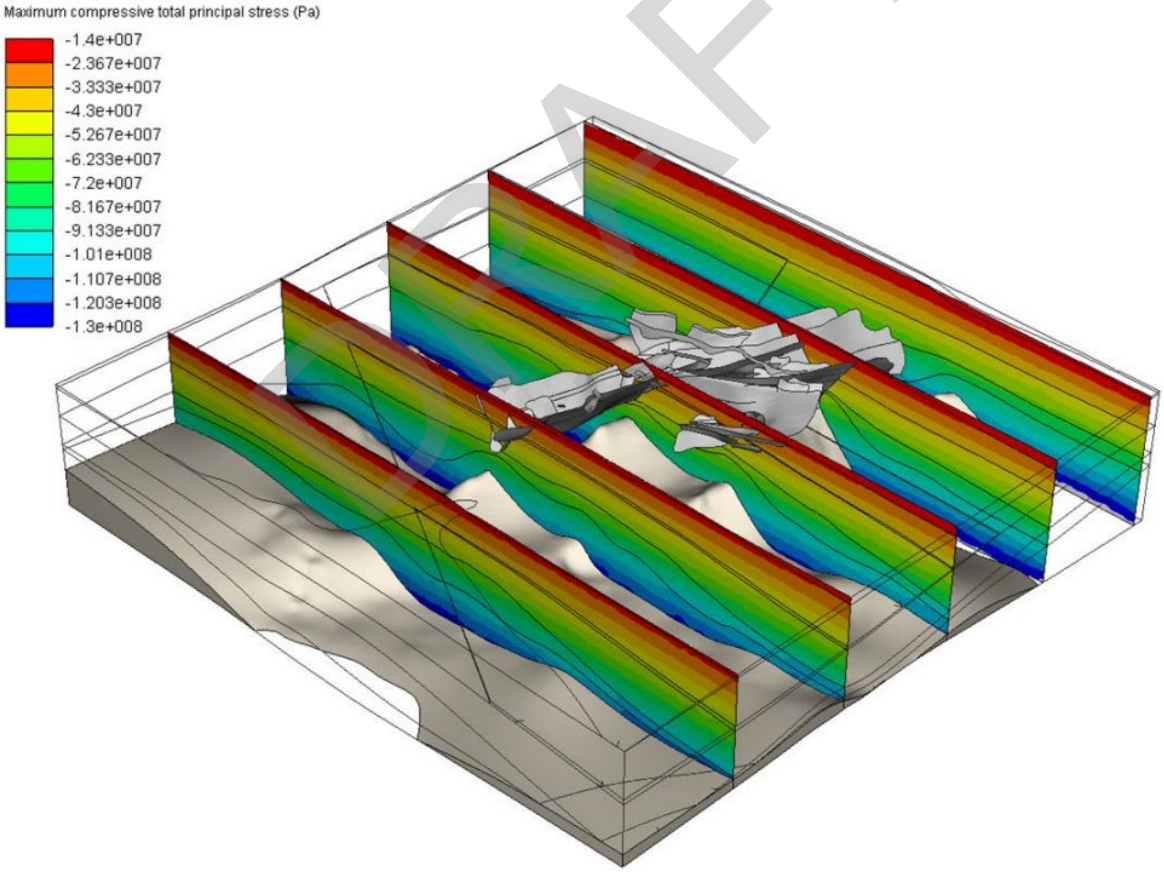

Figure 27: An example of a faulted, three-dimensional finite element model of compaction showing the distribution of the pre-production maximum compressive total principal stress within the field (reproduced from Ferguson et al. (2016)).

Finally, the use of a FEM model allows a choice between either static or transient modelling of the pore pressure and saturation distribution. In the static approach, pore pressure and saturation can be prescribed at each location in the modelling using data from hydrographs or the outputs of a fluid flow simulation. In the transient approach, the

software could be used to simultaneously model the evolution of pore pressure, saturation and stress in response to liquid pumping (or recharge). Alternatively, this could be performed by coupling the FEM software to a dedicated code such as ECLIPSE, MODFLOW, FEFLOW or SEEP/W.

As an example of advanced numerical modelling of reservoir depletion, Ferguson et al. (2016) used the finite element-discrete element code Elfen to model the stress evolution and assess fault reactivation as a result of production from an offshore Brazilian oil field. The model domain (see Figure 27) measured 25 km × 25 km and explicitly included a network of major faults. Porosity was modelled as depth-dependent, initial pore pressures were assumed hydrostatic, and the model was then run to determine the pre-production stress state. The initial pore pressure distribution was then modified using results of a reservoir simulation of production, and the post-production stress was calculated. Subsidence at the sea floor was predicted to be 1.9 m, and the maximum fault slip due to compaction was found to be 0.8 m.

7.3 Advanced numerical modelling: Internal and external shrinkage

As described in Section 3.4, coal is usually simplified as an assemblage of matrix blocks separated by orthogonal cleat sets and bedding plies. Models based on the resultant matchstick geometry have subsequently been developed to describe the change in effective stress and permeability that occurs with pressure change and processes such as sorption-induced shrinking or swelling. Such models assume that the matrix blocks are completely isolated by the cleats between them, which is not physically possible. In recognition of this, Wang et al. (2014) argued that the matrix blocks must be connected by bridges that traverse the cleats, as shown in Figure 28. During gas adsorption under confined geomechanical conditions, the coal bridge and the local matrix block around the cleat would swell. Because of the larger area of the matrix block, its swelling force is greater than that of the matrix bridge and as a result the coal bridge and the cleat are compressed by the *internal swelling* of the matrix block. As gas continues to diffuse into the matrix, the swelling front advances into the blocks and causes *external swelling*. The internal swelling effect leads to reduced cleat aperture and, consequently, reduced permeability of the coal seam. The external swelling, however, leads to the expansion of bulk coal (cleat-matrix system), as shown in Figure 28.

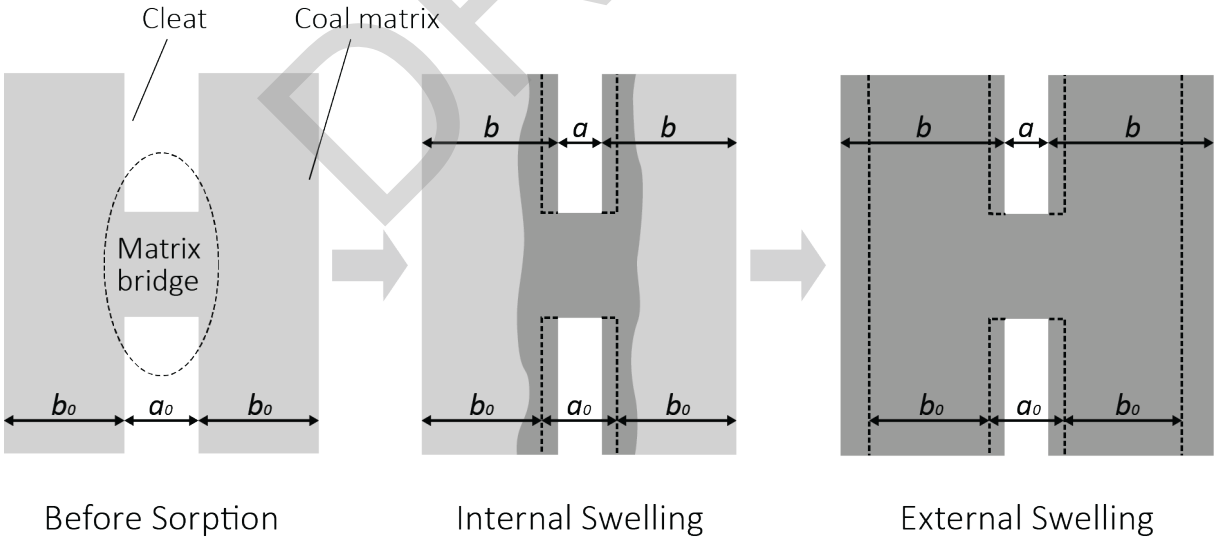

Figure 28: Schematic diagrams highlighting the concepts of internal and external swelling and shrinking, showing (a) the conceptual model of a matrix bridge, (b) internal swelling resulting in cleat width narrowing from a_0 to a, and (c) external swelling resulting in volumetric expansion of the matrix width from b_0 to b (reproduced from Wang et al. (2014)).

Masoudian et al. (2019a) applied the concept of internal and external shrinkage to a two-dimensional model of subsidence around a single CSG well. The internal shrinkage contributed to changes in cleat geometry and permeability while the external shrinkage contributed to bulk volumetric changes of the coal seam at the field scale.

Therefore, only a fraction of the Langmuir shrinkage, ε^s, was apportioned to the internal shrinkage (and subsequent permeability update),

$$\varepsilon_{in}^s = F_{in}\varepsilon^s, \quad (16)$$

with the balance apportioned to the external shrinkage and bulk deformation of the coal seam,

$$\varepsilon_{ex}^s = (1 - F_{in})\varepsilon^s \quad (17)$$

The distribution of internal and external shrinkage is thus governed by the model parameter, F_{in}, which may be a function of coal structure, cleat aperture (porosity), and confining stress (Wang et al., 2014; Zang et al., 2015). The internal and external shrinkage terms were then employed in the calculation of permeability and stress, respectively.

The model developed by Masoudian et al. (2019a) was applied to a case study inspired by the simplified stratigraphy presented by Best et al. (2014), except three thinner coal bearing formations were used in place of a single one. The results clearly showed the competing effects of internal shrinkage and higher permeability versus external shrinkage and greater compaction. Increased permeability led to more uniform pressure depletion within the coal bearing formations and, therefore, a more uniform subsidence profile at the surface. Increased volumetric shrinkage, and thus less permeability enhancement, led to a more pronounced subsidence bowl around the well. For F_{in} values of 0.9, 0.5, and 0.2, the maximum subsidence predicted was 90 mm, 112 mm, and 105 mm, respectively, as shown in Figure 29(a). This showed that the relationship between F_{in} and subsidence is not monotonic, and that there is a combination of permeability enhancement (and thus reservoir depletion) and volumetric shrinkage that results in maximum subsidence. The results also confirmed what is widely understood; that most of the subsidence signature comes from compaction of the coal layers, as shown in Figure 29(b).

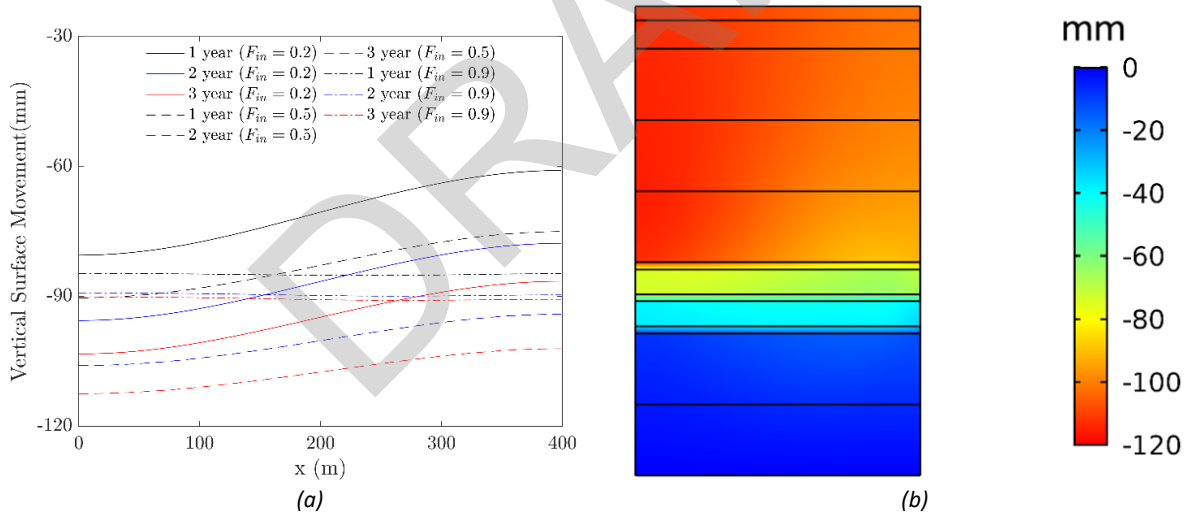

Figure 29: A selection of results from the modelling of subsidence with internal and external shrinkage incorporated, showing (a) the distribution of subsidence around the well at different depressurisation times and values of F_{in}, and (b) the compaction distribution throughout the subsurface (reproduced from Masoudian et al. (2019a)).

7.4 Advanced numerical modelling: Stochastic stratigraphy

One of the most significant challenges associated with modelling the subsurface flow and geomechanics that drive compaction and subsidence lies in determining the input parameters for the associated governing equations (e.g. the distribution of coal and non-coal materials, the distribution of relative permeability for two-phase Darcy flow). The challenge relates not only to a choice of each parameter value, but how those values are distributed within the model. Some of the key parameters that this applies to include porosity, permeability, compressibility, relative permeability, capillary pressure, Young's modulus, Poisson's ratio, Langmuir volume, Langmuir pressure, and gas content.

In reality, the subsurface is often extremely heterogeneous, but this heterogeneity can be difficult to capture in the models used to predict the pressure changes used in calculations of subsidence. As an example of this, one can consider the Walloon Coal Measures (i.e. the target of CSG production in the Surat Basin). It has been noted (e.g. by Cardwell (2018)) that the coal measures vary significantly between wells at relatively short (e.g. 50 m) spacing, with entire coal packages appearing or disappearing over this distance. This clearly presents a challenge when trying to create models based on data gathered at a more typical CSG well spacing of 750 m.

One approach to model these coal measures is to create relatively simple *layered* models, where coal packages are represented by coal and non-coal (i.e. interburden) layers (Masoudian et al., 2019a; OGIA, 2021; Wu et al., 2018). While this is likely to result in models that are relatively straightforward to create and run, the issues with parameterising these upscaled models would still need addressing. This is a particular issue in the Walloon Coal Measures where the coal and interburden have significantly different properties, making upscaling challenging (Cardwell, 2018).

An alternative to layered models would be to use geostatistical modelling such as kriging, Gaussian simulation, or simulated annealing to represent extreme subsurface heterogeneity. To illustrate how heterogeneity influences depressurisation and compaction within coals, two models covering an area of 750 m × 750 m were created based on an approximately 80 m-thick section of a real CSG well. Using wireline logs from the well, coal intervals were identified. In one of the models, each of these coal intervals was represented by a homogenous coal layer, with interburden layers between these, resulting in 20 layers in total. The other model was structurally identical to the layered model, but with heterogenous layers that could contain both coal and interburden (but which would match the coal present in the wireline log). Both models were parameterised with typical properties from the Walloon Coal Measures, where the coal has significantly higher permeability than the interburden. In the layered model each layer was homogenous, and was assigned a single permeability value, while the heterogeneous model had permeabilities that varied across any individual layer, as shown in Figure 30. The spatial distribution of coal and permeability within the layers of the heterogeneous model was populated using copula geostatistics (Hoerning & Rodger, 2021).

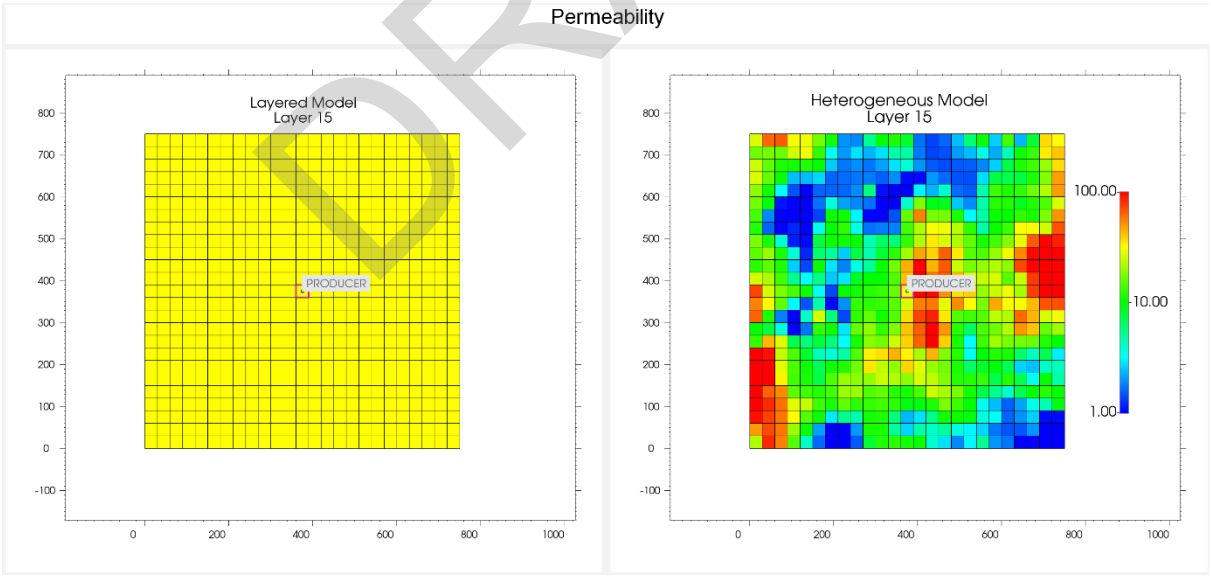

Figure 30: Permeabilities in layer 15 of the (a) layered and (b) heterogeneous models. Note that the value at the well location (i.e. in the centre of the model domain) is identical.

These models were used to simulate one year of production from a well in the centre of the model domain using CMG's GEM compositional simulator, including using GEM's geomechanical model to predict compaction of the modelled layers. The depletion in the various layers after one year is shown in Figure 31(a, b) and the compaction calculated after one year of production is shown in Figure 31(c, d). Compaction in the layered model is predicted to

be almost perfectly radial (i.e. decreasing with distance from the well) and is distributed much more evenly across the model domain. The heterogeneous model shows more variation in compaction due to the discontinuous nature of the coal within the model (which could be considered a more realistic representation of the Walloon Coal Measures). The execution of a large number of subsurface realisations, based on the statistics derived from well logs, could thus be used to generate a stochastic distribution of compaction and subsidence probability around a well, rather than a single deterministic value. Note that the compaction calculations shown in Figure 31(c, d) do not include the mechanical contribution of any overburden, which would attenuate the localised compaction seen around the well as it propagated to the surface as subsidence.

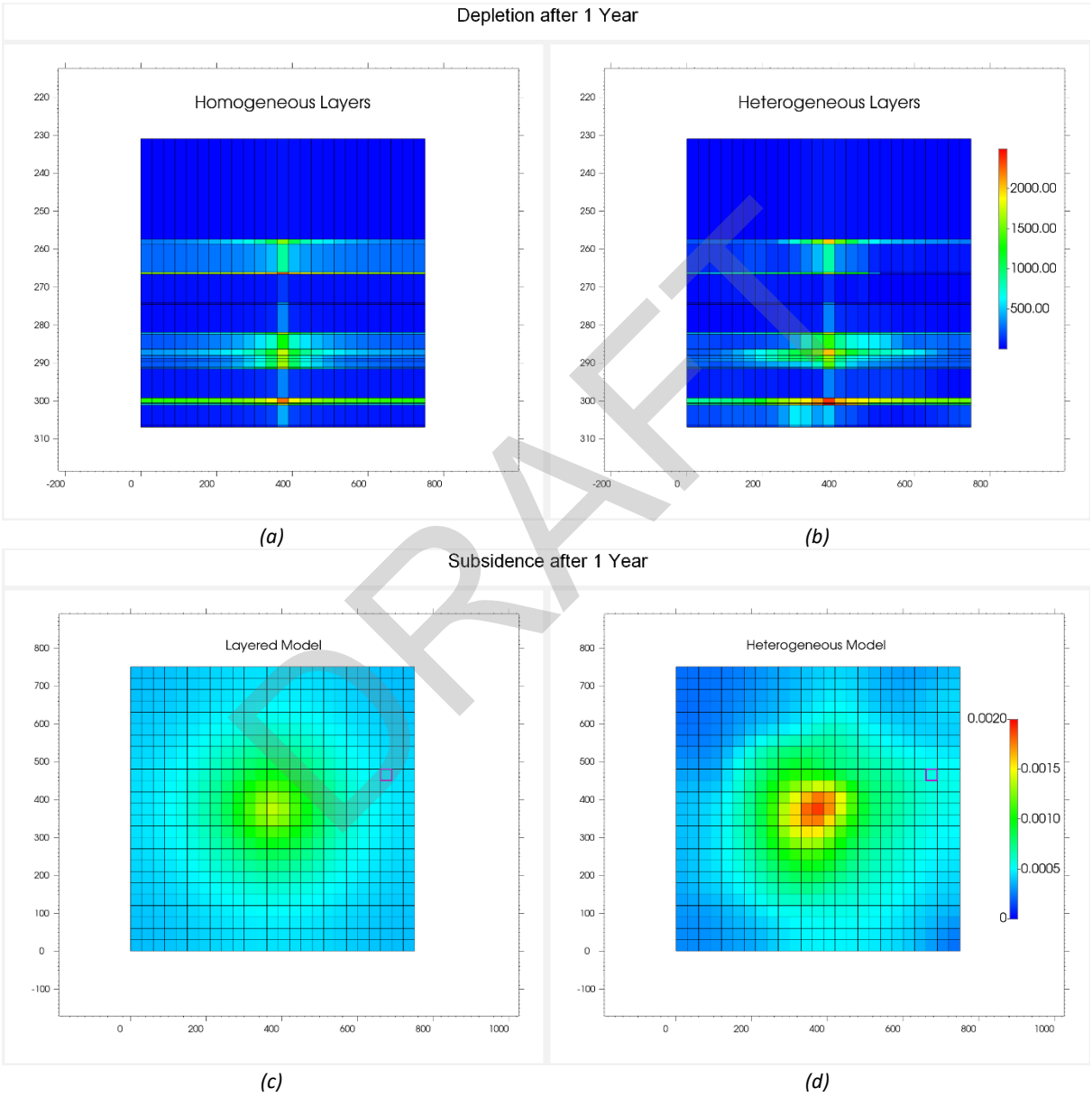

Figure 31: Comparison of subsurface pressure distribution for (a) the layered model, and (b) the heterogeneous model, as well as the layer compaction (not surface subsidence) for (c) the layered model, and (d) the heterogeneous model.

7.5 Integration of InSAR data

The integration of surface movement observations, such as those from InSAR, can be incorporated into the predictions associated with compaction and subsidence. Examples include model calibration or inverse modelling.

Inverse modelling can be used to understand the subsurface processes that result in subsidence, such as changes in reservoir pressure or the influence of an aquifer that is driving reservoir production, and improve estimates of flow and geomechanical parameters. For example, Fokker (2002) used inverse modelling to estimate the change of mass in a reservoir based on measurements of surface subsidence. The subsidence predictions made using a forward model were used as an input to the inverse model to quantify the sensitivity of the process to the smoothing process, the precision of the forward model, and the experimental design. This work demonstrated that well-characterised subsurface material properties are necessary to derive benefit from the inverse modelling approach utilised.

In the work of Muntendam-Bos et al. (2008), a time-dependent inversion scheme for resolving temporal reservoir pressure changes from subsidence data was presented. The scheme was able to accommodate the intermittent absence of data at a location, as well as introduce data at a new location at any time. The temporal nature of the model made it possible to identify any delay, or temporal lag, in reservoir compaction following a driving event (e.g. change in reservoir or aquifer pressure). This work used the same analytic, linear forward model presented in Fokker (2002) that was based on the nucleus of strain concept (Geertsma, 1973) and subsequently applied and improved by others. In this work, compaction was assumed to be linear. An alternative to this type of simplified model is to use computational methods, which is more expensive in terms of forward modelling and more complicated to incorporate in inverse modelling. The presented model was validated using a synthetic case study based on a gas field in the northern Netherlands. This was done by comparing the inversion results, which were generated using the estimates of compaction or pressure drop from the forward model, to the original input data. Results showed that the time-dependent inversion process performed better than the static scheme presented in earlier works.

Reeves et al. (2014) explored the use of InSAR data, which is both spatially and temporally dense, to infill spatial information on the hydraulic head in the confined aquifer system in the San Luis Valley, USA. This study, however, focused on generating greater temporal, as opposed to spatial, resolution of the hydraulic head measurements, as actual observations can be quite infrequent (approximately one year apart). One of the main motivators for this work was the lack of hydraulic head measurements in the valley, as these are useful in the calibration of groundwater flow models. In this work, it was assumed that any observed surface elevation changes were directly related to changes in thickness of the confined aquifer system stemming from groundwater abstraction or recharge. A stochastic technique was used to incorporate uncertainty in the simple kriging model. The predicted heads showed reasonable correspondence with the measured values. However, it was suggested that atmospheric phase effects, which were shown to be present but not quantified, could have degraded results.

In recent years, an increasing number of studies of this kind have appeared in the literature. Chen et al. (2016) estimated storage coefficients and the temporal lag between subsidence measurements and head change using a combined analysis of InSAR and well data. InSAR data were also used to estimate aquifer head over a broader region in the presence of significant decorrelation due to vegetation, as this is where monitoring wells are usually located. Fuhrmann et al. (2015) used a combination of InSAR, global navigation satellite system (GNSS), and levelling measurements to calculate the velocity of movement of the Upper Rhone Graben in central Europe. They found a vertical subsidence of 0.5 mm per year along with a horizontal displacement of 0.8 mm per year in the southeast direction. Fakhri and Kalliola (2015) used InSAR techniques to monitor surface movement in the region of Larissa in central Greece. Interferometry was used to monitor short-term changes between observations (i.e. separated by one satellite period of 35 days), while interferometric stacking was used to monitor long-term changes over a period of 13 years. Finally, Tomás et al. (2014) discussed the advantages and limitations of using differential InSAR to monitor surface movement, with a focus on applications in Spain.

InSAR data assimilation has continued to evolve such that the state-of-the-art is able to account for and reduce the uncertainties associated with flow and geomechanical modelling in a stochastic framework (Gazzola et al., 2021). Further, Candela et al. (2022) showed that it was possible to discriminate which rock compaction model driving subsidence was activated at depth. Similar model calibration using InSAR data is now undertaken by OGIA in its series of Underground Water Impact Reports (OGIA, 2021).

8. Selection of Modelling Parameters

This chapter provides guidance on the selection of modelling parameters used in the calculation of compaction and subsidence. Irrespective of whether an analytical or numerical approach is taken, this requires material properties related to linear poroelasticity (Young's modulus, E, Poisson's ratio, ν, and Biot coefficient, α) and desorption-induced shrinkage (Langmuir constant, b_L, and maximum volumetric swelling strain, ε_L^s). Analytical solutions based on the concept of uniaxial strain commonly make use of the coefficient of compressibility, C_m, however this can be calculated directly from the Young's modulus and Poisson's ratio.

Calculation of the effective stress change that drives compaction requires an understanding of the in-situ stress state, including pore pressure, prior to the onset of production. This is typically performed by integrating well density logs to calculate the total vertical stress and applying poroelastic theory (and an understanding of prevailing tectonic strains) to calculate the total horizontal stress, both as a function of depth. The identification of borehole breakouts and tensile fractures in well image logs can be used to identify the orientation of maximum and minimum horizontal stresses. This basic workflow has been well documented in the oil and gas industry (Zoback, 2007), and as such is not discussed here.

The change in subsurface pressure distribution, which drives changes in effective stress, is best calculated via a computational reservoir or groundwater simulation (e.g. the work that underpins OGIA (2021)). In this context, comprehensive modelling of flow and geomechanics requires data or estimates for porosity, permeability, relative permeability, capillary pressure, Langmuir volume, Langmuir pressure, and gas content, in addition to poroelastic properties and the distribution and thickness of coals and other geological units. Guidance on reservoir simulation and the estimation of these parameters is beyond the scope of this document. However, a brief discussion of hydraulic conductivity is included in Section 8.3 to highlight the variability that exists in the geological units within the Surat CMA.

The calculation of the total compaction of coals and surface subsidence requires summation of contributions from all depressurised geological units as well as the behaviour of any additional overburden. Each will exhibit different material properties and variations within each unit will exist, both laterally and with depth. Exhaustive laboratory testing of all coal and rock layers is not feasible and, even if it were, it is challenged by differences in scale. For example, triaxial testing of competent rocks such as sandstone and shale is unable to capture the influence of natural fractures that are spaced metres apart and would act to reduce the stiffness and strength measured. A similar challenge exists with coal and cleats. In addition, it is also difficult to extract a core sample from the subsurface, where it exists under pressure, without fundamentally altering it (e.g. desorption of gas, opening of cleats) prior to testing. Many heavily cleated coals (i.e. the ones likely to exhibit the highest compressibility) cannot be subjected to standardised laboratory testing because core samples disintegrate once brought to the surface and destressed. To summarise, there exists wide natural variability in the parameters that contribute to subsidence prediction and varying degrees of uncertainty as to what those parameters are at any one location.

A common approach to managing the uncertainty associated with model parameters is to conduct an uncertainty analysis, in which a model is run for a number of different combinations of parameters, each of which is varied within an expected range (i.e. sensitivity analysis). In the context of subsurface pressure prediction, this can be accompanied by model calibration, or *history matching*, whereby parameters are adjusted so as to match field observations (e.g. monitored groundwater levels). This type of field-scale calibration is more difficult to achieve with poroelastic parameters.

8.1 Elastic properties: Young's modulus and Poisson's ratio

Young's modulus, E, is one of the coefficients that links stress and strain in a solid under the assumption of linear elasticity. It is, therefore, also referred to as the elastic modulus. The Young's modulus of many metals is typically isotropic and scale-independent. In sedimentary rocks, however, the Young's modulus may be anisotropic, meaning that the value of E is different across two or more directions. Where natural fractures or other defects are presents, the bulk Young's modulus of the *rockmass* is typically lower than that of small, homogeneous samples (which are more likely to be used in laboratory testing). The presence of fractures and defects also means that bulk Young's modulus increases with applied stress, as these fractures and defects close under incrementally increasing load.

Poisson's ratio, ν, is another of the coefficients that links stress to strain in a linear elastic solid. It quantifies the deformation of a material perpendicular to the direction of loading. For example, in Figure 32(a) the column is subjected to vertical uniaxial stress, with no lateral constraint, and the Poisson effect causes it to widen as it shortens. Under uniaxial strain, where the same column is constrained laterally (i.e. zero strain), the Poisson effect results in the induction of transverse stresses and the shortening of the column is reduced, as shown in Figure 32(b). A rule of thumb for the Poisson's ratio of rocks is a value of approximately 0.25 whereas for Queensland coals it is commonly greater than 0.4. The upper bound of Poisson's ratio is 0.5, which means that the material is incompressible and any volumetric change due to shortening is accompanied by an equivalent volumetric change due to widening. Just like Young's modulus, it can be expected that the Poisson's ratio for coal and sedimentary rocks is anisotropic.

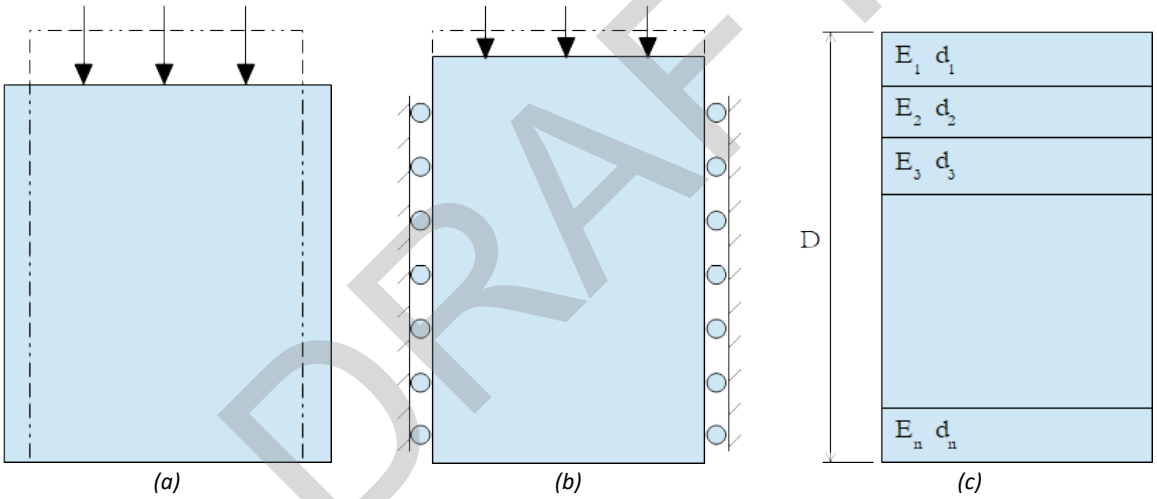

Figure 32: Aspects of linear elasticity, showing (a) the deformation of a column under uniaxial stress (i.e. laterally unconstrained), (b) the deformation of a column under uniaxial strain (i.e. laterally constrained), and (c) the different thickness (d_1, d_2, d_3) and Young's modulus (E_1, E_2, E_3) of adjacent geological units, where $D = \sum_{i=1}^{n} d_i$.

Representative values of Young's modulus for Australian coal and rocks can be sourced from the scientific literature, research reports, or directly from industry. For example, Gale and Fabjanczyk (1993) presented an overview of the relationship between Young's modulus and unconfined compressive strengths (UCS) for a range of Australian rock types, such as coal, shale, siltstone, and sandstone. This provides a crude approximation to one from the other. Similarly, Young's modulus may also be calculated from UCS using the Hoek-Brown rockmass strength criterion and an assessment of the geological strength index (GSI),

$$E = \sqrt{\frac{UCS}{100}}\, 10^{\frac{GSI-100}{40}}, \quad \text{.....(18)}$$

where E is in gigapascals and UCS is in megapascals (Galera et al., 2005).

In analytical and numerical calculations of compaction within the Surat CMA, it is usually necessary to upscale the properties of many thin, adjacent geological units, as shown in Figure 32(c). Based on the theory of elasticity, the

equivalent Young's modulus of a horizontally layered unit, with total thickness, D, undergoing vertical compression can be calculated in an analogous fashion to springs in series (resulting in an anisotropic equivalent elastic system),

$$\frac{D}{E} = \frac{d_1}{E_1} + \frac{d_2}{E_2} + \frac{d_3}{E_3} + \cdots + \frac{d_n}{E_n}, \quad (19)$$

where d_i and E_i are the thickness and Young's modulus of each layer.

As the CSG industry has expanded in Queensland, the library of experimentally determined material properties has also grown. For example, Arrow Energy used data from unconfined compression tests of consolidated rock samples from four wells on the Condamine Alluvium within the Surat Basin to undertake analytical subsidence calculations (Coffey Services Australia, 2021). A summary of the test results is presented in Table 4, where the Young's modulus is presented as the tangent value at the confining pressure rather than the secant value over the entire pressure range (recognising that the Young's modulus increases under increasing stress). The tangent value represents the slope (i.e. the instantaneous rate of change of stress with respect to strain) at the measurement point, whereas the secant value is calculated using the total change in stress and strain over the measurement range.

Table 4: Summary of Young's modulus values from four wells on the Condamine Alluvium.

Well Number	Depth Range (m)	Confining Pressure Range (MPa)	Young's Modulus Range (GPa)
1	140.0 – 451.1	3.5 – 11.2	2.0 – 4.3
2	200.0 – 298.3	5.0 – 6.7	4.5 – 9.0
3	282.7 – 471.4	7.0 – 11.7	5.2 – 5.7
4	203.9 – 478.5	5.1 – 11.9	3.0 – 6.6

Data sourced from Coffey Services Australia (2021)

Data from wireline sonic logs, which include an estimate of dynamic Young's modulus, were also presented. The physical mechanical response of a material is dependent on the rate at which it is loaded and the applied stress-strain amplitude. Logging-based measurements are in the kilohertz range, whereas actual physical loading rates (such as those that occur in situ or in laboratory testing) are generally much slower (quasi-static). By performing laboratory testing for measurement of Young's modulus and Poisson's ratio, and simultaneously measuring the dynamic response of core samples, it is possible to calibrate estimates of static Young's modulus across the entire profile of a well log. Based on triaxial testing of 22 sandstone cores, Fei et al. (2016) presented an empirical correlation for converting dynamic Young's modulus, E_d, values to static Young's modulus, E_s,

$$E_s = 0.564E_d - 3.4941, \quad (20)$$

where both moduli are in gigapascals. This relationship, however, applies to sandstone and is not appropriate for coal. Eissa and Kazi (1988) presented an alternative correlation which takes into account the material density, γ, which is also available from logs,

$$\log_{10}(E_s) = 0.02 + 0.77\log_{10}(\gamma E_d), \quad (21)$$

where both moduli are again in gigapascals and the density is in tonnes per cubic metre.

Origin Energy has previously collated detailed mechanical properties of coal and rocks via laboratory experiments (Schlumberger Reservoir Laboratories, 2017). Triaxial testing was employed to determine elastic properties (as well as anisotropic dynamic properties and Mohr-Coulomb failure properties) for a number of coal, shale and sandstone samples from three wells within the Surat Basin. A summary of the Young's modulus and Poisson's ratio for these

samples, and the depth from which they were collected, is presented in Table 5. Within the coal, shale, and sandstone samples, no strong correlation between elastic properties and depth was observed. However, most of the samples showed a clear increase in Young's modulus and Poisson's ratio with increasing confining pressure (two of the three shale samples were exceptions to this rule). Although there is some variability, the coal data suggest that values of 3 GPa and 0.40 are good approximations of the Young's modulus and Poisson's ratio of the samples tested.

The uniaxial compressibility values in Table 5 were calculated from the elastic properties as per Equation 10. It can be seen that the large Poisson's ratio for the coal samples constrains the compressibility values, such that they are of similar magnitude to the shales and sandstones. Similarly, the low Poisson's ratio of the sandstones helps increase compressibility, even in the presence of relatively large Young's modulus.

Table 5: Elastic properties of samples from three Surat Basin wells determined using triaxial testing

Material	Depth (m)	Young's Modulus (GPa)	Poisson's Ratio (-)	Uniaxial Compressibility (1/GPa)
Coal	509.19	2.963 – 3.240	0.40 – 0.41	0.133 – 0.158
Coal	579.52	3.019 – 3.351	0.41 – 0.43	0.116 – 0.132
Coal	621.21	3.182 – 3.487	0.42	0.112 – 0.123
Coal	641.67	3.219 – 3.433	0.40 – 0.41	0.125 – 0.145
Coal	651.61	3.030 – 3.227	0.43 – 0.45	0.085 – 0.116
Coal	656.29	3.110 – 3.396	0.41 – 0.44	0.091 – 0.138
Coal	727.73	3.028 – 3.389	0.41 – 0.43	0.104 – 0.142
Coal	732.64	2.840 – 2.941	0.43	0.119 – 0.124
Shale	370.05	4.413 – 4.817	0.39 – 0.47	0.035 – 0.114
Shale	502.60	6.587 – 7.612	0.20 – 0.23	0.118 – 0.131
Shale	636.36	2.541 – 3.591	0.38 – 0.39	0.140 – 0.210
Sandstone	385.14	4.012 – 4.547	0.21 – 0.22	0.195 – 0.221
Sandstone	530.36	5.822 – 6.977	0.23 – 0.24	0.123 – 0.148
Sandstone	607.12	6.887 – 8.743	0.24 – 0.26	0.097 – 0.119

Data sourced from Schlumberger Reservoir Laboratories (2017)

A recent report to the Australian Coal Association Research Program (ACARP) (Gray et al., 2019) investigated the anisotropy of coal and the dependence of elastic properties on confining stress. Triaxial testing was performed on 14 coal samples that had been collected from Central Queensland (no further location information is available in the report). A summary of the data from one of these samples (classified as a heavily-cleated, dull bright coal) is presented in Table 6. It can be seen that the vertical and horizontal Young's modulus, E_1 and E_2, increase to values of 3.78 GPa and 4.43 GPa, respectively, with increasing applied stress. The vertical and horizontal Poisson's ratio, ν_1

and ν_2, increase similarly. Anisotropy of the coal is most evident in the ratio of horizontal to vertical Young's modulus, which is 1.17:1 at the maximum confining pressure. The vertical and horizontal Poisson's ratio values remained quite similar.

A number of key points were summarised from this work. It reinforced the fact that the load response of coals is generally nonlinear within the elastic range, and that the tangent stiffness can increase by up to a factor of 10 with increasing confining stress. This results in values of Young's modulus which deviate significantly, both above and below, values that are widely accepted as standard. The elastic coal properties were sometimes found to be anisotropic. It was also concluded that the use of unconfined compressive testing is not the best approach for the measurement of the elastic properties of coal and other sedimentary rocks.

Table 6: Triaxial test data showing the anisotropy and stress-dependence of a Queensland coal.

Vertical Stress (MPa)	Horizontal Stress (MPa)	Vertical Young's Modulus E_1 (GPa)	Vertical Poisson's Ratio ν_{12} (-)	Vertical Stress (MPa)	Horizontal Stress (MPa)	Horizontal Young's Modulus E_2 (GPa)	Horizontal Poisson's Ratio ν_{21} (-)
2.17	0.07	0.46	0.18	2.15	1.80	0.78	0.12
4.20	1.83	1.67	0.13	4.18	3.61	2.20	0.17
6.21	3.67	2.47	0.17	6.26	5.40	3.00	0.23
8.23	5.49	2.93	0.21	8.25	7.21	3.52	0.25
10.24	7.33	3.22	0.24	10.27	9.01	3.86	0.24
12.26	9.12	3.53	0.25	12.28	10.81	4.00	0.26
14.31	10.91	3.50	0.25	14.33	12.61	4.17	0.27
16.30	12.71	3.71	0.27	16.33	14.42	4.34	0.29
18.44	14.54	3.78	0.28	18.46	16.25	4.43	0.29

Data sourced from Gray et al. (2019)

8.2 Elastic properties: Compressibility

The coefficient of volume compressibility, C_m, is calculated from the Young's modulus and Poisson's ratio under the assumption of uniaxial strain (e.g. Figure 32(b)), as per Equation 10. It can also be estimated in-situ, given the relationship between specific storage, formation compressibility, and porosity (see Section 5.1). The evaluation of compressibility is necessary for analytical modelling of one-dimensional compaction, however it is intrinsic in linear elastic numerical models that are subjected to uniaxial strain constraints.

The data for vertical Young's modulus and Poisson's ratio from Table 6 can be used with Equation 31 to highlight the effect of varying elastic properties on compressibility. Figure 33(a) plots the calculated values against vertical stress, which can be interpreted here as a proxy for depth of burial. Note that the first data pair has been excluded from this plot as it would correspond to a depth of approximately 80 m, which is shallower than coal seams typically

targeted for CSG production. It can be seen in the graph that the calculated compressibility decreases by a factor of nearly three over this range, which would significantly alter compaction estimates.

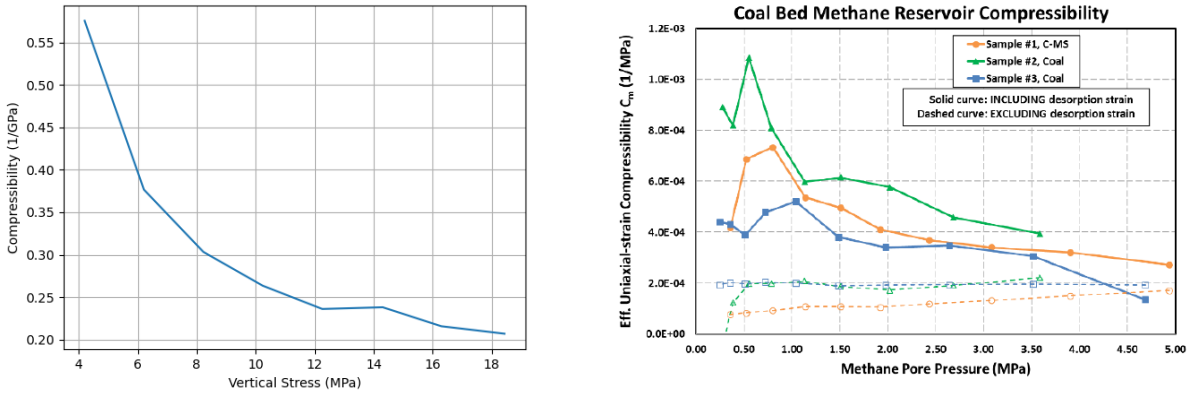

(a) *(b)*

Figure 33: Graphs of coal compressibility, showing (a) the variation in compressibility that stems from the stress dependent interpretation of Young's modulus and Poisson's ratio in Gray et al. (2019), and (b) the variation in compressibility as a function of pore pressure when desorption-induced shrinkage is accounted for (reproduced from Dudley et al. (2019)).

Attempts have recently been made (Coffey Services Australia, 2021) to estimate compressibility of geological units in the Surat Basin using InSAR measurements of subsidence (i.e. compaction) and observed drawdown. This assumed that all measured subsidence was attributed to the compaction of the geological units that comprise the Walloon Coal Measures, and that outside these there was negligible depressurisation. The thickness of units was informed by the OGIA groundwater model and Poisson's ratio was assumed to be 0.25. Via inverse analysis, this resulted in Young's modulus estimates of 4.2 GPa and 23.2 GPa for the Taroom and Juandah Coal Measures, respectively. The former corresponded well with the data from UCS tests summarised in Table 4 but the latter was recognised to be improbably high.

8.3 Hydraulic conductivity, permeability, and porosity

Hydraulic conductivity quantifies the ease of water flow through a porous medium. This quantity can vary by many orders of magnitude (e.g. between sands and clays), and for sedimentary rocks it can be anisotropic. Due to bedding, hydraulic conductivity can end up being larger in the horizontal direction than the vertical direction. As an example of its variability, the hydraulic conductivity in the Condamine alluvium can vary between 1.9 m/day and 40 m/day. The 2019 UWIR (OGIA, 2019) provides a summary of calibrated horizontal and vertical hydraulic conductivities for a number of geological units in the Surat Basin, and a subset of these data (median, 5th percentile, 95th percentile) has been reproduced in Table 7. The vertical conductivity in these data is typically three orders of magnitude smaller than the horizontal conductivity.

Hydraulic conductivity, K, is linked to intrinsic permeability, k, which is a property of the porous medium and independent of the fluid, via,

$$K = \frac{k\rho g}{\mu}, \quad (22)$$

where ρ is the fluid density, g is gravitational acceleration, and μ is the dynamic viscosity of the fluid. Intrinsic permeability is used as the basis for many relative permeability models, which determine the permeability to different fluids (e.g. water and gas) as the fraction of each fluid within a porous medium varies. Uncertainty in relative permeability, and how it is upscaled to a simulator cell or element, propagates through to the prediction of gas and water production.

Porosity is commonly estimated from well log correlations as this approach enables estimation over the whole depth of a well compared to laboratory testing of samples (e.g. porosimetry or computed tomographic imaging). As an

alternative, formation permeability can be estimated in-situ using techniques such as slug tests, pumping tests, response to mechanical loading, and analysis of natural pore-pressure fluctuations (van der Kamp, 2001). Examples of the application of these techniques are widespread in the literature (e.g. Rau et al. (2022)).

Table 7: Calibrated horizontal and vertical hydraulic conductivity (median, 5th percentile, 95th percentile) of selected geological units (as modelled by OGIA) in the Surat Basin.

Hydrogeological Unit	Horizontal Hydraulic Conductivity (m/d)	Vertical Hydraulic Conductivity (m/d)
Gubberamunda Sandstone	2.23e-01 (5.00e-02 - 3.53e+00)	8.23e-05 (1.69e-05 – 1.31e-03)
Westbourne Formation	3.02e-04 (1.40e-04 – 1.02e-03)	3.14e- 07 (1.15e-07 – 1.20e-06)
Upper Springbok Sandstone	3.61e-04 (1.63e-04 - 4.46e-03)	1.40e-07 (5.07e-08 – 1.45e-06)
Lower Springbok Sandstone	5.85e-04 (3.34e-04 - 2.45e-03)	2.36e-06 (6.44e-07 – 2.33e-05)
Walloon Coal Measures NPZ	1.61e-04 (3.49e-07 - 8.19e-02)	2.05e-06 (6.18e-08 – 3.70e-04)
Upper Walloon Coal Measures	1.20e-04 (1.36e-05 - 1.95e-02)	5.78e-08 (1.17e-08 – 1.00e-06)
Middle 1 Walloon Coal Measures	6.34e-05 (2.50e-06 - 1.10e-02)	1.06e-08 (4.06e-09 – 2.56e-07)
Middle 2 Walloon Coal Measures	7.48e-05 (2.55e-06 - 1.32e-02)	1.17e-08 (4.19e-09 – 2.94e-07)
Middle 3 Walloon Coal Measures	9.77e-05 (2.63e-06 - 1.61e-02)	1.31e-08 (4.30e-09 – 3.94e-07)
Lower Walloon Coal Measures	1.01e-04 (1.41e-06 - 1.89e-02)	5.28e-09 (1.92e-09 – 6.44e-08)
Durabilla Formation	4.52e-05 (2.44e-05 - 1.31e-04)	2.33e-08 (8.43e-09 – 1.45e-07)
Upper Hutton Sandstone	3.32e-02 (1.08e-02 - 4.64e-01)	3.68e-06 (1.09e-06 – 1.08e-05)
Lower Hutton Sandstone	9.28e-03 (3.00e-03 - 4.70e-02)	1.00e-06 (2.60e-07 – 1.00e-06)
Upper Evergreen Formation	5.96e-05 (2.74e-05 - 1.73e-04)	1.62e-08 (6.12e-09 – 7.67e-08)
Boxvale Sandstone	3.11e-04 (1.54e-04 - 3.64e-03)	7.62e-08 (3.41e-08 – 1.00e-06)
Lower Evergreen Formation	6.27e-05 (2.66e-05 - 2.10e-04)	1.73e-08 (5.90e-09 – 1.11e-07)
Precipice Sandstone	7.47e-01 (5.00e-02 - 1.42e+01)	5.70e-04 (1.67e-05 – 1.24e-03)

Data sourced from OGIA (2019)

8.4 Langmuir properties

The incorporation of desorption-induced coal shrinkage in estimates of compaction and subsidence requires Langmuir properties of the coal. Whilst many adsorption isotherms are publicly available, it is not usual that they

contain the parameters relevant to shrinkage (i.e. Langmuir constant, b_L, and maximum volumetric swelling strain, ε_L^s). This is possibly due to the close relationship between these data and the constants that define the sorption isotherm of a coal, which is itself a measure of gas content (at a specific temperature and over a range of pressures) and thus a proxy for the economics of a field.

Connell et al. (2016) presented data for seven coal samples from the Bowen Basin which were taken from a range of depths between approximately 100 m and 600 m. Values for Langmuir and elastic properties are summarised in Table 8. It can be seen that the Poisson's ratio data are similar to those at maximum confining stress in Table 6, but the Young's modulus data are generally lower. Amongst other things, this study also presented correlations for the sorption strain with respect to gas content, and ε_L^s with respect to Langmuir volume.

Liu et al. (2017) conducted swelling experiments on small (4 mm) cylinders of medium volatile bituminous coal using methane at 40°C and pressures up to 40 MPa. The data were used to calibrate models of gas diffusion and matrix swelling and showed that gas transport, adsorption/desorption, and time-dependent swelling/shrinking are controlled by the diffusion of free molecules and exhibit dependence on the state of stress.

The work of Dudley et al. (2019) presents the results of methane pore pressure depletion tests under approximate uniaxial strain and in situ stress conditions on whole core coal samples from a Queensland CSG reservoir (no more specific information was provided). The results clearly showed the influence of desorption-induced shrinkage on the compressibility of the samples. As pore pressure decreases (i.e. increasing depletion), the compressibility was found to increase. This is analogous to the steepening of the Langmuir shrinkage curve at decreasing pore pressure. The compressibility as a function of pore pressure for three samples is shown in Figure 33(b). Data are presented both with and without desorption-induced shrinkage included. It can be seen that the results for the latter are largely independent of pore pressure. In describing the effect of shrinkage within a total compressibility coefficient, the data from this study could be applied in an iterative, analytical solution of uniaxial compaction. This is convenient from a computational efficiency point of view because the total compressibility coefficients could be included in large-scale models of compaction and subsidence based on one-dimensional consolidation theory.

Table 8: Langmuir shrinkage and elastic properties for seven coal samples from the Bowen Basin.

Sample	Maximum Swelling Strain ε_L^s (%)	Langmuir Constant P_{umax} (MPa)	Young's Modulus E (GPa)	Poisson's Ratio ν (-)
S1	1.13	5.06	3.771	0.279
S2	1.48	9.77	2.555	0.262
S3	1.28	4.73	3.517	0.320
S4	1.46	4.73	-	-
A1	1.55	6.51	2.278	0.298
A4	1.54	4.98	2.221	0.319
A5	1.21	6.93	2.645	0.284

Data sourced from Connell et al. (2016)

9. Prediction of CSG-Induced Subsidence

The depressurisation of coal seams is a key driver of both CSG production and CSG-induced subsidence. However, the route to effective depressurisation is complex and dependent on a number of interlinked physical processes, as discussed in Section 3. These complex relationships were also represented diagrammatically in Figure 10, which showed that coal permeability plays a fundamental role in gas and water flow. The extraction of these fluids from the subsurface results in formation depressurisation, which facilitates methane desorption and subsequent coal shrinkage. The methane liberated by desorption feeds back to the two-phase flow system, while formation depressurisation and coal shrinkage feed back to the coal permeability. The combination of depressurisation and shrinkage results in formation compaction which, after some attenuation by the overburden, is transmitted to the surface as subsidence. A further complication is that most of these processes vary with depth and coal type. There also exists significant variability in the stratigraphy throughout the Surat Basin, in particular, and interpolation of the stratigraphy between well locations is subject to a high degree of uncertainty. When attempting to predict CSG-induced subsidence it is, therefore, pertinent to consider how much of this detail is necessary and at what level of precision it should be included in the analysis.

A number of different approaches for predicting subsidence were discussed in Section 7, with the most appropriate technique dependent on the desired level of detail and the quality of the available input data. In this section, past subsidence predictions related to CSG production are compared and their differences discussed in the context of analysis choices. This review is then extended by using a synthetic case study to explore the influence of key parameter choices and assumptions on subsidence predictions using two different analysis techniques.

Depending on the scale, tools, data, and experience available, different analysts will approach the prediction of subsidence differently. However, if the key stratigraphic features are captured, material properties are well characterised, and appropriate assumptions are made, then this should not result in subsidence magnitudes that are too dissimilar.

9.1 Subsidence predictions related to Australian CSG production

Numerous predictions of CSG-induced subsidence have been made as the industry has progressed through the processes of environmental approval (e.g. Water Monitoring and Management Plans), field evaluation, and ongoing monitoring and compliance (e.g. Underground Water Impact Reports). These vary in their level of technical complexity, scale, and parameter assumptions. A summary of these most recent predictions is included in Table 9.

A wide range of subsidence magnitudes can be seen in the data summarised in Table 9. Some difference in these predictions is to be expected because each of the four operators listed produce gas from different locations within the Surat and Bowen Basins, where there are differences in the lithology (e.g. coal seam thickness and continuity, depth of overburden), reservoir properties (e.g. pressure and permeability distribution), and mechanical properties of each geological unit (e.g. Young's modulus, Poisson's ratio). However, the differences in assumptions, input data, and approach to analysis will also have contributed to the variability in the estimates.

One of the most significant inputs to the prediction of compaction and subsidence is the final pressure distribution in the subsurface. This is best demonstrated by APLNG (2014), whereby the change from internal groundwater modelling to that in the 2012 UWIR reduced the maximum predicted subsidence from 900 mm to 500 mm. Based on observations since the commencement of production, these have both been demonstrated to be significant overpredictions, which is also attributable to the use of a simple compaction formula based on storage coefficient. Similarly, Golder Associates (2010) combined single-phase groundwater modelling with one-dimensional elastic

deformation (i.e. not the more conventional assumption of uniaxial strain) to predict subsidence. This work assumed that all 300 m of the coal measures (i.e. inclusive of all interburden) was depressurised during production, which again resulted in overestimation of compaction and subsidence.

Table 9 A summary of subsidence modelling predictions by CSG operators in Queensland.

Company	Year	Prediction(s)	Comments
QGC Shell (Golder Associates, 2010)	2012	Subsidence of 80 mm, 145 mm and 180 mm in the central, southeast, and northwest development areas, respectively.	Single-phase groundwater modelling was used to inform an analytical subsidence model based on one-dimensional linear elasticity. Coal shrinkage was not incorporated.
Santos (Santos, 2013)	2013	Subsidence of 280 mm near Roma and 150 mm at the Arcadia and Fairview fields.	Linear elastic theory (no further information could be found).
Australia Pacific LNG (APLNG, 2014)	2014	Subsidence of 900 mm in high-risk areas and less than 50 mm in low-risk areas, with the maximum value reducing to 500 mm when using OGIA's pressure data.	A simple compaction formula based on storage coefficient and change in pressure head was coupled to a numerical groundwater model (and the 2012 UWIR groundwater model for comparison). Coal shrinkage was not incorporated.
QGC Shell (Jacobs, 2016)	2016	Subsidence up to 370 mm at the Kenya, Kenya East, Kate, Owen, and Jammat fields (Central) and Kathleen, Arthur, Philip, Cameron, and Polaris (Northern) fields. Results averaged over the 8 km × 8 km tenement scale.	Depressurisation predictions from the 2016 UWIR (OGIA, 2016b) were used to inform axial compaction calculations (without assuming uniaxial strain). The key input, E, was estimated by combining information from laboratory tests, wellbore logs, and the literature. Coal shrinkage was not incorporated.
Arrow Energy (Coffey Environments, 2018)	2018	Upper-bound subsidence of up to 100 mm by 2050 at the Daandine field when considering Arrow operations only, which increases to 120 mm when considering adjacent operations.	Depressurisation predictions from the 2016 UWIR (OGIA, 2016b) were used to inform uniaxial elastic compaction. One of the key inputs, E' , was evaluated from measured subsidence (InSAR) and pressure drawdown. An average shrinkage strain was applied to coal seams.
QGC Shell (Rai & Hummel, 2019)	2019	Upper-bound subsidence of up to 200 mm (P50) or 250 mm (P90) by 2060 at the Lauren and Codie field in the southern part of the Central Development Area (CDA).	Depressurisation predictions from reservoir simulation of the CDA used to inform a 3D finite element model of compaction and subsidence. Numerical results complemented by uniaxial compaction estimates. The coal compressibility, C_m, due to poroelasticity and shrinkage was determined experimentally.
OGIA (OGIA, 2021)	2022	Maximum (P50) subsidence of 150 mm south of Miles and north of Cecil Plains. Highly localised predictions of 175 mm. Most locations predicted to undergo less than 100 mm of subsidence.	Depressurisation predictions from the 2021 UWIR (OGIA, 2021) used to inform 3D finite element modelling and large-scale uniaxial compaction. InSAR data were used to constrain compressibility parameters. The method used to represent coal shrinkage was not documented.

Data sourced from various industry reports

The comparison of these predictions is further complicated by the fact that only Coffey Environments (2018) and Rai and Hummel (2019) have directly accounted for desorption-induced coal shrinkage, which would add to the total amount of subsidence predicted. However, these more recent analyses have benefitted from the continued evolution of stratigraphic understanding in the Surat and Bowen Basins and the continuous improvement of reservoir simulations (e.g. that undertaken by OGIA in each successive UWIR, see below). In combination, these have resulted in more precise subsurface pressure predictions which in turn result in lower predictions of poroelastic compaction.

As discussed in Section 6.4, OGIA is required to report on the potential for subsidence impacts in its triennial UWIR process. The latest UWIR (OGIA, 2021) included large-scale predictive modelling of subsidence based on analytical and numerical techniques. A three-dimensional finite element model was built using the Visage™ geomechanical analysis package from Schlumberger. The model was 130 km long and 50 km wide and oriented northwest-southeast over the towns of Cecil Plains, Dalby, and Chinchilla A total of 88 vertical layers were included with a cell size that ranged from 250 m × 250 m to 750 m × 750 m. The necessary geomechanical properties of each layer were calculated from sonic logs of the wells within the model domain. The subsurface pressure distribution applied to the geomechanical model was derived from the UWIR's updated groundwater model. The method used to represent coal shrinkage was not documented.

The application of finite element methods to the entire Surat CMA is not computationally tractable. To facilitate subsidence predictions at this scale, an analytical model based on uniaxial compaction was also constructed. Comparison of the analytical and numerical model results showed good correspondence of subsidence predictions. This provided the necessary confidence to apply the analytical model in stochastic analysis and history matching. A total of 1,000 realisations were analysed with the best 50, based on comparison to InSAR measurements of the same area, used in the assessment of subsidence and change in slope.

The large-scale analytical subsidence predictions showed a maximum (P50) of 150 mm in locations south of Miles and north of Cecil Plains. Highly localised predictions of 175 mm were also seen at the latter, but in general most locations were predicted to undergo less than 100 mm of subsidence. In terms of slope, which is of particular importance in areas were flood irrigation is used, the results indicate a small region north of Cecil Plains where there is an approximately 80% probability of a 0.005% (i.e. 50 mm over 1 km) change in slope. This is attributed to the difference in depressurisation that occurs either side of the Horrane Fault in that location. In general, however, most locations were predicted to see a change in slope of 0.001%.

Interpretation of the modelling results was used to conclude that subsidence is dominated by linear elastic compaction of the Walloon Coal Measures, the rate of subsidence is highest early in development (i.e. during initial dewatering), and that there is negligible arching of overburden to reduce the ratio between compaction of geological units and subsidence at the surface. The latter conclusion is supported by geomechanical modelling commissioned by QGC Shell (Rai & Hummel, 2019). However, the influence of desorption-induced shrinkage on the first two conclusions warrants further investigation. The characteristic shape of the Langmuir shrinkage strain curve suggests that the rate of shrinkage may increase with continued depletion (but not necessarily time), as has been observed in InSAR analysis undertaken by industry (Rai & Hummel, 2019).

9.2 Surat Basin: Synthetic case study

The comparison of past subsidence predictions highlighted the sensitivity of results to the depressurisation field and the approach to calculating compaction as a function of pressure change. Assumptions related to the extent of vertical depressurisation within the Walloon Coal Measures (i.e. how many of the non-coal geological units were depressurised and to what degree) were also shown to significantly affect the magnitude of predicted subsidence. One of the points discussed in Section 7 was that, in general, one-dimensional consolidation models are straightforward to apply but might yield overestimates of subsidence. Conversely, three-dimensional numerical

analysis is too computationally and parameter intensive to be applied at the basin-scale. Even sub-models of part of a single CSG tenement can become computationally intractable when sensitivity analyses are required (i.e. a number of repeat calculations). Therefore, the choice of analysis technique is a function of scale (i.e. single or multiple wells, entire field or basin), the amount of stratigraphic detail to be included, and the availability of data with which to parameterise a high-fidelity model.

Another factor in the prediction of subsidence is the variability of the key parameters, including permeability, Young's modulus, Poisson's ratio, Langmuir isotherm, and associated shrinkage behaviour. As highlighted in Section 8, some parameters can vary by orders of magnitude and exhibit little correlation with vertical or lateral proximity. This challenge can be partially overcome by stochastic analysis, in which a distribution of key inputs is used (as opposed to a single value) to generate a distribution of outputs, highlight sensitivity to different parameters, and help quantify uncertainty.

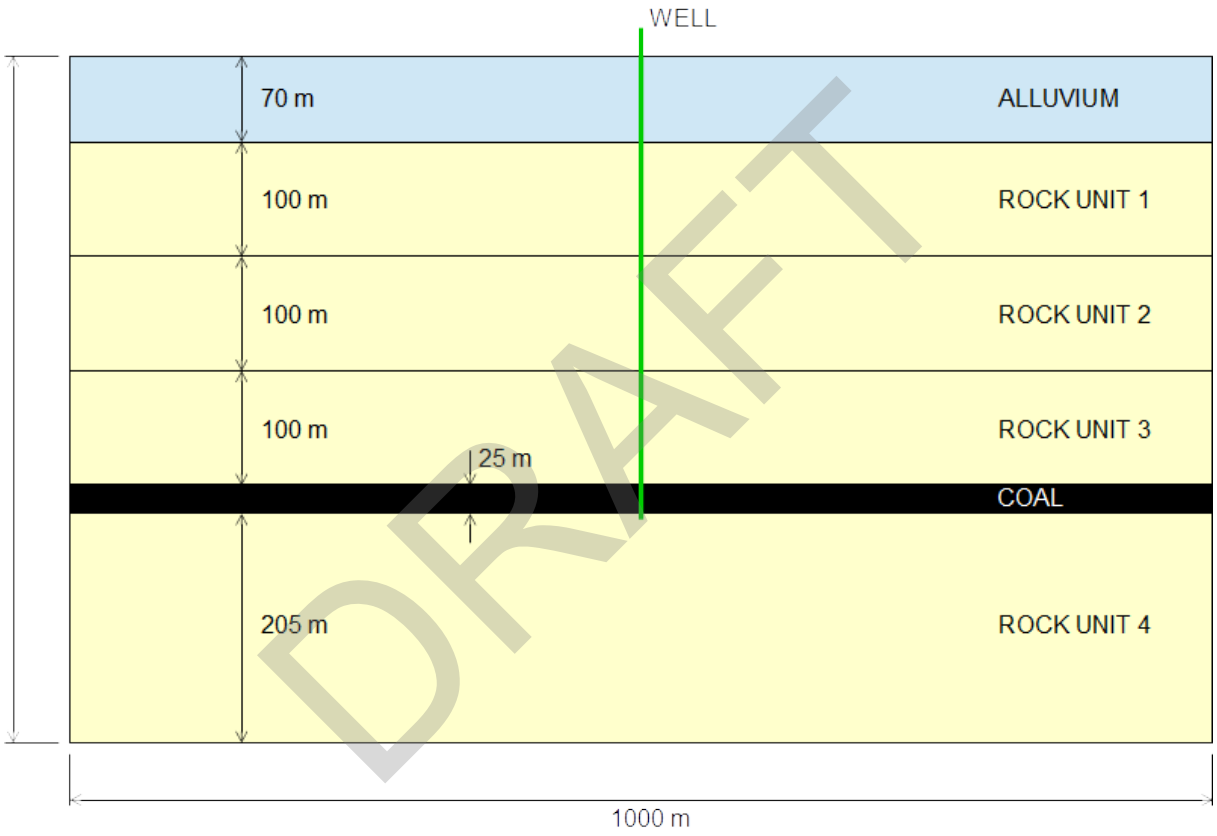

Figure 34: Schematic representation of the stratigraphy used in the subsidence case study.

At the request of the IESC, a case study was developed to demonstrate how the various forms of complexity might be simplified to result in a tractable numerical model of subsidence around a single CSG well and also compare the predictions of two different numerical approaches. The case study is based on a synthetic Surat Basin well that is targeting the Walloon Coal Measures. It is not designed to replicate any particular location and should be interpreted as such. It was assumed that the multiple coal seams across the WCM could be collapsed into a single, 25 m-thick coal layer (see Figure 34), which has good hydraulic connectivity with the well, where the target bottom hole pressure was 300 kPa. The initial pore pressure profile was assumed to be hydrostatic from the ground surface. Material properties representative of the WCM were chosen and are summarised in Table 10. The overburden (i.e. three rock units) and underburden (i.e. one rock unit) were assumed to have low permeability and thus not prone to significant depressurisation. Note that this configuration has excluded the interburden that would exist between the aggregated coal seams and be prone to some degree of depressurisation. The simplified stratigraphy and low permeability of the overburden and underburden used in this case study mean that depressurisation is primarily confined to the coal.

This is in contrast to the earlier predictions of Best et al. (2014), which assumed that all approximately 300 m of the Walloon Coal Measures are depressurised and, as such, represented an upper-bound, conservative estimate of total compaction and subsidence.

The two modelling platforms used in this comparison were COMSOL Multiphysics and CMG-GEM. COMSOL is a generalised platform for finite element discretisation and analysis of partial differential equations related to solid mechanics, fluid mechanics, and other multiphysics problems. GEM, on the other hand, is an advanced equation-of-state (EOS) compositional and unconventional reservoir simulator, which also includes a geomechanics module. GEM is part of a suite of tools typically applied in reservoir engineering.

Table 10: Material parameters used in the subsidence case study.

Property	Value	Property	Value
Coal properties		**Rock unit properties**	
Young's modulus, E	2 GPa	Young's modulus, E_{RU1}	4 GPa
Poisson's ratio, ν	0.40	Young's modulus, E_{RU2}	5 GPa
Fracture porosity, ϕ_0	0.01	Young's modulus, E_{RU3}	6 GPa
Initial permeability, k_0	100 mD	Young's modulus, E_{RU4}	8 GPa
Biot coefficient, α	1.0	Poisson's ratio, ν	0.25
Fracture compressibility, c_f	0.0002 kPa^{-1}	Fracture porosity, ϕ_0	0.20
Density, ρ	1,500 kg/m^3	Permeability, k_0	0.0001 mD
Maximum swelling strain, $\varepsilon_L{}^s$	0.013	Biot coefficient, α	1.0
Langmuir's constant, b_L	0.33 MPa^{-1}	Density, ρ	2,500 kg/m^3
Alluvium Properties		**Modified Rock Unit Properties**	
Young's modulus, E	0.2 GPa	Young's modulus, E_{RU1}	6 GPa
Poisson's ratio, ν	0.2	Young's modulus, E_{RU2}	8 GPa
Permeability, k_0	1 mD	Young's modulus, E_{RU3}	10 GPa
Density, ρ	2,000 kg/m^3	Young's modulus, E_{RU4}	20 GPa

The COMSOL model used an axisymmetric geometry around a single well, effectively resulting in a cylindrical domain. It included linear elastic solid mechanics, the Richard's (Richards, 1931) and van Genuchten (van Genuchten, 1980) equations for the transport of water in an unsaturated medium (the other phase is gas), stress-dependent permeability (i.e. dynamic permeability) based on the Cui-Bustin model (Cui & Bustin, 2005) listed in Equation 4, and shrinkage modelled analogously to thermal strain using Equation 12 in the solid mechanics

model. The van Genuchten equation was calibrated to include the pressure-saturation data that was output from the GEM reservoir simulator. In terms of the modelling of flow, this approach is similar to that applied by OGIA (Herckenrath et al., 2015).

The GEM model used a three-dimensional, prismatic domain with the single well in the centre. It models the conservation of mass and momentum for multiple fluid phases in a reservoir and is iteratively couped to a linear elastic solid mechanics module. The pressure-dependent Palmer-Mansoori model (Palmer & Mansoori, 1998) was used to update the coal permeability as a function of drawdown.

Five different analyses were undertaken to contrast the sensitivity of predictions to methodology, coal seam permeability, overburden strength, and coal shrinkage. This is not intended to represent an exhaustive parameter study or sensitivity analysis, but rather an illustration of how results change with inputs. The input parameters used for this case study are summarised in Table 10, and the five analysis scenarios are listed as follows.

0. One-dimensional compaction based on uniaxial strain;
1. Poroelastic with two phases modelled and static coal permeability;
2. Poroelastic with two phases modelled and dynamic coal permeability;
3. Poroelastic with two phases modelled, dynamic coal permeability, and 'strong' overburden;
4. Poroelastic with two phases modelled, dynamic coal permeability, and isotropic coal shrinkage.

The result for Case 0 can be calculated using Equation 11 and the average pressure drop in the coal layer, 3.45 MPa, the coal's uniaxial compressibility, 0.233 GPa^{-1}, the coal layer thickness, 25 m, and assuming that the coal's Biot coefficient is 1.0 (as is common in practice and in the absence of data to justify another value). This results in a coal layer compaction of 20.3 mm, which will be used as a basis for comparison for Cases 1 to 4. It is important to note that this value does not include any potential depressurisation of the rock units above or below the coal.

Figure 35 presents a number of graphs from the comparison of the COMSOL (left column) and GEM (right column) models for Cases 1 and 2. COMSOL exports data from the coordinates of finite element nodes whereas GEM exports averaged data from the centre of cells, meaning that the data presented herein are not sourced from exactly the same locations within the domain. However, this does not preclude meaningful comparison of the results from each model. Figure 35(a) and (b) plot the pressure profile with depth in the domain after 10, 20, and 30 years of drawdown for both Case 1 and 2 (i.e. static and dynamic permeability). The deviation from the initial hydrostatic profile is evident in both graphs, as is the propagation of pressure drop into the overburden and underburden as time progresses. The difference in data output is evident in these two graphs, as the GEM results do not show uniform depressurisation to 300 kPa of the coal layer at the well. However, some of this difference is a consequence of the different approaches to handling the gas and liquid phase in the models. Figure 35(c) and (d) plot the radial pressure profile in the coal with distance from the well, showing similar trends and pressure magnitudes from both models. In both COMSOL and GEM, the introduction of dynamic coal permeability reduced the magnitude of pressure drawdown in the coal layer. This is further explained in Figure 35(e) and (f), which plot the radial variation of coal permeability with distance from the well and how it changes with time. Both models show similar trends in permeability reduction as production (i.e. time) advances. In both modelling approaches, the use of a stress- (COMSOL) and pressure-dependent (GEM) permeability model has resulted in a decrease in spatial depressurisation due to the reduction of coal permeability with drawdown. It is evident from both analyses that the permeability of the coal seam, and how it changes during dewatering and gas production, is a key parameter in the prediction of subsurface pressure distribution and resulting subsidence.

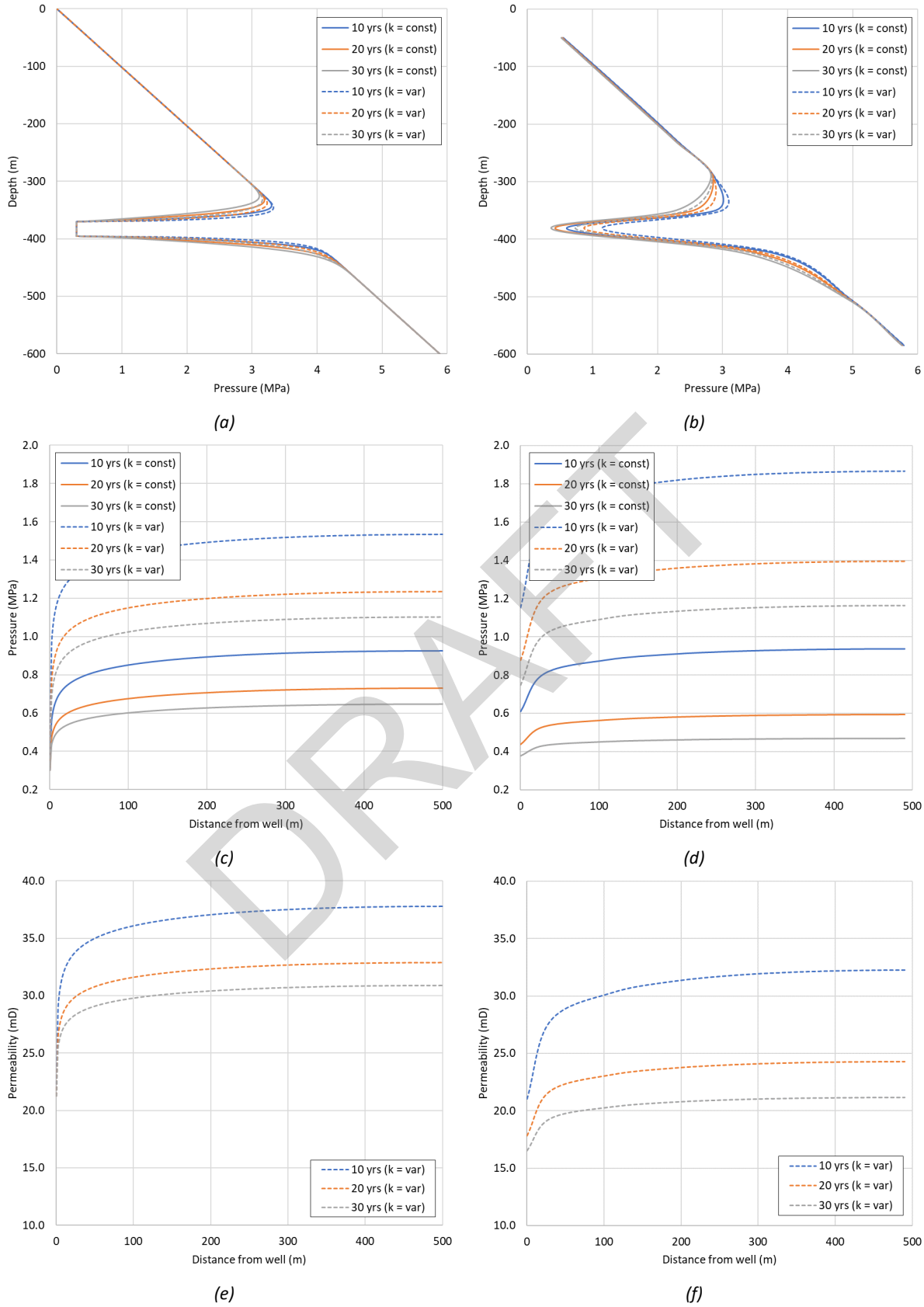

Figure 35: Results of the subsidence case study, showing graphs of (a, b) pressure profile with depth, (c, d) radial pressure profile in the coal with distance from the well, and (e, f) radial coal permeability with distance from the well. The left column (a, c, e) was produced with the COMSOL model, and the right column (b, d, f) was produced with the GEM model.

Figure 36(a) and (b) plot the cumulative compaction, or progressive subsidence, with depth in the domain for Case 1 (static permeability), Case 2 (dynamic permeability), and Case 3 (dynamic permeability and 'strong' overburden). After 30 years, the COMSOL model predicts 30 mm, 23 mm, and 20 mm subsidence above the well for each case, respectively. The reduced depressurisation caused by dynamic permeability change results in reduced subsidence, which is further reduced by the arching effect and reduction in compressibility when 'stronger' overburden is employed. All predictions are comparable to that calculated for Case 0, with the result for Case 3 almost identical to that calculated analytically. After 30 years, the GEM model predicts 34 mm, 27 mm, and 20 mm subsidence above the well for each case, respectively. The greater depressurisation predicted by GEM is borne out in greater subsidence magnitudes. However, the trend of subsidence reduction from Case 1, to Case 2, and then Case 3 is the same as that predicted by COMSOL. Figure 36(c) and (d) plot the subsidence at the surface with distance from the well. Both results show effectively uniform subsidence, with no more than 2 mm difference between the location of the well and the model boundary. They also clearly show the similarity in predictions between the two modelling approaches. The absence of pronounced cones of subsidence around the well is representative of the surface movement observed in InSAR data adjacent to CSG wells.

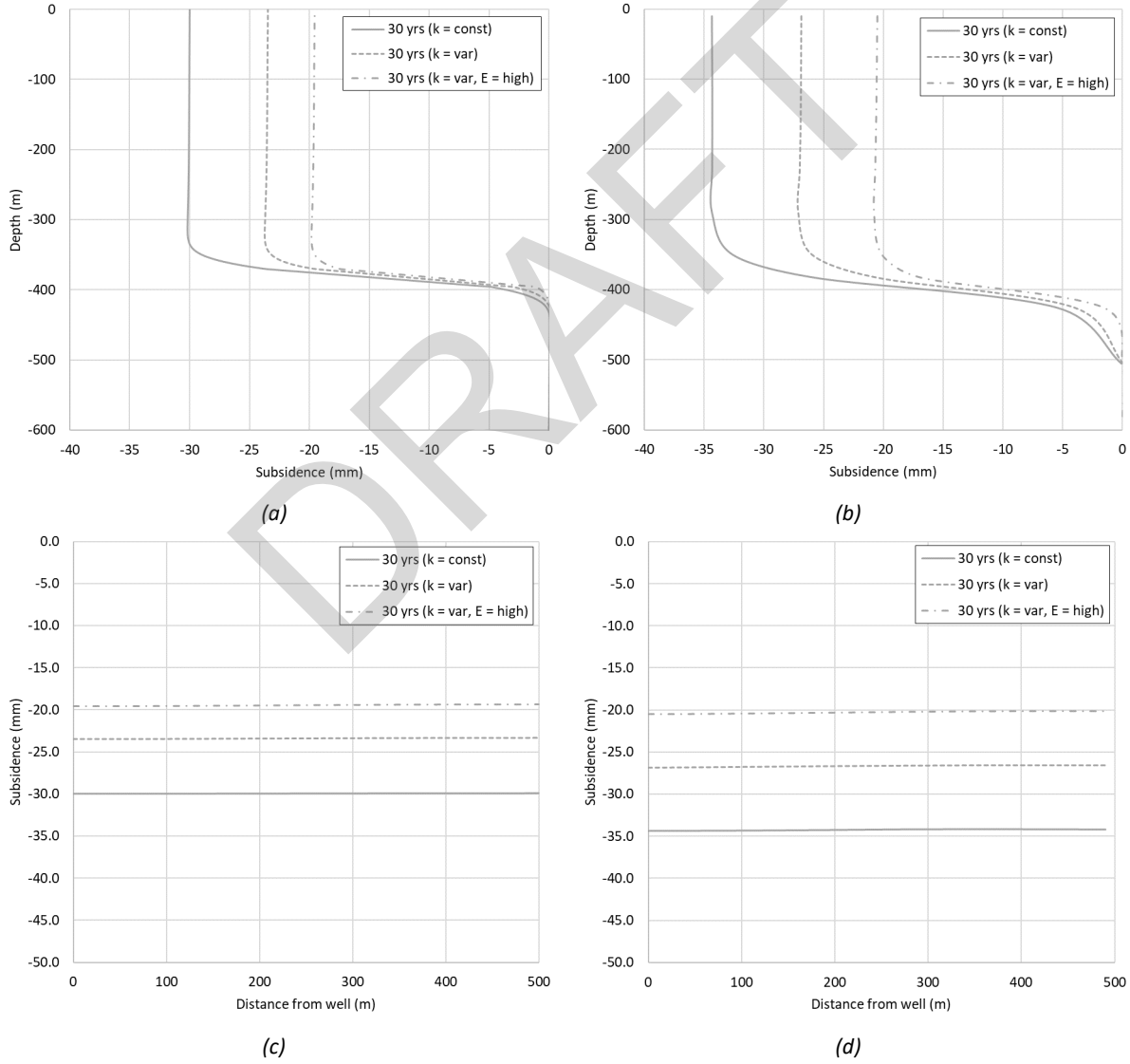

Figure 36: Results of the subsidence case study, showing graphs of (a, b) subsidence with depth and (c, d) subsidence at the surface as a function of the distance from the well. The left column (a, c) was produced with the COMSOL model and the right column (b, d) was produced with the GEM model.

The influence of shrinkage on the COMSOL predictions of subsidence is shown in Figure 37(a) and (b). These graphs show approximately 115 mm of desorption-induced shrinkage within the coal layer, resulting in subsidence of 138 mm at the surface. It can also be seen that the rate of subsidence decreases significantly after approximately five years, regardless of whether or not shrinkage was included. These results are consistent with other predictions and some observations of subsidence in the Surat Basin, as reported by OGIA (2021), and provide evidence in support of the incorporation of shrinkage in analysis of CSG-induced subsidence. More widespread measurement of shrinkage strain, ε_L^s, from coals that are exploited for CSG, or might be in the future, would reduce uncertainty in predictions related to this key model parameter.

It is important to note the limitations in the approach to modelling desorption-induced shrinkage in this case study. The shrinkage strain defined by Equation 12 implies an immediate compaction and, therefore, subsidence response with change in pore pressure. In reality, though, change in gas adsorption pressure might not always occur synchronously with dewatering and pore pressure reduction. Reasons for this include the existence of coals in an undersaturated state or with low-conductivity connection to the source of depressurisation (i.e. the well), both of which would delay the temporal response of shrinkage. Further research into the time-dependent, rather than pressure-dependent, manifestation of desorption-induced coal shrinkage *in situ* is required.

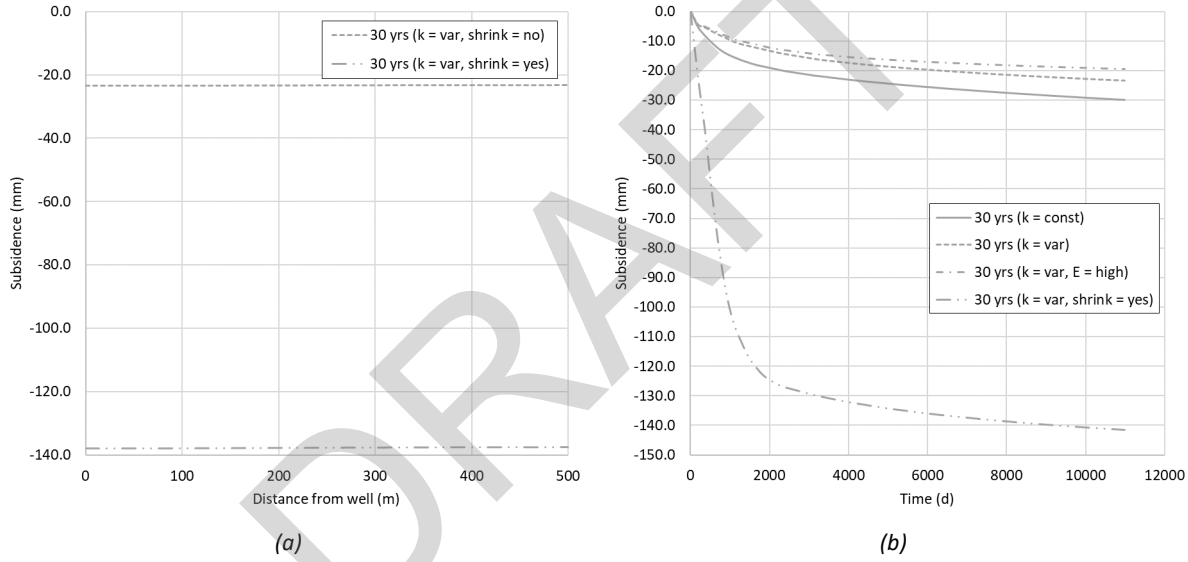

Figure 37: Results of the subsidence case study when coal shrinkage is included, showing graphs of (a) subsidence at the surface as a function of the distance from the well and (b) subsidence as a function of time for Case 1, 2, 3, and 4. These results were produced with COMSOL as desorption-induced shrinking and swelling is not available in the GEM geomechanics module.

10. Concluding Remarks

This explanatory note describes the subsurface flow and geomechanical processes by which CSG production induces subsidence, how the magnitude of CSG-induced subsidence can be predicted, and techniques for large-scale and high-precision monitoring of subsidence as it occurs. The information presented attempts to capture the state-of-the-art in relation to these issues, so that it may be used to guide best-practice in the assessment of CSG activities into the future. CSG-induced subsidence continues to be the focus of analysis, research, and development from academic, industrial, and regulatory perspectives, and these activities will contribute to greater understanding of the mechanics of CSG-induced subsidence, improved techniques for prediction and monitoring, and reduced uncertainty in the geometrical and material parameters that are input to analysis

10.1 Ongoing monitoring and assessment activity

Proposals for new CSG projects, such as the Narrabri Gas Project in NSW, are typically assessed at both State and Federal levels, including project-specific technical advice from the IESC. Experience from past and ongoing operations such as at Camden in NSW and in the Surat CMA, and the data that they generate, will help inform theses assessments. Several organisations are involved in the monitoring, analysis, and assessment of potential impacts of subsidence and surface movement. Some are focused on specific areas, whilst others work across NSW and Queensland. They include:

- The Queensland Office of Groundwater Impact Assessment (OGIA), who will continue to analyse groundwater and subsidence measurements and iteratively update history-matched predictions of future subsidence across the Surat CMA;
- Geoscience Australia (GA), who have deployed infrastructure including InSAR corner reflectors and GNSS stations to monitor surface movement in Camden in NSW and within the Surat CMA. GA are well-positioned to leverage this to provide large-scale assessment of surface movement in these locations and the nation more broadly;
- The GasFields Commission Queensland, who in 2022 partnered with OGIA to better understand the potential impacts and risks to farming operations resulting from CSG-induced subsidence, and how these impacts may be assessed and managed should they occur;
- CSG producers, who each have their own management and monitoring programs for subsidence and remote sensing (e.g. InSAR, LiDAR) of surface movement;
- The Centre for Natural Gas at The University of Queensland, who work directly with three large CSG operators in the Surat CMA to address areas of research need, one of which is subsidence and surface movement.

10.2 Future research requirements

Predictions of subsurface phenomena continue to be challenged by uncertainty surrounding the stratigraphy (i.e. what is down there, and where is it?), the properties of each geological unit (i.e. how do they behave from the perspectives of mechanics and fluid transport?), and the variability of these properties (i.e. what is an appropriate distribution?). In addition, as the continued collection of field data and improvements in analysis answer some of the outstanding questions related to CSG-induced subsidence, it can also raise new questions. A non-exhaustive list of future research opportunities is included as follows:

- Continued study of background (or baseline) trends of surface movement in non-production areas to assist with the separating of multiple contributions to net surface movement in areas of CSG production. This is particularly pertinent as recent climatic changes (i.e. the switch from an extended period of below-average rainfall to above-average rainfall) may manifest in observations such as changes to the long-term trends observed in the Surat CMA. The ability to better isolate the contribution of CSG-induced subsidence to observed surface movement would also facilitate inverse analysis of InSAR data aimed at, for example, quantifying reservoir depletion or history-matching reservoir properties;
- Further investigation of remote sensing tools (i.e. InSAR, GNSS, and LiDAR) for surface movement measurement, including their respective strengths and limitations in the parts of Australia where they are required, and how they can be combined to result in a comprehensive monitoring strategy;
- Continued improvement in the description of the subsurface, including a better description of sequence stratigraphy and statistics on the correlation of strata between wells (as informed by data from logs). This would help inform the assumptions made in upscaling and simplifying the stratigraphy used in predictions of depressurisation and CSG-induced subsidence. It would also improve the statistical description of lithology and parameter distribution in stochastic analysis, such as that discussed in Section 7.4;
- Investigation of the influence of faults on subsidence and differential surface movement via the inclusion of discontinuities in geomechanical analysis. This would be of benefit where specific faults could influence surface gradient as the surrounding strata compact and subside. This would also be useful in studying the effect of coal seam, and therefore pressure, dislocation where faults act as a barrier to fluid flow;
- Investigation of how permeability, and particularly relative permeability, is upscaled from a single cleat, to a coal block, coal seam, and then coal bearing unit. In addition, investigation of how the uncertainty associated with this scaling can be better quantified using advanced computational models. Recalling that coal permeability is the foundation of gas production and surface subsidence (see Figure 10), this has the potential to significantly improve subsidence predictions;
- Investigation of the transient nature of subsidence, recognising the cumulative impacts of poroelastic compaction (which should be greatest in the early stages of a well's life) and desorption-induced shrinkage (which might persist with the life of a well). One aspect of this could employ small- to intermediate-scale modelling of the compaction of cleated coal blocks where diffusive transport in the coal matrix is coupled to two-phase Darcy flow in the cleat network;
- Understanding of how anisotropy and the stress- and pressure-dependence of properties influence forward estimates of subsidence. Material properties of particular interest include the transverse isotropy of coal elastic and shrinkage properties, as well as the nonlinearity of the desorption-induced shrinkage of coal.

Glossary

This glossary is a modification of that published in Best et al. (2014).

Term	Description
Adsorption	The adhesion in an extremely thin layer of molecules (as of gases, solutes, or liquids) to the surfaces of solid bodies or liquids with which they are in contact.
Anisotropy	A term used to describe the directional dependence of a material property (e.g. vertical and horizontal permeability may be different).
Aquifer	A term used to refer to a water-bearing geological unit.
Aquitard	A relatively low-hydraulic conductivity geological unit.
Associated water	Water that exists naturally within coal seams and is generally rich in salts and other minerals.
Biot coefficient	The ratio of the volume of the fluid change divided by the change in bulk volume under the constraint that pore pressure remains constant.
Brine	Water from a deep geological formation that exhibits a high salt concentration.
Cleats	Cleats are fractures in coal created during coalification. They usually occur in two sets that are perpendicular to one another and perpendicular to bedding. The cleats in one direction form first and exhibit a high level of continuity. These are called 'face cleats'. Cleats in perpendicular to face cleats are called 'butt cleats'.
Coal measures	Geological formation comprised of thin-bedded, claystones, shales, siltstones, lithic and sublithic to feldspathic arenites, coal seams and partings and minor limestone.
Coal rank	A classification system that distinguishes the physical and chemical properties of different qualities of coal (from peat, through lignite and bituminous coal, to anthracite). Higher rank coals possess a higher sorptive capacity for methane gas, and tend to have higher carbon content, and decreased moisture content and volatile matter.
Coefficient of volume compressibility	A measure of the compressibility of a material.
Compaction	When used in a geological context, is the process by which geological strata under pressure reduce in thickness and porosity, and increase in density (see Compression).
Compressibility	A parameter that determines the potential for compaction. Compressibility is typically high for soft clays, intermediate for sands, low (but variable) for coals, very low for consolidated sedimentary rocks such as sandstones and mudstone, and extremely low for competent rocks such as granites and other intrusions.

Compression	A system of geomechanical forces or stresses that tend to decrease the volume or shorten a substance, or the change of volume produced by such a system of forces. In the context of this report, compression is a result of both the shrinkage of the coal due to gas desorbing from the coal matrix, and geomechanical compression due to depressurisations associated with gas and groundwater extraction.
Conventional	Conventional resources are concentrations of oil or gas that occur in discrete accumulations within rock formations that traditionally have high porosity and permeability and are found below impermeable rock formations. These resources are developed using vertical well bores and minimal stimulation.
Darcy's Law	A constitutive equation that describes the flow of a fluid through a porous medium (e.g. groundwater through an aquifer).
Depressurisation	Reduction in ground pressures due to the removal of groundwater.
Dewatering	The removal or draining of groundwater by pumping.
Drawdown	Groundwater drawdown is the fall in the groundwater pressure (or groundwater table) from a pre-existing level.
Dual porosity	A feature of soil/rock whereby fluids may be present within the open fractures (which possess a certain storage capacity or 'primary porosity') and within porous matrix blocks (which possess a different storage capacity or 'secondary porosity'). The secondary porosity is the principal conduit for flow and transport.
Elastic	The physical property of a material that returns to its original shape.
Fick's Law	Typically referring to Fick's first law, a mathematical law that describes diffusion (the movement of a substance from regions of high concentration to regions of low concentration).
Gas resource	Defined by the internationally recognised Petroleum Resources Management System (PRMS) as those quantities of gas which are estimated, on a given date, to be potentially recoverable from known accumulations, but which are not currently considered to be commercially recoverable.
Gas reserve	Defined by the PRMS as those quantities of petroleum which are anticipated to be commercially recovered from known accumulations from a given date forward.
Geological unit	A volume of soil or rock of identifiable geological origin and age that is defined by distinctive and recognisable mineral and textural detail, physical characteristics, and (potentially) fossil content.
Geomechanical	Relating to the mechanics (movement/compression/expansion) of soils or rock.
Gilgai	From the Australian Aboriginal word meaning 'small water hole', a small, ephemeral lake formed from a depression in the soil surface in expanding clay soils. Additionally, the term gilgai is used to refer to the overall micro-relief in such areas.
Guar	The legume from which guar gum is derived. Guar gum is a substance used to increase the viscosity of fluids.

Heterogeneous	A substance that is not uniform in composition or in a particular character.
Horizon	A geological bedding surface where there is a change in lithology, or a layer with a characteristic lithology within a sequence of layers.
Hydraulic conductivity	A measure of the rate or velocity of groundwater flow through a material (such as soil/rock).
Hydraulic fracturing	A technique used to increase the permeability of geological strata in the vicinity of a coal seam gas well by injecting a fluid slurry into a well under pressure.
Hydrogeological unit	A geological unit that bears groundwater.
Interbedded	Geological beds (rock layers) of one lithology lie in alternating layers with beds of another lithology.
Knudsen number	A dimensionless number defined as the ratio of the molecular mean free path length to a representative physical length scale (e.g. pore throat diameter), used to determine whether continuum mechanics or statistical mechanics should be used to model transport.
Laminar flow	A water flow regime characterised by the flow of parallel streamlines with no disruption (such as eddies, cross flow, swirling or pulsing flow) between these streamlines.
Langmuir isotherm	A physical relationship describing the mass or volume of a substance covering by adsorption to a solid surface in relation to gas pressure or substance concentration.
Lithology	A description/characterisation of the physical characteristics of a rock mass.
Matrix (rock matrix)	The finer grained mass of rock material in which larger grains/crystals are embedded.
Modelling, analytical	The use of closed-form mathematical solutions to directly to calculate, for example, subsidence as a function of material properties, boundary conditions, and loading.
Modelling, numerical	The use of numerical methods (e.g. finite element method) to discretise a set of governing equations (e.g. coupled fluid in and compaction of porous rocks) and solve them on a computer to calculate, for example, subsidence in situations that are too complex for analytical models.
Overburden	In coal seam gas/coal mining, the soil/rock that lies above the coal seam.
Permeability	The measure of the ability of a rock, soil or sediment to yield or transmit a fluid. The magnitude of permeability depends largely on the porosity and the interconnectivity of pores and spaces in the ground.
Poisson's ratio	In solid mechanics, the measure of deformation of a material perpendicular to the direction of loading. Typically varies between 0 and 0.5.
Pore (water) pressure	The pressure of groundwater held within a soil or rock, in the space (pores) between soil/rock particles.

Preferential flow	Preferential flow refers to the uneven and often rapid and short-circuiting movement of water and solutes through porous media (typically soil) characterised by small regions of enhanced flux (such as faults, fractures or high permeability pathways) which contributes most of the flow, allowing much faster transport of a range of contaminants through that pathway.
Recharge	Groundwater recharge is the process whereby surface water (such as from rainfall runoff) percolates through the ground to the water table.
Saturated flow	Flow through a porous medium (such as soil or rock) in which the void space within the porous medium is entirely occupied by water (as opposed to water and gas).
Sedimentary rock	Rock formed by deposition of material at the Earth's surface and within water bodies.
Settlement	The vertical, downward displacement of strata in response to compaction or removal of underlying strata.
Sorption	Physical/chemical process whereby one substance becomes attached to another.
Strain	A proportional change in length or volume of a mass.
Stratum	A layer of sedimentary rock or soil within distinctive characteristics that distinguish it from other layers (plural: strata).
Subsidence	Usually refers to vertical displacement of a point at or below the ground surface. However, the subsidence process actually includes both vertical and horizontal displacements. Subsidence is usually expressed in units of millimetres (mm) or metres (m).
Two-phase flow	Fluid flow characterised by the flow of two fluid phases (e.g. a liquid and a gas).
Unconventional	Unconventional resources are oil or gas-bearing units where the permeability and porosity are typically low and or the target hydrocarbons still exist within the host formation.
Unsaturated flow	Flow through a porous medium (such as soil or rock) in which the void space within the porous medium is occupied by both water and gas (rather than water only).
Upstream operations	In the context of oil and gas, this typically refers to activities related to exploration and extraction, as opposed to transport, refinery and other value-adding processes.
Vertosol	A vertosol is a soil type in which there is a high content of expansive clay minerals, many of them known as montmorillonite, that form deep cracks in drier seasons or years.
Well	Borehole in which casing (e.g. steel piping) has been placed to restrict connection to specific ground horizons/depths.
Well field	The area over which wells are distributed to extract groundwater and coal seam gas.
Young's modulus	A measure of the stiffness of an elastic material. Also known as the elastic modulus.

References

Acar Yalcin, B., & El-Tahir El-Tahir, A. (1986). Low Strain Dynamic Properties of Artificially Cemented Sand. *Journal of Geotechnical Engineering*, *112*(11), 1001-1015. https://doi.org/10.1061/(ASCE)0733-9410(1986)112:11(1001)

Acworth, R. I., Halloran, L. J. S., Rau, G. C., Cuthbert, M. O., & Bernardi, T. L. (2016). An objective frequency domain method for quantifying confined aquifer compressible storage using Earth and atmospheric tides. *Geophysical Research Letters*, *43*(22), 11,671-611,678. https://doi.org/10.1002/2016GL071328

AGL. (2022). *Camden Gas Project - Safely supplying our share of NSW's gas needs since 2001*. Retrieved 4 August from https://www.agl.com.au/about-agl/how-we-source-energy/camden-gas-project

Al-Arouri, K. R., McKirdy, D. M., & Boreham, C. J. (1998). Oil-source correlations as a tool in identifying the petroleum systems of the southern Taroom Trough, Australia. *Organic Geochemistry*, *29*(1), 713-734. https://doi.org/https://doi.org/10.1016/S0146-6380(98)00132-6

Ali, A., Merrick, N. P., Williams, R. M., Mampitiya, D., d'Hautefeuille, F., & Sinclair, P. (2004, 17-20th February, 2004). *Land settlement due to groundwater pumping in the Lower Namoi Valley of NSW* 9th Murray Darling Basin Groundwater Workshop, Bendigo, Victoria.

Allen, A. S. (1984). Types of land subsidence. *Studies and Reports in Hydrology*, *40*, 133-142.

Alley, W. M., Healy, R. W., LaBaugh, J. W., & Reilly, T. E. (2002). Flow and storage in groundwater systems. *Science*, *296*(5575), 1985-1990. https://doi.org/10.1126/science.1067123

Aminian, K. (2020). 4 - Gas storage in coal. In P. Thakur, S. J. Schatzel, K. Aminian, G. Rodvelt, M. H. Mosser, & J. S. D'Amico (Eds.), *Coal Bed Methane (Second Edition)* (pp. 115-131). Elsevier. https://doi.org/https://doi.org/10.1016/B978-0-12-815997-2.00004-4

APLNG. (2014). *Groundwater monitoring plan - Australia Pacific LNG upstream project* (Q-LNG-01-10-MP-0005).

Armstrong, R. T., Sun, C., Mostaghimi, P., Berg, S., Rücker, M., Luckham, P., Georgiadis, A., & McClure, J. E. (2021). Multiscale Characterization of Wettability in Porous Media. *Transport in Porous Media*, *140*(1), 215-240. https://doi.org/10.1007/s11242-021-01615-0

Arrow Energy. (2022). *Surat Gas Project - Updated CSG water monitoring and management plan.*

Auvray, R., Rosin-Paumier, S., Abdallah, A., & Masrouri, F. (2014). Quantification of soft soil cracking during suction cycles by image processing. *European Journal of Environmental and Civil Engineering*, *18*(1), 11-32. https://doi.org/10.1080/19648189.2013.840250

Bear, J., & Corapcioglu, M. Y. (1981). Mathematical model for regional land subsidence due to pumping: 2. Integrated aquifer subsidence equations for vertical and horizontal displacements. *Water Resources Research*, *17*(4), 947-958.

Bell, J. S. (2006). In-situ stress and coal bed methane potential in Western Canada. *Bulletin of Canadian Petroleum Geology*, *54*(3), 197-220. https://doi.org/10.2113/gscpgbull.54.3.197

Benedek, C., Majdik, A., Nagy, B., Rozsa, Z., & Sziranyi, T. (2021). Positioning and perception in LIDAR point clouds. *Digital Signal Processing*, *119*, 103193. https://doi.org/https://doi.org/10.1016/j.dsp.2021.103193

Berardino, P., Fornaro, G., Lanari, R., & Sansosti, E. (2002). A new algorithm for surface deformation monitoring based on small baseline differential SAR interferograms. *IEEE Transactions on Geoscience and Remote Sensing*, *40*(11), 2375-2383. https://doi.org/10.1109/TGRS.2002.803792

Best, R., Rotter, B., Orton, A., Geng, I., Zoorabadi, M., & Tammetta, P. (2014). *Monitoring and management of subsidence induced by coal seam gas extraction* [Report]. I. E. S. C. o. C. S. G. a. L. C. M. Development.

Bhutto, A. W., Bazmi, A. A., & Zahedi, G. (2013). Underground coal gasification: From fundamentals to applications. *Progress in Energy and Combustion Science*, *39*(1), 189-214. https://doi.org/https://doi.org/10.1016/j.pecs.2012.09.004

Biot, M. A. (1941). General theory of 3-dimensional consolidation. *Journal of Applied Physics*, *12*, 155-164.

Black, D. J., & Aziz, N. I. (2009). *Developments in coal mine methane drainage and utilisation in Australia* Ninth International Mine Ventilation Congress, Dhanbad, India.

Booker, J. R., & Carter, J. P. (1986). Analysis of a point sink embedded in a porous elastic half space [https://doi.org/10.1002/nag.1610100204]. *International Journal for Numerical and Analytical Methods in Geomechanics*, *10*(2), 137-150. https://doi.org/https://doi.org/10.1002/nag.1610100204

Booker, J. R., & Carter, J. P. (1987). Elastic consolidation around a point sink embedded in a half-space with anisotropic permeability [https://doi.org/10.1002/nag.1610110106]. *International Journal for Numerical and Analytical Methods in Geomechanics*, *11*(1), 61-77. https://doi.org/https://doi.org/10.1002/nag.1610110106

Borchers, J. W., & Carpenter, M. (2014). *Land subsidence from groundwater use in California.*

Bracegirdle, A., Mair, R. J., Nyren, R. J., & Taylor, R. N. (1996). *A methodology for evaluating potential damage to cast iron pipes induced by tunnelling* Technical Committee TC28 on Underground Construction in Soft Ground,

Briaud, J.-L., Zhang, X., & Moon, S. (2003). Shrink test-water content method for shrink and swell predictions. *Journal of Geotechnical and Geoenvironmental Engineering*, *129*(7), 590-600. https://doi.org/10.1061/(ASCE)1090-0241(2003)129:7(590)

Brown, N., Richardson, C., Neufeld, J., & Woods, A. (2014). *Constraining Surface Deformation Preditions Resulting from Coal Seam Gas Extraction*. Geoscience Australia.

Budhu, M., Ossai, R., & Adiyaman, I. (2014). Ground Movements from Aquifer Recharge and Recovery. *Journal of Hydrologic Engineering*, *19*(4), 790-799. <Go to ISI>://WOS:000332770400014

Burbey, T. J. (2001a). Stress-strain analyses for aquifer-system characterization. *Groundwater*, *39*(1), 128-136.

Burbey, T. J. (2001b). Storage coefficient revisited: Is purely vertical strain a good assumption? *Groundwater*, *39*(3), 458-464.

Burbey, T. J. (2002). The influence of faults in basin-fill deposits on land subsidence, Las Vegas Valley, Nevada, USA. *Hydrogeology Journal*, *10*(5), 525-538.

Burbey, T. J., & Helm, D. C. (1999). Modeling three-dimensional deformation in response to pumping of unconsolidated aquifers. *Environmental & Engineering Geoscience*(2), 199-212.

Busetti, S., & Flottmann, T. (2018). Modeling Hydraulic Fracturing in Transitional Stress Regimes, Surat Basin, Australia. 2nd International Discrete Fracture Network Engineering Conference,

Bustin, R. M. (1997). Importance of fabric and composition on the stress sensitivity of permeability in some coals, northern Sydney basin, Australia: Relevance to coalbed methane exploitation. *81, place = United States*(11). https://www.osti.gov/biblio/563428 , journal = AAPG Bulletin

Calderhead, A., Therrien, R., Rivera, A., Martel, R., & Garfias, J. (2011). Simulating pumping-induced regional land subsidence with the use of InSAR and field data in the Toluca Valley, Mexico. *Advances in Water Resources*, *34*(1), 83-97.

Candela, T., Chitu, A. G., Peters, E., Pluymaekers, M., Hegen, D., Koster, K., & Fokker, P. A. (2022). Subsidence Induced by Gas Extraction: A Data Assimilation Framework to Constrain the Driving Rock Compaction Process at Depth [Original Research]. *Frontiers in Earth Science*, *10*. https://doi.org/10.3389/feart.2022.713273

Cardwell, J. (2018). Dynamic Modelling of Walloon Coal Measures: An Unsavoury Cocktail of Reservoir Variability, Mismatched Resolutions, and Unreasonable Expectations. SPE Asia Pacific Oil and Gas Conference and Exhibition,

Case, J. C., Edgar, T. V., & De Briun, R. H. (2000). *Subsidence potential related to water withdrawal in the Powder River basin: Wyoming State*. G. S. Wyoming.

Cassiani, G., & Zocatelli, C. (1998). *Gas Extraction and Risk of Subsidence: the Case of the Northern Adriatic Gas Fields, Technical Issues* SPE International Conference on Health, Safety, and Environment in Oil and Gas Exploration and Production, https://doi.org/10.2118/46808-MS

Casu, F., Manzo, M., & Lanari, R. (2006). A quantitative assessment of the SBAS algorithm performance for surface deformation retrieval from DInSAR data. *Remote Sensing of Environment*, *102*(3), 195-210. https://doi.org/https://doi.org/10.1016/j.rse.2006.01.023

Chaussard, E., Wdowinski, S., Cabral-Cano, E., & Amelung, F. (2014). Land subsidence in central Mexico detected by ALOS InSAR time-series. *Remote Sensing of Environment*, *140*, 94-106. https://doi.org/https://doi.org/10.1016/j.rse.2013.08.038

Chen, J., Knight, R., Zebker, H. A., & Schreüder, W. A. (2016). Confined aquifer head measurements and storage properties in the San Luis Valley, Colorado, from spaceborne InSAR observations. *Water Resources Research*, *52*(5), 3623-3636. https://doi.org/10.1002/2015WR018466

Chen, Z. R. (2011). Poroelastic model for induced stresses and deformations in hydrocarbon and geothermal reservoirs. *Journal of Petroleum Science and Engineering*, *80*(1), 41-52. https://doi.org/https://doi.org/10.1016/j.petrol.2011.10.004

Clarkson, C. R., & Bustin, R. M. (1999). The effect of pore structure and gas pressure upon the transport properties of coal: a laboratory and modeling study. 2. Adsorption rate modeling. *Fuel*, *78*(11), 1345-1362. https://doi.org/https://doi.org/10.1016/S0016-2361(99)00056-3

Coffey Environments. (2018). *Surat gas project Stage 1 CSG Water monitoring and management program - Subsidence technical memorandum* (ENAUABTF20484AA).

Coffey Services Australia. (2021). *Surat gas project - Subsidence monitoring and prediction (prepared or Arrow Energy)* (Report Reference: 754-MELENP268280-AA).

Colazas, X., & Olson, L. (1983). Subsidence monitoring methods and beach mark elevation response to water injection, Wilmington oil field, Long Beach, California. Proceedings of 1982 Forum on Subsidence due to Fluid Withdrawals,

Connell, L. D., Mazumder, S., Sander, R., Camilleri, M., Pan, Z., & Heryanto, D. (2016). Laboratory characterisation of coal matrix shrinkage, cleat compressibility and the geomechanical properties determining reservoir permeability. *Fuel*, *165*, 499-512. https://doi.org/https://doi.org/10.1016/j.fuel.2015.10.055

Cook, A. G. B., S. E.; and Draper, J. J. (2013). Post-orogenic Mesozoic basins and magmatism. In P. A. Jell (Ed.), *Geology of Queensland* (pp. 970). Geological Survey of Queensland.

Crilly, M. S., & Driscoll, R. M. C. (2000). The behaviour of lightly loaded piles in swelling ground and implications for their design. *Proceedings of the Institution of Civil Engineers: Geotechnical Engineering*, *143*(1), 3-16.

Crosdale, P. J., Moore, T. A., & Mares, T. E. (2008). Influence of moisture content and temperature on methane adsorption isotherm analysis for coals from a low-rank, biogenically-sourced gas reservoir. *International Journal of Coal Geology*, *76*(1), 166-174. https://doi.org/https://doi.org/10.1016/j.coal.2008.04.004

Crosetto, M., Monserrat, O., Cuevas-González, M., Devanthéry, N., & Crippa, B. (2016). Persistent Scatterer Interferometry: A review. *ISPRS Journal of Photogrammetry and Remote Sensing*, *115*, 78-89. https://doi.org/https://doi.org/10.1016/j.isprsjprs.2015.10.011

Cui, X., & Bustin, R. M. (2005). Volumetric strain associated with methane desorption and its impact on coalbed gas production from deep coal seams. *AAPG Bulletin*, *89*(9), 1181-1202. https://doi.org/10.1306/05110504114

David, K., Timms, W. A., Barbour, S. L., & Mitra, R. (2017). Tracking changes in the specific storage of overburden rock during longwall coal mining. *Journal of Hydrology*, *553*, 304-320. https://doi.org/10.1016/j.jhydrol.2017.07.057

Day, S., Fry, R., & Sakurovs, R. (2008). Swelling of Australian coals in supercritical CO2. *International Journal of Coal Geology*, *74*(1), 41-52. https://doi.org/https://doi.org/10.1016/j.coal.2007.09.006

de Andrade Vieira Filh, C. L., Sobczak, K., Holl, H.-G., Hurter, S., & Vasconcelos, P. (2021). Understanding the nature of the transition between Late Jurassic formations of the Surat Basin through borehole image logs using cumulative dip plots. Australian Earth Sciences Convention 2021, Virtual.

de Vallejo, L. G., & Ferrer, M. (2011). *Geological engineering* (s. Edition, Ed.). CRC Press.

Diaz, J. C. F., Carter, W. E., Shrestha, R. L., & Glennie, C. L. (2017). LiDAR Remote Sensing. In P. J., M. S., & C.-L. S. (Eds.), *Handbook of Satellite Applications* (pp. 929-980). Springer, Cham. https://doi.org/https://doi.org/10.1007/978-3-319-23386-4_44

Doornhof, D., Kristiansen, T. G., Nagel, N. B., Pattillo, P. D., & Sayers, C. (2006). Compaction and subsidence. *Oilfield Review*, *18*(3), 50-68.

Du, Z., Ge, L., Ng, A. H.-M., Li, X., & Li, L. (2018). Monitoring of ground deformation in Liulin district, China using InSAR approaches. *International Journal of Digital Earth*, *11*(3), 264-283. https://doi.org/10.1080/17538947.2017.1322151

Dudley, J. W., Deviney, D. B., Rai, U. B., Hol, S., Hummel, N., Sutton, H., & Gear, I. (2019). Methane Pore Pressure Depletion Experiments on Coal Seam Gas Reservoir Rock. 53rd U.S. Rock Mechanics/Geomechanics Symposium,

Dusseault, M., & Rothenburg, L. (2002). Analysis of deformation measurements for reservoir management. *Oil & Gas Science and Technology*, *57*(5), 539-554. https://doi.org/10.2516/ogst:2002036

Dusseault, M. B., Yin, S., Rothenburg, L., & Han, H. (2007). Seismic monitoring and geomechanics simulation. *Leading Edge (Tulsa, OK)*, *26*(5), 610-620. https://doi.org/10.1190/1.2737119

Eissa, E. A., & Kazi, A. (1988). Relation between static and dynamic Young's moduli of rocks. *International Journal of Rock Mechanics and Mining Sciences & Geomechanics Abstracts*, *25*(6), 479-482. https://doi.org/https://doi.org/10.1016/0148-9062(88)90987-4

Ellsworth, W. L., Giardini, D., Townend, J., Ge, S., & Shimamoto, T. (2019). Triggering of the Pohang, Korea, Earthquake (Mw 5.5) by Enhanced Geothermal System Stimulation. *Seismological Research Letters*, *90*(5), 1844-1858. https://doi.org/10.1785/0220190102

Enever, J., Casey, D., & Bocking, M. (1999). The Role of In-Situ Stress in Coalbed Methane Exploration. In M. Mastalerz, M. Glikson, & S. D. Golding (Eds.), *Coalbed Methane: Scientific, Environmental and Economic Evaluation* (pp. 297-303). Springer Netherlands. https://doi.org/10.1007/978-94-017-1062-6_18

Epstein, V. J. (1987). *Hydrologic and geologic factors affecting land subsidence near Eloy, Arizona* (Vol. 87). Department of the Interior, US Geological Survey.

Erban, L. E., Gorelick, S. M., & Zebker, H. A. (2014). Groundwater extraction, land subsidence, and sea-level rise in the Mekong Delta, Vietnam. *Environmental Research Letters*, *9*(8). https://doi.org/10.1088/1748-9326/9/8/084010

Escojido, D. (1981). Subsidence in the Bolivar Coast. In R. F. Meyer & C. T. Steele (Eds.), *Future of heavy crude and tar sands* (pp. 761-767). McGraw-Hill.

Espinoza, D. N., Pereira, J. M., Vandamme, M., Dangla, P., & Vidal-Gilbert, S. (2015). Desorption-induced shear failure of coal bed seams during gas depletion. *International Journal of Coal Geology*, *137*, 142-151. https://doi.org/https://doi.org/10.1016/j.coal.2014.10.016

Esterle, J. S., Williams, R., Sliwa, R., & Malone, M. (2006). *Variability in gas reservoir parameters that impact on emissions estimations for Australian black coals*. ACARP.

Fakhri, F., & Kalliola, R. (2015). Monitoring ground deformation in the settlement of Larissa in Central Greece by implementing SAR interferometry [journal article]. *Natural Hazards*, *78*(2), 1429-1445. https://doi.org/10.1007/s11069-015-1779-6
Fei, W., Huiyuan, B., Jun, Y., & Yonghao, Z. (2016). Correlation of dynamic and static elastic parameters of rock. *Electronic Journal of Geotechnical Engineering*, *21*, 1551-1560.
Ferguson, W., Bere, A., Rodriguez, C., Félix, L., Marsili, M., & Medeiros, L. (2016). Modelling of a deepwater Brazilian field to assess fault reactivation and the insitu stresses during production. *First Break*, *34*(6). https://doi.org/https://doi.org/10.3997/1365-2397.2016007
Ferretti, A. (2014). *Satellite InSAR Data: Reservoir Monitoring from Space*. EAGE Publications.
Ferretti, A., Fumagalli, A., Novali, F., Prati, C., Rocca, F., & Rucci, A. (2011). A New Algorithm for Processing Interferometric Data-Stacks: SqueeSAR. *IEEE Transactions on Geoscience and Remote Sensing*, *49*(9), 3460-3470. https://doi.org/10.1109/TGRS.2011.2124465
Ferretti, A., Prati, C., & Rocca, F. (2001). Permanent scatterers in SAR interferometry. *IEEE Transactions on Geoscience and Remote Sensing*, *39*(1), 8-20. https://doi.org/10.1109/36.898661
Finnegan, N. J., Pritchard, M. E., Lohman, R. B., & Lundgren, P. R. (2008). Constraints on surface deformation in the Seattle, WA, urban corridor from satellite radar interferometry time-series analysis. *Geophysical Journal International*, *174*(1), 29-41. https://doi.org/10.1111/j.1365-246X.2008.03822.x
Finol, A. S., & Sancevic, Z. A. (1995). Chapter 7 Subsidence in Venezuela. In G. V. Chilingarian, E. C. Donaldson, & T. F. Yen (Eds.), *Developments in Petroleum Science* (Vol. 41, pp. 337-372). Elsevier. https://doi.org/https://doi.org/10.1016/S0376-7361(06)80054-3
Fityus, S. G., Smith, D. W., & Allman, M. A. (2004). Expansive soil test site near Newcastle. *Journal of Geotechnical and Geoenvironmental Engineering*, *130*(7), 686-695. https://doi.org/10.1061/(ASCE)1090-0241(2004)130:7(686)
Fokker, P. A. (2002, 2002/10/23). *Subsidence prediction and inversion of subsidence data* SPE/ISRM Rock Mechanics Conference, Irving, Texas.
Fokker, P. A., Gunnink, J. L., Koster, K., & de Lange, G. (2019). Disentangling and Parameterizing Shallow Sources of Subsidence: Application to a Reclaimed Coastal Area, Flevoland, the Netherlands. *Journal of Geophysical Research: Earth Surface*, *124*(5), 1099-1117. https://doi.org/https://doi.org/10.1029/2018JF004975
Fokker, P. A., & Orlic, B. (2006). Semi-analytic modelling of subsidence. *Mathematical Geology*, *38*(5), 565-589. https://doi.org/10.1007/s11004-006-9034-z
Freij-Ayoub, R., Underschultz, J., Li, F., Trefry, C., Hennih, A., Otto, C., & McInnes, K. (2007). *Simulation of coastal subsidence and storm wave inundation risk in the Gippsland Basin* (Petroleum Report 07-003).
Fuhrmann, T., Batchelor, J., McCall, T., & Garthwaite, M. C. (2020). *Positions and orientations for the Queensland corner reflector array, Australia: report on geodetic surveys conducted in May and June 2018*.
Fuhrmann, T., Cuenca, M. C., Knopfler, A., van Leijen, F. J., Mayer, M., Westerhaus, M., Hanssen, R. F., & Heck, B. (2015). Estimation of small surface displacements in the Upper Rhine Graben area from a combined analysis of PS-InSAR, levelling and GNSS data. *Geophysical Journal International*, *203*(1), 614-631. <Go to ISI>://WOS:000366492900043
Fuhrmann, T., & Garthwaite, M. C. (2019). Resolving Three-Dimensional Surface Motion with InSAR: Constraints from Multi-Geometry Data Fusion. *Remote Sensing*, *11*(3). https://doi.org/10.3390/rs11030241
Gabrysch, R. K. B., C. W. (1975). *Land-surface subsidence at Seabrook, Tex.* U. S. Geological Survey, Reston, VA, United States.
Gale, W. J., & Fabjanczyk, M. W. (1993). Design approach to assess coal mine roadway stability and support requirements. In *In: Eighth Australian Tunnelling Conference: Finding Common Ground. Parkville, VIC: Australasian Institute of Mining and Metallurgy, 1993: 153-159*. Australasian Institute of Mining and Metallurgy. https://doi.org/10.3316/informit.835476555816231
Galera, J. M., Alvarez, M., & Bieniawski, Z. T. (2005). Evaluation of the deformation modulus of rock masses: Comparison of pressuremeter and dilatometer tests with RMR prediction. Underground Works under Special Conditions,
Galloway, D. L., Hudnut, K. W., Ingebritsen, S. E., Phillips, S. P., Peltzer, G., Rogez, F., & Rosen, P. A. (1998). Detection of aquifer system compaction and land subsidence using interferometric synthetic aperture radar, Antelope Valley, Mojave Desert, California. *Water Resources Research*, *34*(10), 2573-2585. https://doi.org/10.1029/98WR01285
Galloway, D. L., Jones, D. R., & Ingebritsen, S. E. (1999). *Land subsidence in the United States* (Vol. 1182). US Geological Survey.
Gambolati, G. (1974). Second-order theory of flow in three-dimensional deforming media. *Water Resources Research*, *10*(6), 1217-1228.
Gambolati, G., & Freeze, R. A. (1973). Mathematical simulation of the subsidence of Venice: 1. Theory. *Water Resources Research*, *9*(3), 721-733. https://doi.org/10.1029/WR009i003p00721
Gambolati, G., & Teatini, P. (2015). Geomechanics of subsurface water withdrawal and injection. *Water Resources Research*, *51*(6), 3922-3955. https://doi.org/10.1002/2014wr016841

Gambolati, G., Teatini, P., Baú, D., & Ferronato, M. (2000). Importance of poroelastic coupling in dynamically active aquifers of the Po river basin, Italy. *Water Resources Research*, *36*(9), 2443-2459.
Gan, H., Nandi, S. P., & Walker, P. L. (1972). Nature of the porosity in American coals. *Fuel*, *51*(4), 272-277. https://doi.org/https://doi.org/10.1016/0016-2361(72)90003-8
Garthwaite, M. C., & Fuhrmann, T. (2020). *Subsidence monitoring in the Sydney Basin, New South Wales: Results of the Camden Environmental Monitoring Project* (Record 2020/16).
Garthwaite, M. C., Hazelwood, M., Nancarrow, S., Hislop, A., & Dawson, J. H. (2015). A regional geodetic network to monitor ground surface response to resource extraction in the northern Surat Basin, Queensland. *Australian Journal of Earth Sciences*, *62*(4), 469-477. https://doi.org/10.1080/08120099.2015.1040073
GasFields Commission Queensland. (2021). *Industry snapshot - shared landscapes.*
GasFields Commission Queensland. (2022). *Regulatory review of coal seam gas-induced subsidence.*
Gash, B. W. (1991). Measurement of "Rock Properties" in Coal for Coalbed Methane Production. SPE Annual Technical Conference and Exhibition,
Gazzola, L., Ferronato, M., Frigo, M., Janna, C., Teatini, P., Zoccarato, C., Antonelli, M., Corradi, A., Dacome, M. C., & Mantica, S. (2021). A novel methodological approach for land subsidence prediction through data assimilation techniques. *Computational Geosciences*, *25*(5), 1731-1750. https://doi.org/10.1007/s10596-021-10062-1
Geertsma, J. (1973). Land Subsidence Above Compacting Oil and Gas Reservoirs. *Journal of Petroleum Technology*, *25*(6), 734-744. https://doi.org/10.2118/3730-PA
Geological Survey of Queensland. (2012). *Queensland's coal seam gas overview.* E. D. a. I. Department of Employment. http://www.landtrakcorp.com/wp-content/uploads/2012/01/coal-seam-gas-2012-facts.pdf
Geoscience Australia. (2021). *Australia's Energy Commodity Resources.* http://pid.geoscience.gov.au/dataset/ga/130098
Geoscience Australia. (2022a). *Positioning Australia.* https://www.ga.gov.au/scientific-topics/positioning-navigation/positioning-australia
Geoscience Australia. (2022b). *Station Coordinates and Maps.* https://www.ga.gov.au/scientific-topics/positioning-navigation/geodesy/gnss-networks/station-coordinates-and-maps
Golder Associates. (2010). *Queensland Gas Company - Assessment of subsidence due to coal seam gas extraction* (097626104-011-Rev0).
Golding, S. D., Boreham, C. J., & Esterle, J. S. (2013). Stable isotope geochemistry of coal bed and shale gas and related production waters: A review. *International Journal of Coal Geology*, *120*, 24-40. https://doi.org/https://doi.org/10.1016/j.coal.2013.09.001
Gonthier, G. J. (2007). *A graphical method for estimation of barometric efficiency from continuous data; concepts and application to a site in the Piedmont, Air Force Plant 6, Marietta, Georgia.* U. S. Geological Survey, Reston, VA, United States.
Gray, I., Zhao, X., Liu, L., & Wood, J. (2019). *The Young's moduli, Poisson's ratios and poroeleastic coefficients of coals* (ACARP Project C26061).
Grigg, K. M., & Katzenstein, K. W. (2013, 27-30 October, 2013). *Using InSAR and groundwater pumping data to model land subsidence from coalbed methane production in the Powder River Basin, Wyoming* 125th Anniversary Annual Meeting and Expo, Denver, Colorado.
Gu, F., & Chalaturnyk, R. J. (2006). Numerical Simulation of Stress and Strain Due to Gas Sorption/Desorption and Their Effects on In Situ Permeability of Coalbeds. *Journal of Canadian Petroleum Technology*, *45*(10). https://doi.org/10.2118/06-10-05
Hamilton, S. K., Golding, S. D., Baublys, K. A., & Esterle, J. S. (2014). Stable isotopic and molecular composition of desorbed coal seam gases from the Walloon Subgroup, eastern Surat Basin, Australia. *International Journal of Coal Geology*, *122*, 21-36. https://doi.org/https://doi.org/10.1016/j.coal.2013.12.003
Hanson, R. T. (1988). Aquifer-system compaction, Tucson Basin and Avra Valley, Arizona.
Hanssen, R. F. (2001). *Radar Interferometry: Data Interpretation and Error Analysis* (Vol. 2). Springer Netherlands. https://doi.org/https://doi.org/10.1007/0-306-47633-9
Hatton, T. J., Otto, C., & Underschultz, J. (2004). *Falling water levels in the Latrobe Aquifer, Gippsland Basin - Determination of cause and recommendations for future work.*
Hayes, P., Nicol, C., La Croix, A. D., Pearce, J., Gonzalez, S., Wang, J., Harfoush, A., He, J., Moser, A., Helm, L., Morris, R., & Gornall, D. (2020). Enhancing geological and hydrogeological understanding of the Precipice Sandstone aquifer of the Surat Basin, Great Artesian Basin, Australia, through model inversion of managed aquifer recharge datasets. *Hydrogeology Journal*, *28*(1), 175-192. https://doi.org/10.1007/s10040-019-02079-9
Hebblewhite, B. K. (2022). *Subsidence associated with underground coal mining explanatory note.* Independent Expert Scientific Committee on Coal Seam Gas and Large Coal Mining Development.
Helm, D. (1984). Latrobe Valley subsidence predictions: the modeling of time-dependent ground movement due to groundwater withdrawal. *Joint Report of Fuel Department and Design Engineering and Environment Department, State Electricity Commission of Victoria, Melbourne.*
Helm, D. C. (1975). One-dimensional simulation of aquifer system compaction near Pixley, California; 1, constant parameters. *Water Resources Research*, *11*(3), 465-478. https://doi.org/10.1029/WR011i003p00465

Helm, D. C. (1976). One-dimensional simulation of aquifer system compaction near Pixley, California: 2. Stress-Dependent Parameters. *Water Resources Research*, *12*(3), 375-391. https://doi.org/10.1029/WR012i003p00375
Helm, D. C. (1978). Field verification of a one-dimensional mathematical model for transient compaction and expansion of a confined aquifer system. Verification of Mathematical and Physical Models in Hydraulic Engineering,
Herckenrath, D., Doherty, J., & Panday, S. (2015). Incorporating the effect of gas in modelling the impact of CBM extraction on regional groundwater systems. *Journal of Hydrology*, *523*, 587-601. https://doi.org/https://doi.org/10.1016/j.jhydrol.2015.02.012
Hernandez-Marin, M., & Burbey, T. J. (2010). Controls on initiation and propagation of pumping-induced earth fissures: insights from numerical simulations. *Hydrogeology Journal*, *18*(8), 1773-1785.
Hernandez-Marin, M., & Burbey, T. J. (2012). Fault-controlled deformation and stress from pumping-induced groundwater flow. *Journal of Hydrology*, *428*, 80-93.
Hettema, M., Papamichos, E., & Schutjens, P. (2002). Subsidence delay: field observations and analysis. *Oil & Gas Science and Technology*, *57*(5), 443-458. https://doi.org/10.2516/ogst:2002029
Hocking, J. B. (1980). *Definition and revision of Tertiary Stratigraphic Units, Onshore Gippsland Basin* (1976/1).
Hoerning, S., & Rodger, I. (2021). Key Properties are not Well Represented by Means: Spatial Asymmetry in Coal Seam Gas Reservoir Modelling. SPE/AAPG/SEG Asia Pacific Unconventional Resources Technology Conference,
Hofmann-Wellenhof, B., Lichtenegger, H., & Wasle, E. (2008). More on GNSS. In *GNSS — Global Navigation Satellite Systems: GPS, GLONASS, Galileo, and more* (pp. 397-430). Springer Vienna. https://doi.org/10.1007/978-3-211-73017-1_12
Holdgate, G. R., & Clarke, J. D. A. (2000). A review of tertiary brown coal deposits in Australia: Their depositional factors and eustatic correlations. *AAPG Bulletin*, *84*(8), 1129-1151.
Holdgate, G. R., Wallace, M. W., Gallagher, S. J., Smith, A. J., Keene, J. B., Moore, D., & Shafik, S. (2003). Plio-Pleistocene tectonics and eustasy in the Gippsland Basin, southeast Australia: Evidence from magnetic imagery and marine geological data. *Australian Journal of Earth Sciences*, *50*(3), 403-426. https://doi.org/10.1046/j.1440-0952.2003.01004.x
Holzer, T. L. (1984). Ground failure induced by ground-water withdrawal from unconsolidated sediment. *Man-induced land subsidence*, 67-105. https://www.scopus.com/inward/record.uri?eid=2-s2.0-0021606905&partnerID=40&md5=32eab1610a54cce0c41a40c77998b8b3
Hooper, A., Zebker, H., Segall, P., & Kampes, B. (2004). A new method for measuring deformation on volcanoes and other natural terrains using InSAR persistent scatterers [https://doi.org/10.1029/2004GL021737]. *Geophysical Research Letters*, *31*(23). https://doi.org/https://doi.org/10.1029/2004GL021737
Hsieh, P. A. (1996). Deformation-induced changes in hydraulic head during ground-water withdrawal. *Groundwater*, *34*(6), 1082-1089.
Hu, J., Li, Z. W., Ding, X. L., Zhu, J. J., Zhang, L., & Sun, Q. (2014). Resolving three-dimensional surface displacements from InSAR measurements: A review. *Earth-Science Reviews*, *133*, 1-17. https://doi.org/https://doi.org/10.1016/j.earscirev.2014.02.005
Huang, Y., Yang, Y., & Li, J. (2015). Numerical simulation of artificial groundwater recharge for controlling land subsidence. *KSCE Journal of Civil Engineering*, *19*(2), 418-426. https://doi.org/10.1007/s12205-015-0505-y
Ingebritsen, S. E., & Galloway, D. L. (2014). Coastal subsidence and relative sea level rise. *Environmental Research Letters*, *9*(9). https://doi.org/10.1088/1748-9326/9/9/091002
Jacobs. (2016). *Ground motion modelling using OGIA 2016 modelling results* (4500251750).
Jahangir, E., Deck, O., & Masrouri, F. (2012). Estimation of ground settlement beneath foundations due to shrinkage of clayey soils. *Canadian Geotechnical Journal*, *49*(7), 835-852. https://doi.org/10.1139/T2012-042
Jahr, T., Jentzsch, G., Gebauer, A., & Lau, T. (2008). Deformation, seismicity, and fluids: Results of the 2004/2005 water injection experiment at the KTB/Germany. *Journal of Geophysical Research: Solid Earth*, *113*(B11).
Jensen, J. (2000). *Remote Sensing of the Environment: An Earth Resource Perspective*. Prentice-Hall.
Johnson, R. L., Cheong, S., & Farley, A. (2021). Characterising the application of horizontal wells and indirect hydraulic fracturing for improved coal seam gas drainage. *The APPEA Journal*, *61*(1), 89-105. https://doi.org/https://doi.org/10.1071/AJ20122
Jolivet, R., Grandin, R., Lasserre, C., Doin, M.-P., & Peltzer, G. (2011). Systematic InSAR tropospheric phase delay corrections from global meteorological reanalysis data. *Geophysical Research Letters*, *38*(17). https://doi.org/https://doi.org/10.1029/2011GL048757
Jung, H., & Frigaard, I. A. (2022). Evaluation of common cementing practices affecting primary cementing quality. *Journal of Petroleum Science and Engineering*, *208*, 109622. https://doi.org/https://doi.org/10.1016/j.petrol.2021.109622

Kaplan, E. D. (2017). Introduction. In E. D. Kaplan & C. J. Hegarty (Eds.), *Understanding GPS/GNSS - Principles and Applications (3rd Edition)* (pp. 1-18). Artech House. https://app.knovel.com/hotlink/pdf/id:kt011M7GS2/understanding-gps-gnss/introduction

Kasmarek, M. C. (2012). *Hydrogeology and simulation of groundwater flow and land-surface subsidence in the northern part of the Gulf Coast aquifer system, Texas, 1891-2009*. U. S. Geological Survey, Reston, VA, United States.

Kasmarek, M. C. R., James L. (2004). *Hydrogeology and simulation of ground-water flow and land-surface subsidence in the northern part of the Gulf Coast aquifer system, Texas*. U. S. Geological Survey, Reston, VA, United States.

Knutson, T. R., McBride, J. L., Chan, J., Emanuel, K., Holland, G., Landsea, C., Held, I., Kossin, J. P., Srivastava, A. K., & Sugi, M. (2010). Tropical cyclones and climate change. *Nature Geoscience*, *3*(3), 157-163. https://doi.org/10.1038/ngeo779

Kolker, A. S., Allison, M. A., & Hameed, S. (2011). An evaluation of subsidence rates and sea-level variability in the northern Gulf of Mexico. *Geophysical Research Letters*, *38*(21). https://doi.org/10.1029/2011GL049458

Langmuir, I. (1916). The constitution and fundamental properties of solids and liquids. Part I. Solids. *Journal of the American Chemical Society*, *38*(11), 2221-2295. https://doi.org/10.1021/ja02268a002

Larsen, J. W. (2004). The effects of dissolved CO2 on coal structure and properties. *International Journal of Coal Geology*, *57*(1), 63-70. https://doi.org/https://doi.org/10.1016/j.coal.2003.08.001

Laubach, S. E., Marrett, R. A., Olson, J. E., & Scott, A. R. (1998). Characteristics and origins of coal cleat: A review. *International Journal of Coal Geology*, *35*(1), 175-207. https://doi.org/https://doi.org/10.1016/S0166-5162(97)00012-8

Lawrie, S. (2012). *Use of Interferometric Synthetic Aperture Radar (InSAR) to Detect Strain Accumulation on the Sorong Fault Zone, West Papua, Indonesia* [Honours, The Australian National University].

Leonardi, C. R., Flottmann, T., Pandey, V. J., & Johnson, R. J. (2019). Quantifying the Influence of Three Dimensionality on Hydraulic Fracturing in Coal Seam Gas Wells. SPE/AAPG/SEG Asia Pacific Unconventional Resources Technology Conference,

Leonardi, C. R., Hurter, S., Chen, Z., & Underschultz, J. (2017). *Surface movement and shallow processes* (Report Reference: 149345).

Lewis, R., & Schrefler, B. (1978). A fully coupled consolidation model of the subsidence of Venice. *Water Resources Research*, *14*(2), 223-230.

Li, C., Wang, Z., Shi, L., & Feng, R. (2017). Analysis of Analytical Models Developed under the Uniaxial Strain Condition for Predicting Coal Permeability during Primary Depletion. *Energies*, *10*(11), 1849. https://www.mdpi.com/1996-1073/10/11/1849

Lin, X., Sutherland, G., Cumming, D., Thomas, B., & Sani, A. (2018). Increasing Coal Seam Gas Field Productivity with Horizontal Well Technology: A Case Study. SPE Asia Pacific Oil and Gas Conference and Exhibition,

Ling, H. I., Smyth, A., & Betti, R. (2009). *Poromechanics IV*. DEStech Publications, Inc.

Liu, J., Fokker, P. A., & Spiers, C. J. (2017). Coupling of swelling, internal stress evolution, and diffusion in coal matrix material during exposure to methane. *Journal of Geophysical Research: Solid Earth*, *122*(2), 844-865. https://doi.org/https://doi.org/10.1002/2016JB013322

Liu, S., Wang, Y., & Harpalani, S. (2016). Anisotropy characteristics of coal shrinkage/swelling and its impact on coal permeability evolution with CO2 injection [https://doi.org/10.1002/ghg.1592]. *Greenhouse Gases: Science and Technology*, *6*(5), 615-632. https://doi.org/https://doi.org/10.1002/ghg.1592

Liu, Y., & Helm, D. C. (2008a). Inverse procedure for calibrating parameters that control land subsidence caused by subsurface fluid withdrawal: 1. Methods. *Water Resources Research*, *44*(7).

Liu, Y., & Helm, D. C. (2008b). Inverse procedure for calibrating parameters that control land subsidence caused by subsurface fluid withdrawal: 2. Field application. *Water Resources Research*, *44*(7).

Mahoney, S. A., Rufford, T. E., Dmyterko, A. S., Rudolph, V., & Steel, K. M. (2015). The Effect of Rank and Lithotype on Coal Wettability and its Application to Coal Relative Permeability Models. SPE Asia Pacific Unconventional Resources Conference and Exhibition,

Mares, T. E., Radliński, A. P., Moore, T. A., Cookson, D., Thiyagarajan, P., Ilavsky, J., & Klepp, J. (2009). Assessing the potential for CO2 adsorption in a subbituminous coal, Huntly Coalfield, New Zealand, using small angle scattering techniques. *International Journal of Coal Geology*, *77*(1), 54-68. https://doi.org/https://doi.org/10.1016/j.coal.2008.07.007

Masoudian, M. S. (2016). Multiphysics of carbon dioxide sequestration in coalbeds: A review with a focus on geomechanical characteristics of coal. *Journal of Rock Mechanics and Geotechnical Engineering*, *8*(1), 93-112. https://doi.org/https://doi.org/10.1016/j.jrmge.2015.08.002

Masoudian, M. S., Airey, D. W., & El-Zein, A. (2016). The role of coal seam properties on coupled processes during CO2 sequestration: A parametric study. *Greenhouse Gases: Science and Technology*, *6*(4), 492-518. https://doi.org/https://doi.org/10.1002/ghg.1575

Masoudian, M. S., Leonardi, C., Chen, Z., & Underschultz, J. (2019a). The effect of sorption-induced shrinkage on the ground surface movement above gas-producing coalbeds. 53rd U.S. Rock Mechanics/Geomechanics Symposium,

Masoudian, M. S., Leonardi, C., Chen, Z., & Underschultz, J. (2019b). Towards the development of a baseline for surface movement in the Surat Cumulative Management Area. *The APPEA Journal*, *59*(1), 95-114. https://doi.org/https://doi.org/10.1071/AJ18181
Massarotto, P., Rudolph, V., & Golding, S. D. (2003, 7-8 May, 2003). *Anisotropic permeability characterisation of Permian coals* 2003 International Coalbed Methane Symposium, Alabama, USA.
Mastalerz, M., & Drobniak, A. (2020). 5 - Coalbed Methane: Reserves, Production, and Future Outlook. In T. M. Letcher (Ed.), *Future Energy (Third Edition)* (pp. 97-109). Elsevier. https://doi.org/https://doi.org/10.1016/B978-0-08-102886-5.00005-0
Mastro, P., Serio, C., Masiello, G., & Pepe, A. (2020). The Multiple Aperture SAR Interferometry (MAI) Technique for the Detection of Large Ground Displacement Dynamics: An Overview. *Remote Sensing*, *12*(7), 1189. https://www.mdpi.com/2072-4292/12/7/1189
Mathias, S. A., Nielsen, S., & Ward, R. L. (2019). Storage Coefficients and Permeability Functions for Coal-Bed Methane Production Under Uniaxial Strain Conditions. *Transport in Porous Media*, *130*(2), 627-636. https://doi.org/10.1007/s11242-019-01331-w
Mavor, M. J., Hartman, C., & Pratt, T. J. (2004). Uncertainty in sorption isotherm measurements. 2004 International Coalbed Methane Symposium, University of Alabama, Tuscaloosa, Alabama.
Mayuga, M., & Allen, D. (1969). Subsidence in the Wilmington Oil Field, Long Beach, California, USA. Proceedings of Tokyo Symposium on Land Subsidence,
Mayuga, M. N. (1970). Geology and Development of California's Giant—Wilmington Oil Field1. In M. T. Halbouty (Ed.), *Geology of Giant Petroleum Fields* (Vol. 14, pp. 0). American Association of Petroleum Geologists. https://doi.org/10.1306/M14368C7
Mayuga, M. N., & Allen, D. R. (1970). Subsidence in the Wilmington Oil Field, Long Beach, California, U.S.A. In L. J. Tison (Ed.), *Land Subsidence* (pp. 66-79). International Association of Scientific Hydrology, UNESCO.
McClure, J. E., Berg, S., & Armstrong, R. T. (2021). Capillary fluctuations and energy dynamics for flow in porous media. *Physics of Fluids*, *33*(8), 083323. https://doi.org/10.1063/5.0057428
McIntyre, D. S., Watson, C. L., & Loveday, J. (1982). Swelling of a clay soil profile under ponding. *Australian Journal of Soil Research*, *20*(2), 71-79.
McKee, C. R., & Bumb, A. C. (1987). Flow-Testing Coalbed Methane Production Wells in the Presence of Water and Gas. *SPE Formation Evaluation*, *2*(04), 599-608. https://doi.org/10.2118/14447-pa
McManamon, P. (2019). *LiDAR Technologies and Systems*. SPIE. https://app.knovel.com/hotlink/pdf/id:kt012EEJ02/lidar-technologies-systems/title-page
McMillan, T. C., Rau, G. C., Timms, W. A., & Andersen, M. S. (2019). Utilizing the Impact of Earth and Atmospheric Tides on Groundwater Systems: A Review Reveals the Future Potential [https://doi.org/10.1029/2018RG000630]. *Reviews of Geophysics*, *57*(2), 281-315. https://doi.org/https://doi.org/10.1029/2018RG000630
Merritt, M. L. (2004). *Estimating hydraulic properties of the Floridan aquifer system by analysis of Earth-tide, ocean-tide, and barometric effects, Collier and Hendry Counties, Florida*. U. S. Geological Survey, [Reston, VA], United States.
Michael, K., Bunch, M., & Varma, S. (2013). Simulation of the cumulative impacts of CO2 geological storage and petroleum production on aquifer pressures in the offshore Gippsland Basin. *International Journal of Greenhouse Gas Control*, *19*(Supplement C), 310-321. https://doi.org/https://doi.org/10.1016/j.ijggc.2013.09.009
MIT Energy Initiative. (2011). *The future of natural gas - an interdisciplinary MIT study*.
Moore, T. A. (2012). Coalbed methane: A review. *International Journal of Coal Geology*, *101*, 36-81. https://doi.org/https://doi.org/10.1016/j.coal.2012.05.011
Moreira, A., Prats-Iraola, P., Younis, M., Krieger, G., Hajnsek, I., & Papathanassiou, K. P. (2013). A tutorial on synthetic aperture radar. *IEEE Geoscience and Remote Sensing Magazine*, *1*(1), 6-43.
Müller, N. (2011). Supercritical CO2-Brine Relative Permeability Experiments in Reservoir Rocks—Literature Review and Recommendations. *Transport in Porous Media*, *87*(2), 367-383. https://doi.org/10.1007/s11242-010-9689-2
Muntendam-Bos, A. G., Kroon, I. C., & Fokker, P. A. (2008). Time-dependent Inversion of Surface Subsidence due to Dynamic Reservoir Compaction [journal article]. *Mathematical Geosciences*, *40*(2), 159-177. https://doi.org/10.1007/s11004-007-9135-3
Nagel, N. B. (2001). Compaction and subsidence issues within the petroleum industry: From wilmington to ekofisk and beyond. *Physics and Chemistry of the Earth, Part A: Solid Earth and Geodesy*, *26*(1), 3-14. https://doi.org/https://doi.org/10.1016/S1464-1895(01)00015-1
Ng, A. H.-M., Ge, L., & Li, X. (2015). Assessments of land subsidence in the Gippsland Basin of Australia using ALOS PALSAR data. *Remote Sensing of Environment*, *159*(Supplement C), 86-101. https://doi.org/https://doi.org/10.1016/j.rse.2014.12.003
Ng, A. H.-M., Ge, L., Li, X., Abidin, H. Z., Andreas, H., & Zhang, K. (2012). Mapping land subsidence in Jakarta, Indonesia using persistent scatterer interferometry (PSI) technique with ALOS PALSAR. *International Journal*

of Applied Earth Observation and Geoinformation, *18*, 232-242. https://doi.org/https://doi.org/10.1016/j.jag.2012.01.018
Nicot, J.-P., & Scanlon, B. R. (2012). Water Use for Shale-Gas Production in Texas, U.S. *Environmental Science & Technology*, *46*(6), 3580-3586. https://doi.org/10.1021/es204602t
Nowamooz, H. (2014). Effective stress concept on multi-scale swelling soils. *Applied Clay Science*, *101*, 205-214. https://doi.org/10.1016/j.clay.2014.07.036
OGIA. (2016a). *Hydrogeological conceptualisation report for the Surat Cumulative Management Area.*
OGIA. (2016b). *Underground Water Impact Report for the Surat Cumulative Management Area.*
OGIA. (2019). *Underground water impact report for the Surat Cumulative Management Area.*
OGIA. (2021). *Underground water impact report for the Surat Cumulative Management Area.*
Ortiz-Zamora, D., & Ortega-Guerrero, A. (2010). Evolution of long-term land subsidence near Mexico City: Review, field investigations, and predictive simulations [https://doi.org/10.1029/2008WR007398]. *Water Resources Research*, *46*(1). https://doi.org/https://doi.org/10.1029/2008WR007398
Osmanoğlu, B., Sunar, F., Wdowinski, S., & Cabral-Cano, E. (2016). Time series analysis of InSAR data: Methods and trends. *ISPRS Journal of Photogrammetry and Remote Sensing*, *115*, 90-102. https://doi.org/https://doi.org/10.1016/j.isprsjprs.2015.10.003
Otott Jr, G. E., & Clarke, D. D. (1996). History of the Wilmington Field-1986-1996.
Ozawa, T., & Ueda, H. (2011). Advanced interferometric synthetic aperture radar (InSAR) time series analysis using interferograms of multiple-orbit tracks: A case study on Miyake-jima. *Journal of Geophysical Research: Solid Earth*, *116*(B12). https://doi.org/https://doi.org/10.1029/2011JB008489
Palmer, I. (2009). Permeability changes in coal: Analytical modeling. *International Journal of Coal Geology*, *77*(1), 119-126. https://doi.org/https://doi.org/10.1016/j.coal.2008.09.006
Palmer, I., & Mansoori, J. (1998). How Permeability Depends on Stress and Pore Pressure in Coalbeds: A New Model. *SPE Reservoir Evaluation & Engineering*, *1*(06), 539-544. https://doi.org/10.2118/52607-pa
Pan, Z., & Connell, L. D. (2011). Modelling of anisotropic coal swelling and its impact on permeability behaviour for primary and enhanced coalbed methane recovery. *International Journal of Coal Geology*, *85*(3), 257-267. https://doi.org/https://doi.org/10.1016/j.coal.2010.12.003
Pandey, V. J., Flottman, T., & Zwarich, N. R. (2017). Applications of Geomechanics to Hydraulic Fracturing: Case Studies From Coal Stimulations. *SPE Production & Operations*, *32*(04), 404-422. https://doi.org/10.2118/173378-pa
Pepe, A., & Calò, F. (2017). A Review of Interferometric Synthetic Aperture RADAR (InSAR) Multi-Track Approaches for the Retrieval of Earth's Surface Displacements. *Applied Sciences*, *7*(12), 1264. https://www.mdpi.com/2076-3417/7/12/1264
Pineda, J. A., & Sheng, D. (2013). *Subsidence - An overview of causes, risks and future developments for coal seam gas production* (Review of Coal Seam Gas Activities in NSW, Issue.
Poland, J. F. (1984). *Guidebook to studies of land subsidence due to ground-water withdrawal* (Vol. 40). United Nations Educational, Scientific and Cultural Organization (UNESCO), Paris, International.
Pope, J. P., & Burbey, T. J. (2003). *Characterization and modeling of land subsidence due to groundwater withdrawals from the confined aquifers of the Virginia Coastal Plain* (Publication Number Rep 03-308) Prince KR, Galloway DL (eds) U.S. Geological Survey Subsidence Interest Group Conference, Proceedings of the technical meeting, Galveston, Texas, 27–29 Nov 2001.
Pope, J. P., & Burbey, T. J. (2004). Multiple-Aquifer Characterization from Single Borehole Extensometer Records. *Groundwater*, *42*(1), 45-58.
Pratt, W. E., & Johnson, D. W. (1926). Local Subsidence of the Goose Creek Oil Field. *The Journal of Geology*, *34*(7), 577-590. http://www.jstor.org/stable/30056838
Prokopovich, N. P. (1986). Classification of land subsidence by origin. *Land subsidence. Proc. 3rd symposium, Venice, 1984*, 281-290.
Purcell, J. (2012). Developing a surface irrigation system. In D. Wiggington (Ed.), *WATERpak – a guide for irrigation management in cotton and grain farming systems* (Third ed.). Cotton Research and Development Corporation.
Queensland Building and Construction Commission. (2022). *A guide to preventing structural damage.* Retrieved 3 August from https://www.qbcc.qld.gov.au/sites/default/files/2021-10/guide-preventing-structural-damage.pdf
Radlinski, A. P., Mastalerz, M., Hinde, A. L., Hainbuchner, M., Rauch, H., Baron, M., Lin, J. S., Fan, L., & Thiyagarajan, P. (2004). Application of SAXS and SANS in evaluation of porosity, pore size distribution and surface area of coal. *International Journal of Coal Geology*, *59*(3), 245-271. https://doi.org/https://doi.org/10.1016/j.coal.2004.03.002
Rai, U. B., & Hummel, N. D. (2019). *Prediction of compaction and subsidence due to gas production from coal seams in the Surat Basin, Australia (report prepared for QGC Shell)* (Report Reference: SR.19.00168).
Rajora, A., Sharma, V., Oberhardt, M., Lukyanov, M., Lim, E., & Mazumder, S. (2019). Deviated Pad Wells in Surat: Journey So Far. SPE/AAPG/SEG Asia Pacific Unconventional Resources Technology Conference,

Rau, G. C., McMillan, T. C., Andersen, M. S., & Timms, W. A. (2022). In situ estimation of subsurface hydro-geomechanical properties using the groundwater response to semi-diurnal Earth and atmospheric tides. *Hydrol. Earth Syst. Sci.*, *26*(16), 4301-4321. https://doi.org/10.5194/hess-26-4301-2022
Reeves, J. A., Knight, R., Zebker, H. A., Kitanidis, P. K., & Schreüder, W. A. (2014). Estimating temporal changes in hydraulic head using InSAR data in the San Luis Valley, Colorado. *Water Resources Research*, *50*(5), 4459-4473. https://doi.org/10.1002/2013WR014938
Richards, L. A. (1931). CAPILLARY CONDUCTION OF LIQUIDS THROUGH POROUS MEDIUMS. *Physics*, *1*(5), 318-333. https://doi.org/10.1063/1.1745010
Rintoul, W. (1981). *Drilling ahead: Tapping California's richest oil fields*. Valley Publishers.
Roberts, R. (1992). Silver Springs/Renlim Field - Australia, Bowen Basin, Queensland. *Treatise of Petroleum Geology, Atlas of Oil and Gas Fields*, 219-236. https://www.scopus.com/inward/record.uri?eid=2-s2.0-84961718730&partnerID=40&md5=dfb74b550c63829cd5d72536b0857a3b
Robertson, E. P., & Christiansen, R. L. (2008). A permeability model for coal and other fractured, sorptive-elastic media. *SPE Journal*, *13*(03), 314-324. https://doi.org/10.2118/104380-pa
Roscoe, K. H., & Burland, J. (1968). On the generalized stress-strain behaviour of wet clay.
Ross, J., & Jeffrey, L. (1991). *Ground subsidence and bore collapse associated with groundwater withdrawals - Namoi Valley, NSW*.
Sadek, S., Ghanimeh, S., & El-Fadel, M. (2007). Predicted performance of clay-barrier landfill covers in arid and semi-arid environments. *Waste Management*, *27*(4), 572-583. https://doi.org/10.1016/j.wasman.2006.06.008
Safai, N. M., & Pinder, G. F. (1979). Vertical and horizontal land deformation in a desaturating porous medium. *Advances in Water Resources*, *2*, 19-25.
Safai, N. M., & Pinder, G. F. (1980). Vertical and horizontal land deformation due to fluid withdrawal. *International Journal for Numerical and Analytical Methods in Geomechanics*, *4*(2), 131-142.
Saghafi, A., Faiz, M., & Roberts, D. (2007). CO2 storage and gas diffusivity properties of coals from Sydney Basin, Australia. *International Journal of Coal Geology*, *70*(1), 240-254. https://doi.org/https://doi.org/10.1016/j.coal.2006.03.006
Sandhu, R. S. (1979). Modeling land subsidence. Evaluation and Prediction of Subsidence,
Santos. (2013). *Santos GLNG Project - CSG water monitoring and management plan - Summary plan Stage 2* (Revision 2).
Saurabh, S., & Harpalani, S. (2019). Anisotropy of coal at various scales and its variation with sorption. *International Journal of Coal Geology*, *201*, 14-25. https://doi.org/https://doi.org/10.1016/j.coal.2018.11.008
Schlumberger Reservoir Laboratories. (2017). *Geomechanics characterization of selected core material (prepared for Origin Energy)* (Report Reference: 16-015).
Schoonbeek, J. B. (1976). *Land Subsidence as a Result of Natural Gas Extraction in the Province of Groningen* SPE European Spring Meeting, https://doi.org/10.2118/5751-MS
Schultz, H., Hayes, P., McIntyre, N., & Miraldo-Ordens, C. (2021). *Resetting our understanding of the Surat Part of the Great Artesian Basin*. T. U. o. Queensland.
Schumer, R., & Jerolmack, D. J. (2009). Real and apparent changes in sediment accumulation rates over time. *Geophysical Research Abstracts*, *11*.
Seidle, J. P., Jeansonne, M. W., & Erickson, D. J. (1992). Application of Matchstick Geometry To Stress Dependent Permeability in Coals. SPE Rocky Mountain Regional Meeting,
Şenel, İ. G., Gürüz, A. G., Yücel, H., Kandas, A. W., & Sarofim, A. F. (2001). Characterization of Pore Structure of Turkish Coals. *Energy & Fuels*, *15*(2), 331-338. https://doi.org/10.1021/ef000081k
Shaw, D., Mostaghimi, P., & Armstrong, R. T. (2019). The dynamic behaviour of coal relative permeability curves. *Fuel*, *253*, 293-304. https://doi.org/https://doi.org/10.1016/j.fuel.2019.04.107
Shi, J.-Q., & Durucan, S. (2005). A Model for Changes in Coalbed Permeability During Primary and Enhanced Methane Recovery. *SPE Reservoir Evaluation & Engineering*, *8*(04), 291-299. https://doi.org/10.2118/87230-pa
Shi, J.-Q., Pan, Z., & Durucan, S. (2014). Analytical models for coal permeability changes during coalbed methane recovery: Model comparison and performance evaluation. *International Journal of Coal Geology*, *136*, 17-24. https://doi.org/https://doi.org/10.1016/j.coal.2014.10.004
Shi, J. Q., & Durucan, S. (2004). Drawdown Induced Changes in Permeability of Coalbeds: A New Interpretation of the Reservoir Response to Primary Recovery. *Transport in Porous Media*, *56*(1), 1-16. https://doi.org/10.1023/B:TIPM.0000018398.19928.5a
Smerdon, B. D., & Ransley, T. R. (2012). *Water resource assessment for the Surat region. A report to the Australian Government from the CSIRO Great Artesian Basin Water Resource Assessment*.
Smith, D. J. (1988). *Project Management Of Subsidence And Ekofisk Jacking Project* Offshore Technology Conference, https://doi.org/10.4043/5655-MS
Sobczak, K., Holl, H.-G., & Garnett, A. (2021). Estimating porosity and permeability in the Springbok Sandstone, Surat Basin (Queensland), using new wireline log-based workflow. *The APPEA Journal*, *61*(2), 720-725. https://doi.org/https://doi.org/10.1071/AJ20201

Somerton, W. H., Söylemezoğlu, I. M., & Dudley, R. C. (1975). Effect of stress on permeability of coal. *International Journal of Rock Mechanics and Mining Sciences & Geomechanics Abstracts*, *12*(5), 129-145. https://doi.org/https://doi.org/10.1016/0148-9062(75)91244-9

Sparks, D. P., McLendon, T. H., Saulsberry, J. L., & Lambert, S. W. (1995). The Effects of Stress on Coalbed Reservoir Performance, Black Warrior Basin, U.S.A. SPE Annual Technical Conference and Exhibition,

Standards Australia. (2011). *AS 2870 Residential slabs and footings*.

Sulak, R. M., Thomas, L. K., & Boade, R. R. (1991). 3D Reservoir Simulation of Ekofisk Compaction Drive (includes associated papers 24317 and 24400). *Journal of Petroleum Technology*, *43*(10), 1272-1278. https://doi.org/10.2118/19802-PA

Sun, C., McClure, J. E., Mostaghimi, P., Herring, A. L., Berg, S., & Armstrong, R. T. (2020a). Probing Effective Wetting in Subsurface Systems [https://doi.org/10.1029/2019GL086151]. *Geophysical Research Letters*, *47*(5), e2019GL086151. https://doi.org/https://doi.org/10.1029/2019GL086151

Sun, C., McClure, J. E., Mostaghimi, P., Herring, A. L., Shabaninejad, M., Berg, S., & Armstrong, R. T. (2020b). Linking continuum-scale state of wetting to pore-scale contact angles in porous media. *Journal of Colloid and Interface Science*, *561*, 173-180. https://doi.org/https://doi.org/10.1016/j.jcis.2019.11.105

Syvitski, J. P. M., & Saito, Y. (2007). Morphodynamics of deltas under the influence of humans. *Global and Planetary Change*, *57*(3-4), 261-282. https://doi.org/10.1016/j.gloplacha.2006.12.001

Taigbenu, A. E. (1999). Unsaturated Flow (Richards Equation). In *The Green Element Method* (pp. 217-230). Springer US. https://doi.org/10.1007/978-1-4757-6738-4_8

Teatini, P., Gambolati, G., Ferronato, M., Settari, A. T., & Walters, D. (2011). Land uplift due to subsurface fluid injection. *Journal of Geodynamics*, *51*(1), 1-16.

Teatini, P., Tosi, L., & Strozzi, T. (2012). Comment on "Recent subsidence of the Venice Lagoon from continuous GPS and interferometric synthetic aperture radar" by Y. Bock, S. Wdowinski, A. Ferretti, F. Novali, and A. Fumagalli. *Geochemistry, Geophysics, Geosystems*, *13*(7). https://doi.org/https://doi.org/10.1029/2012GC004191

Tenthorey, E., Vidal-Gilbert, S., Backé, G., Puspitasari, R., Pallikathekathil, Z. J., Maney, B., & Dewhurst, D. (2013). Modelling the geomechanics of gas storage: A case study from the Iona gas field, Australia. *International Journal of Greenhouse Gas Control*, *13*, 138-148.

Thakur, P. S., Steven J.; Aminian, Kashy; Rodvelt, Gary; Mosser, Morgan H.; D'Amico, Joseph S. (Ed.). (2020). *Coal bed methane: Theory and applications* (Second Edition ed.). Elsevier. https://doi.org/https://doi.org/10.1016/C2017-0-02178-X.

Thompson, B. R., & Walker, G. M. (1982, 15-19 November). *Coal resources – origin and utilisation in Australia – The geology of the Seaspray Depression: Gippsland Basin* Coal Group, Geological Society of Australia Symposium, Melbourne.

TNO. (2021). *Reservoir pressure and subsidence - Groningen field update for production profile GTS*. https://www.rvo.nl/sites/default/files/2021/04/Appendix-A-Pressure-and-Subsidence-March-GTS-raming-2021.pdf

Tomás, R., Romero, R., Mulas, J., Marturià, J. J., Mallorquí, J. J., Lopez-Sanchez, J. M., Herrera, G., Gutiérrez, F., González, P. J., Fernández, J., Duque, S., Concha-Dimas, A., Cocksley, G., Castañeda, C., Carrasco, D., & Blanco, P. (2014). Radar interferometry techniques for the study of ground subsidence phenomena: a review of practical issues through cases in Spain. *Environmental Earth Sciences*, *71*(1), 163-181. https://doi.org/10.1007/s12665-013-2422-z

Tosi, L., Teatini, P., Carbognin, L., & Brancolini, G. (2009). Using high resolution data to reveal depth-dependent mechanisms that drive land subsidence: The Venice coast, Italy. *Tectonophysics*, *474*(1-2), 271-284. https://doi.org/10.1016/j.tecto.2009.02.026

Towler, B., Firouzi, M., Underschultz, J., Rifkin, W., Garnett, A., Schultz, H., Esterle, J., Tyson, S., & Witt, K. (2016). An overview of the coal seam gas developments in Queensland. *Journal of Natural Gas Science and Engineering*, *31*, 249-271. https://doi.org/https://doi.org/10.1016/j.jngse.2016.02.040

Ulaby, F., & Long, D. (2014). *Microwave Radar and Radiometric Remote Sensing*. University of Michigan Press.

Underschultz, J. R., Vink, S., & Garnett, A. (2018). Coal seam gas associated water production in Queensland: Actual vs predicted. *Journal of Natural Gas Science and Engineering*, *52*, 410-422. https://doi.org/https://doi.org/10.1016/j.jngse.2018.02.010

van der Kamp, G. (2001). Methods for determining the in situ hydraulic conductivity of shallow aquitards – an overview. *Hydrogeology Journal*, *9*(1), 5-16. https://doi.org/10.1007/s100400000118

van Elk, J., Doornhof, D., Bommer, J. J., Bourne, S. J., Oates, S. J., Pinho, R., & Crowley, H. (2017). Hazard and risk assessments for induced seismicity in Groningen. *Netherlands Journal of Geosciences*, *96*(5), s259-s269. https://doi.org/10.1017/njg.2017.37

van Genuchten, M. T. (1980). A closed-form equation for predicting the hydraulic conductivity of unsaturated soils. *Soil Science Society of America Journal*, *44*(5), 892-898. https://doi.org/https://doi.org/10.2136/sssaj1980.03615995004400050002x

Walker, G. R., & Mallants, D. (2014). *Methodologies for investigating gas in water bores and links to coal seam gas development*. CSIRO.
Wang, K., Zang, J., Wang, G., & Zhou, A. (2014). Anisotropic permeability evolution of coal with effective stress variation and gas sorption: Model development and analysis. *International Journal of Coal Geology*, *130*, 53-65. https://doi.org/https://doi.org/10.1016/j.coal.2014.05.006
Webb, S. W. (2006). Two-Phase Gas Transport. In C. K. Ho & S. W. Webb (Eds.), *Gas Transport in Porous Media* (pp. 55-70). Springer Netherlands. https://doi.org/10.1007/1-4020-3962-x_5
Wegmüller, U., & Werner, C. (1997, 14-21 March). *Gamma SAR processor and interferometry software* 3rd ERS Symposium, Florence, Italy. https://earth.esa.int/eogateway/events/the-3rd-ers-symposium
Wei, Y.-n., Fan, W., & Cao, Y. (2017). Experimental study on the vertical deformation of aquifer soils under conditions of withdrawing and recharging of groundwater in Tongchuan region, China
Etude experimentale de la deformation verticale des sols daquifere en conditions dexploitation et de recharge des eaux souterraines dans la region du Tongchuan, Chine. *Hydrogeology Journal*, *25*(2), 297-309. https://doi.org/10.1007/s10040-016-1498-4
Werner, C., Wegmuller, U., Strozzi, T., & Wiesmann, A. (2003, 21-25 July 2003). Interferometric point target analysis for deformation mapping. IGARSS 2003. 2003 IEEE International Geoscience and Remote Sensing Symposium. Proceedings (IEEE Cat. No.03CH37477),
Wolff, R. G. (1970). Relationship between horizontal strain near a well and reverse water level fluctuation. *Water Resources Research*, *6*(6), 1721-1728.
Woodhouse, I. (2006). *Introduction to Microwave Remote Sensing*. CRC Press.
Wright, T. J., Parsons, B. E., & Lu, Z. (2004). Toward mapping surface deformation in three dimensions using InSAR. *Geophysical Research Letters*, *31*(1). https://doi.org/https://doi.org/10.1029/2003GL018827
Wu, G., Jia, S., & Wu, B. (2019). Comparison of a novel coupled hydro-mechanical model with typical analytical models in subsidence of coal seam gas extraction. *International Journal of Oil, Gas and Coal Technology*, *22*(2), 246-268. https://doi.org/10.1504/ijogct.2019.102783
Wu, G., Jia, S., Wu, B., & Yang, D. (2018). A discussion on analytical and numerical modelling of the land subsidence induced by coal seam gas extraction. *Environmental Earth Sciences*, *77*(9), 353. https://doi.org/10.1007/s12665-018-7526-z
Xue, F., Lv, X., Dou, F., & Yun, Y. (2020). A Review of Time-Series Interferometric SAR Techniques: A Tutorial for Surface Deformation Analysis. *IEEE Geoscience and Remote Sensing Magazine*, *8*(1), 22-42. https://doi.org/10.1109/MGRS.2019.2956165
Yao, Y., Liu, D., Tang, D., Tang, S., & Huang, W. (2008). Fractal characterization of adsorption-pores of coals from North China: An investigation on CH4 adsorption capacity of coals. *International Journal of Coal Geology*, *73*(1), 27-42. https://doi.org/https://doi.org/10.1016/j.coal.2007.07.003
Yeh, A., & O'Sullivan, M. (2007). Modelling Subsidence in Geothermal Fields. Proceedings New Zealand Geothermal Workshop,
Yesiller, N., Miller, C. J., Inci, G., & Yaldo, K. (2000). Desiccation and cracking behavior of three compacted landfill liner soils. *Engineering Geology*, *57*(1), 105-121. https://doi.org/https://doi.org/10.1016/S0013-7952(00)00022-3
Zang, A., Oye, V., Jousset, P., Deichmann, N., Gritto, R., McGarr, A., Majer, E., & Bruhn, D. (2014). Analysis of induced seismicity in geothermal reservoirs – An overview. *Geothermics*, *52*, 6-21. https://doi.org/https://doi.org/10.1016/j.geothermics.2014.06.005
Zang, J., Wang, K., & Zhao, Y. (2015). Evaluation of gas sorption-induced internal swelling in coal. *Fuel*, *143*, 165-172. https://doi.org/https://doi.org/10.1016/j.fuel.2014.11.007
Zare Reisabadi, M., Haghighi, M., Salmachi, A., Sayyafzadeh, M., & Khaksar, A. (2020). Analytical modelling of coal failure in coal seam gas reservoirs in different stress regimes. *International Journal of Rock Mechanics and Mining Sciences*, *128*, 104259. https://doi.org/https://doi.org/10.1016/j.ijrmms.2020.104259
Zeng, Q., & Wang, Z. (2017). A New Cleat Volume Compressibility Determination Method and Corresponding Modification to Coal Permeability Model. *Transport in Porous Media*, *119*(3), 689-706. https://doi.org/10.1007/s11242-017-0906-0
Zhang, J., Feng, Q., Zhang, X., Wen, S., & Zhai, Y. (2015). Relative Permeability of Coal: A Review. *Transport in Porous Media*, *106*(3), 563-594. https://doi.org/10.1007/s11242-014-0414-4
Zhang, J., Zhang, B., Xu, S., Feng, Q., Zhang, X., & Elsworth, D. (2021). Interpretation of Gas/Water Relative Permeability of Coal Using the Hybrid Bayesian-Assisted History Matching: New Insights. *Energies*, *14*(3), 626. https://www.mdpi.com/1996-1073/14/3/626
Zhong, R., Mitchell, T., Johnson, R., & Leonardi, C. (2022). Efficient implicit methods for wellbore shear failure analysis during drilling and production in coalbeds. *International Journal of Rock Mechanics and Mining Sciences*, *155*, 105129. https://doi.org/https://doi.org/10.1016/j.ijrmms.2022.105129
Zhou, X., Chang, N.-B., & Li, S. (2009). Applications of SAR Interferometry in Earth and Environmental Science Research. *Sensors*, *9*(3), 1876-1912. https://www.mdpi.com/1424-8220/9/3/1876

Zimmerman, R. W. (2017). Pore Volume and Porosity Changes under Uniaxial Strain Conditions. *Transport in Porous Media*, *119*(2), 481-498. https://doi.org/10.1007/s11242-017-0894-0
Zoback, M. D. (2007). *Reservoir Geomechanics*. Cambridge University Press. https://doi.org/DOI: 10.1017/CBO9780511586477

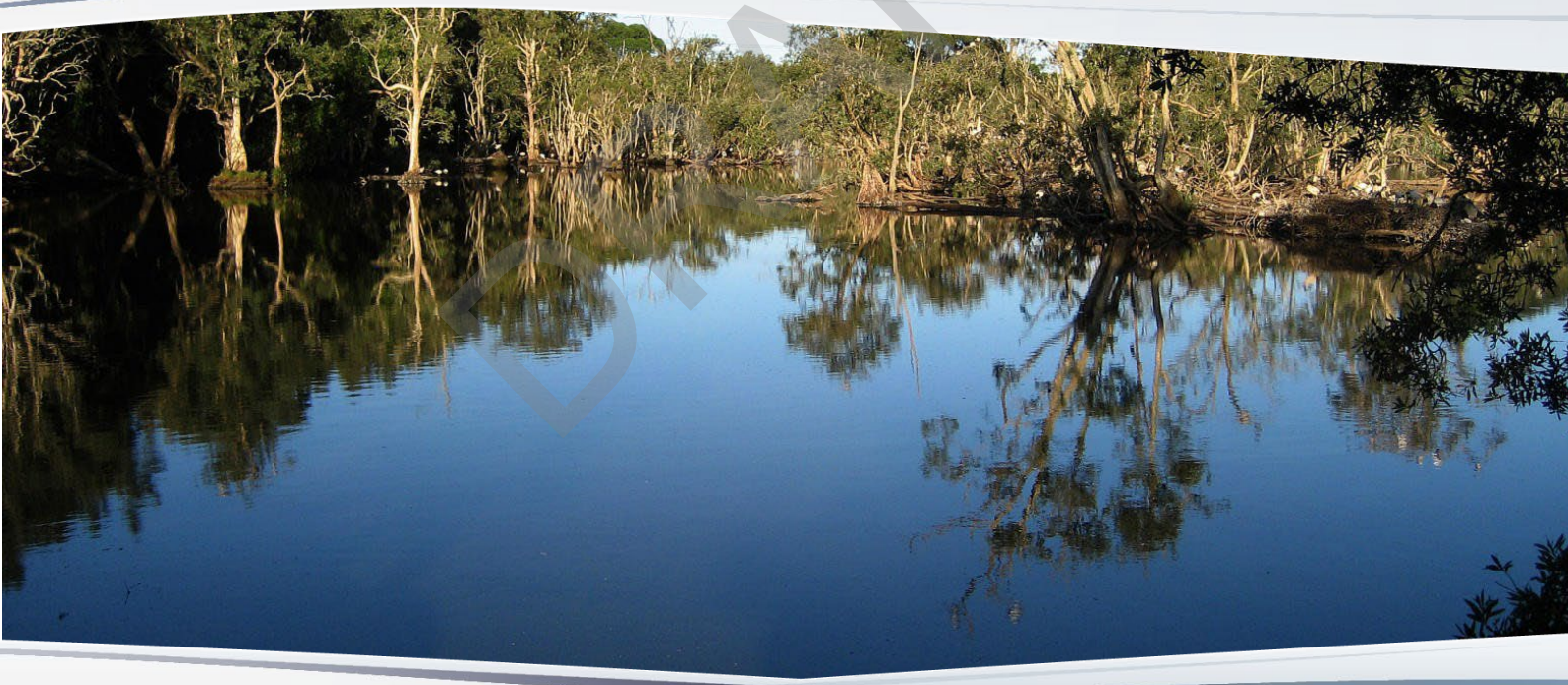

Australian Government | This initiative is funded by the Australian Government